

1. LEG 206 SUMMARY¹

Shipboard Scientific Party²

ABSTRACT

Drilling a complete section of oceanic crust has been an unfulfilled ambition since the inception of scientific ocean drilling. Recovery of in situ oceanic crust is imperative to understand igneous accretion and the complex interplay between magmatic, hydrothermal, and tectonic processes, as well as a means for calibrating remote geophysical observations, particularly seismic and magnetic data. Only by drilling a complete section of upper crust formed away from fracture zones can the processes operating at normal mid-ocean ridges be understood.

There is an observed relationship between the depth to axial low-velocity zones imaged at active mid-ocean ridges and spreading rate. Recent recognition of an episode of superfast spreading (200–220 mm/yr) on the East Pacific Rise ~11–20 m.y. ago presents an opportunity to drill through the upper oceanic crust into the gabbroic rocks in minimal time. Even allowing for significant burial by lavas that have flowed off axis (~300 m), the upper gabbros, thought to be the frozen axial melt lens, are predicted at ~1100–1300 meters below seafloor (mbsf).

During Leg 206, we completed the initial phase of a planned two-leg project to drill a complete in situ section of the upper oceanic crust that will eventually extend through the extrusive lavas and sheeted dikes and into gabbros. Drilling was conducted at Ocean Drilling Program (ODP) Site 1256 (6.736°N, 91.934°W) on ~15-Ma oceanic lithosphere of the Cocos plate, which was formed by superfast spreading (>200 mm/yr) at the East Pacific Rise. To fully characterize the sedimentary overburden and establish depths for the casing strings, three pilot holes were cored, recovering a nearly complete section of the 250.7 m of sediment overlying basement and penetrating 88.5 m into basement with very good recovery (61.3%). The sediments can be subdivided into two main lithologies. Unit I (0–40.6 mbsf) is clay rich with a few carbonate-

¹Examples of how to reference the whole or part of this volume.

²Shipboard Scientific Party addresses.

rich intervals, whereas Unit II (40.6–250.7 mbsf) is predominantly biogenic carbonate.

More than 500 m of young Pacific extrusive lavas were cored with moderate to high rates of recovery following the installation of a reentry cone with a 16-in-diameter casing string that extended 20 m into basement in Hole 1256D. Axial sheet flows with subordinate pillow lavas, hyaloclastites, and rare dikes are capped by a more evolved massive flow >74 m thick and other sheet flows that probably ponded in small faulted depressions several kilometers off axis. The lavas have normal mid-ocean-ridge chemistries and display moderate fractionation upsection as well as heterogeneous incompatible element ratios. The lavas are slightly to moderately affected by low-temperature hydrothermal alteration, and very little interaction with oxidizing seawater is apparent. The rocks are much less oxidized than those from Holes 504B and 896A in 6.9-Ma crust formed at an intermediate spreading rate and are more akin to the background alteration in Hole 801C (180 Ma), albeit with very little carbonate at Site 1256.

The complete lava sequence formed over a sufficient time period to record the transition from a stable shallowly dipping magnetic field in the axial lavas to a more steeply dipping field (inclination > 70°) in the overlying ponded flow. If our interpretation is correct, ~20% of the extrusive sequence cored so far formed from lavas that flowed significant distances from the axis.

A complete suite of geophysical wireline logs, including the first deployment in a basement hole of the Ultrasonic Borehole Imager (UBI), confirmed that Hole 1256D is in excellent condition, with robust margins and within gauge for its complete depth. Formation MicroScanner and UBI imaging will be integrated with other geophysical logs and the recovered core to refine the igneous stratigraphy and structure.

Hole 1256D was exited cleanly, leaving the hole clear of debris, open to its full depth, and primed for future deepening into the sheeted dikes and gabbros early in the next phase of ocean drilling.

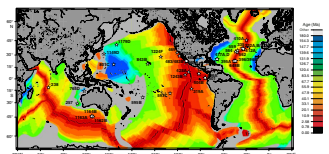
INTRODUCTION

The accretion of the oceanic crust is one of the major means of heat loss from the Earth's interior and is a fundamental component of the plate tectonic processes responsible for the formation and evolution of our planet's surface. Hydrothermal interactions at mid-ocean spreading centers and on the ridge flanks influence the chemistry of the oceans and, through subduction, the composition of the upper mantle. Despite the role that the ocean crust has played in the evolution of our planet, our sampling of in situ oceanic basement remains rudimentary. Samples of basalts, dikes, gabbros, and peridotites have been retrieved by dredging and from shallow drill holes from most of the ocean basins, but the geological context of these samples is rarely established. As such, the nature and variability of the composition and structure of the ocean crust away from transform faults and other tectonic windows remains poorly known.

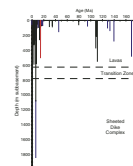
Drilling a complete crustal section has always been a major goal of deep ocean drilling (Shor, 1985), but this has been impeded by technical difficulties and the time investments required (Table T1; Figs. F1, F2). The distribution of drill holes into in situ basement formed at mid-ocean ridges is described in detail in the next section, but the present sparse sampling is instantly striking. Hole 504B, on the southern flank

T1. Drill holes into basement, 1968–2003, p. 103.

F1. Oceanic lithosphere drilling, 1968–2003, p. 40.



F2. Basement age vs. depth of basement penetration, p. 41.



of the Costa Rica Rift, remains our only complete section of in situ upper crust and the only hole to penetrate the extrusive lavas and most of the way through the sheeted dike complex. The dike/gabbro boundary has never been drilled, and the nature of the plutonic rocks directly underlying the sheeted dike complex has never been established. There are few significant penetrations (>100 m) of crust generated at fast or superfast spreading ridges and, before Leg 206, only one of those (Hole 1224F) in relatively young ocean crust (<50 Ma) (Table T1). Our poor sampling of ocean crust at different spreading rates and crustal ages and the absence of information on crustal variability compromises our ability to extrapolate observations from specific sites to global descriptions of the magmatic accretion processes and hydrothermal exchange in the ocean crust.

Summary of In Situ Basement Drilling during DSDP and ODP: 1968–2003

Deep drilling is perhaps the only approach able to address many fundamental questions about the formation, composition, and evolution of the oceanic lithosphere. Unfortunately, deep drilling of in situ ocean basement or the sampling of deeper crustal rocks in tectonic windows (e.g., Hess Deep) remains poor. As such, many of the primary questions that first motivated the inception of scientific ocean drilling remain unanswered.

Table T1 is a compilation of Deep Sea Drilling Project (DSDP) and Ocean Drilling Program (ODP) drill holes that have penetrated more than 50 m of in situ ocean basement cored from the top of the lava sequences. We have not included drill holes into plutonic rocks, such as the highly successful drilling in Hole 735B on the Southwest Indian Ridge or shallow penetrations at Hess Deep or the Kane Fracture Zone. Holes selected in this compilation were formed at normal, un sedimented ocean spreading ridges away from the influence of hotspots and have approximately normal mid-ocean-ridge (N-MORB) chemistry. Holes into arc crust (e.g., Holes 786B and 834B) have not been included, although arcs are another poorly sampled crustal domain.

Figure F1 shows the global distribution of deep drill holes into ocean basement. With a few exceptions, most effort in basement drilling has been concentrated on the northern Mid-Atlantic Ridge (MAR) and in the eastern Pacific Basin. There are only three holes south of the equator in the Pacific Ocean (Holes 319A, 595B, and 597C) and only a handful of penetrations into Indian Ocean crust. There are no holes into abyssal basement in the South Atlantic. Even though the Pacific Ocean is the largest ocean basin with the longest record of ocean spreading (0–180 Ma), there are only eight holes deeper than 50 m in crust older than 15 Ma, with Hole 801C being the only one drilled deeper than 400 meters subbasement (msb).

The penetration and age distribution of drill holes at all spreading rates and from all oceans is shown in Figure F2. It is clear from this figure that there is only one truly deep hole (>600 msb) into in situ crust. Hole 504B on the south flank of the intermediate–spreading rate Costa Rica Rift is the only hole that samples a complete section of extrusive lavas and penetrates into the sheeted dikes. Samples of the sheeted dike complex or the boundary between lavas and dikes have not been recovered by drilling from either slow- or fast-spreading crust. Although Hole 504B is the only hole where this important transition has been recovered, it remains difficult to evaluate how representative the recovered

sequence is relative to ocean crust overall. Presently, there are no samples of the uppermost gabbros and the thermal and chemical nature of the boundary between dikes and gabbros remains poorly known.

Seawater interaction with basalt continues for many millions of years on the ridge flanks, and a departure from the theoretical heat flow is discernible on average out to ~65 Ma (Stein and Stein, 1994), indicating the hydrothermal advection of heat. In order to evaluate the role that seawater-basement interactions play in buffering the chemistry of the oceans as well as the upper mantle, it is important to quantify the processes and extent of chemical and isotopic exchange with crustal age (e.g., Alt and Teagle, 1999). As can be seen in Figure F2, in addition to Hole 504B, there are a number of moderate-depth holes (<600 msb) drilled into young crust (<20 Ma). There are also a number of moderately deep samples of relatively old ocean crust, in particular the sampling of Cretaceous crust in the western Atlantic at Sites 417/418 and the recently deepened Hole 801C in Jurassic crust (~170 Ma) in the far western Pacific. However, there are very few samples of even the uppermost ocean crust and no holes of moderate depth into 20- to 110-Ma ocean crust, despite this being the critical age range. The average age of the ocean crust is ~61 Ma (Pollack et al., 1993), and the average age of oceanic basement presently being subducted is ~77 Ma. Knowledge of the extent of chemical and isotopic exchange in the time interval between 40 and 90 Ma is essential to constrain global hydrothermal budgets and the geochemistry of the upper mantle, but our present sampling of the ocean crust is woefully inadequate to address these issues.

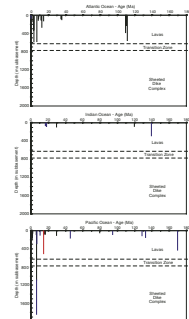
The crisis in our sampling of the oceanic lithosphere is even more acute when the current suite of drill cores is subdivided by spreading rates or ocean basin (Figs. F3, F4). Clearly, an extensive drilling program into in situ crust is required to thoroughly characterize the oceanic basement at a range of spreading rates and in all oceans. Such information is imperative to select a suitable site for the realization of the long-term goal of achieving a full penetration of ocean crust before the end of the first decade of the Integrated Ocean Drilling Program.

The Case for Deep Drilling of In Situ Ocean Crust

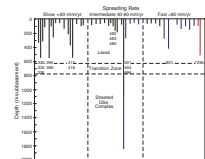
The transition from sheeted dikes to gabbros has never been drilled, and this remains an important objective in achieving a complete or even composite crustal section by either offset or deep drilling strategies. The dike-gabbro transition and the uppermost plutonic rocks are the frozen axial melt lens and the fossil thermal boundary layer between magma chambers and vigorous hydrothermal circulation (Fig. F5). Detailed knowledge of this transition zone is critical to our understanding of the mechanisms of crustal accretion and hydrothermal cooling of the ocean crust. The uppermost gabbros and the overlying sheeted dikes and extrusive lavas provide a time-integrated record of the processes of hydrothermal exchange and the associated fluid and chemical fluxes. The geochemistry of the frozen melt lens, when compared with the overlying dikes, lavas, and, if possible, lower crustal cumulate rocks, will place important controls on plutonic accretion processes. Drilling this interval will constrain magma chamber geometry and provide a geological context to geophysical observations of low-velocity zones.

Offset drilling strategies, where deeper portions of the ocean crust are sampled by drilling in tectonic windows, have recently been high priorities for ocean drilling (COSOD II, 1987; Ocean Drilling Program, 1996).

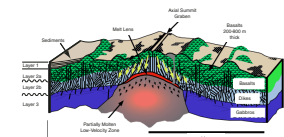
F3. Depth of penetration subdivided by ocean basin, p. 42.



F4. Depth of penetration clustered by spreading rate, p. 43.



F5. Cross section of crust created by superfast seafloor spreading, p. 44.



Drilling at several sites has provided a wealth of new data and understanding of gabbros and peridotites from the lower crust and upper mantle (e.g., Hess Deep, Kane Fracture Zone, and Southwest Indian Ridge). However, serious technical problems still exist with drilling tectonized rocks with little sediment blanket or without erosional removal of fractured material. It is also often difficult to relate drilled sections to the regional geology. Furthermore, at sites that are tectonized at very young ages, doubts will remain as to whether the same factors that cause tectonic exposures also perturb the ridge axis from the normal state. Composite sections are not substitutes for deep in situ penetrations, and the drilling of deep holes to obtain complete upper crustal sections continues to be a primary challenge for scientific ocean drilling (Dick and Mével, 1996; Ocean Drilling Program, 1996; Murray et al., 2002).

Even some basic observations regarding the architecture of ocean crust, including the lithology, geochemistry, and thicknesses of the volcanic and sheeted dike sections and the nature of the transition from dikes to gabbros, have yet to be made. Further progress is still required in order to correlate and calibrate geochemical, seismic, and magnetic imaging of the structure of the crust with basic geological observations. For example, how do velocity changes within seismic Layer 2 and the Layer 2–Layer 3 transition relate to the physical, structural, or alteration variations in the volcanics and dikes and to the dike–gabbro transition? At Site 504 in crust generated at an intermediate-rate spreading ridge, the Layer 2–Layer 3 transition lies within the 1-km-thick sheeted dike complex and coincides with a metamorphic change (Detrick et al., 1994; Alt et al., 1996), but is this representative of ocean crust and of crust generated at different spreading rates? Is the depth to gabbros shallower in crust generated at a superfast spreading rate, as predicted, and which of the volcanic or dike sections is thinner compared with crust constructed at slow or intermediate spreading rates? Francheteau et al. (1992) estimated a lava thickness of ~200 m at Hess Deep vs. >500 m at Site 504 and in the Atlantic; measurements of the thickness of seismic Layer 2A suggest 500–600 m for the East Pacific Rise (EPR) (e.g., Kent et al., 1994).

A second objective is to understand the interactions between magmatic and alteration processes, including the relationships between extrusive volcanics, the feeder sheeted dikes, and the underlying gabbroic rocks from the melt lens and subjacent sills/intrusions. Little information presently exists on the heterogeneity of hydrothermal alteration in the upper crust or the variability of the associated thermal, fluid, and chemical fluxes. How these phenomena vary at similar and different spreading rates is poorly known. Metamorphic assemblages and analyses of secondary minerals in material recovered by deep drilling can provide limits on the amount of heat removed by hydrothermal systems and place important constraints on the geometry of magmatic accretion and the thermal history of both the upper and lower crust. Fluid flow paths, the extent of alteration, and the nature of the subsurface reaction and mixing zones are all critical components of our understanding of hydrothermal processes that can only be addressed through drilling. These questions can be answered by examining the “stratigraphy” and relative chronology of alteration within the extrusive lavas and dikes; by determining whether disseminated sulfide mineralization, fluid mixing, and a large step in thermal conditions is present at the volcanic–dike transition (as in Hole 504B and many ophiolites); and from the grade and intensity of alteration in the lower dikes and upper

gabbros. The lowermost dikes and upper gabbros have been identified as both the conductive boundary layer between the magma chambers and the axial high-temperature hydrothermal systems and the subsurface reaction zone, where downwelling fluids acquire black-smoker chemistries (Alt et al., 1996; Vanko and Laverne, 1998). However, extensive regions of this style of alteration or zones of focused discharge have yet to be recognized and information from ophiolites may not be appropriate to in situ ocean crust (Richardson et al., 1987; Schiffman and Smith, 1988; Bickle and Teagle, 1992; Gillis and Roberts, 1999). Drilling down to the boundary between the lower dikes and upper gabbros will allow tracing of fluid compositions (e.g., Teagle et al., 1998) and the integration of the thermal requirements of hydrothermal alteration in sheeted dikes and underlying gabbros with the magmatic processes in the melt lens.

Marine magnetic anomalies are one of the key observations that led to the development of plate tectonic theory, through the recognition that the ocean crust records the changing polarity of the Earth's magnetic field through time (Vine and Matthews, 1963). It is generally assumed that micrometer-sized grains of titanomagnetite within the erupted basalt are the principal recorders of the marine magnetic anomalies, but recent studies of tectonically exhumed lower crustal rocks and serpentinized upper mantle indicate that these deeper rocks may also be a significant source of the magnetic stripes. Whether these deeper rocks have a significant influence on the magnetic field in undisrupted crust is unknown, as is the extent of secondary magnetite growth in gabbros and mantle assemblages away from transform faults. Sampling the plutonic layers of the crust could refine the Vine-Matthews hypothesis by characterizing the magnetic properties of gabbros and peridotites through drilling normal ocean crust, on a well-defined magnetic stripe, away from transform faults.

Although there are several questions that can be answered with shallow holes in tectonic windows such as Hess Deep, where deep and mid-crustal rocks crop out, other questions on topics from in situ permeability to alteration history require sampling of intact normal oceanic crust. A suite of drill holes into in situ basement from a range of spreading rates and ages is required to thoroughly understand and characterize the variability of the processes occurring during the accretion and evolution of the ocean crust.

SCIENTIFIC OBJECTIVES

Leg 206 is the first part of a two-leg strategy to sample a complete crustal section from extrusive lavas, through the sheeted dikes, and into the uppermost gabbros from in situ ocean crust, by drilling a deep hole into basement formed at a superfast spreading rate. Drilling crust generated at a superfast spreading rate will provide comprehensive documentation of one end-member style of mid-ocean-ridge accretion (COSOD II, 1987; Ocean Drilling Program, 1996).

Although perhaps only 20% of the global ridge axis is separating at fast spreading rates (>80 mm/yr full rate), ~50% of the present-day ocean crust and ~30% of the total Earth's surface was produced at this pace of ocean spreading. At least in terms of seismic structure (Raitt, 1963; Menard, 1964), crust formed at fast spreading rates is relatively simple and uniform. Hence, the successful deep sampling of such crust

in a single location can reasonably be extrapolated to describe a significant portion of the Earth's surface.

To date, legs with drilling fast spreading crust as their primary objective (DSDP Leg 54 and ODP Leg 142) have been mostly unsuccessful, and apart from sampling of surficial recent basalt at ridge axes, little is known of the shallow- and intermediate-depth structure of fast-spreading crust (Table T1). Penetration of ~100 m of fast-spreading basalt has been achieved during several legs with other objectives (Legs 92, 136, 200, and 203). One recent example is drilling at Site 1224 during Leg 200 in the eastern North Pacific, which sampled the upper 146.5 m of basaltic oceanic crust formed at a fast spreading rate (142 mm/yr full rate) (Stephen, Kasahara, Acton, et al., 2003). Studies of Site 1224 are ongoing but limited to the extrusive basalt flows recovered. ODP Hole 801C in fast-spreading crust was also recently deepened to >400 msb, but further penetration was not possible because of other drilling objectives (Plank, Ludden, Escutia, et al., 2000). A continuous section through the upper oceanic crust and ultimately into mid-crustal gabbros is imperative to calibrate geophysical observations and validate theoretical models of the ocean crustal processes.

Drilling of superfast-spreading rate ocean crust during Leg 206 was undertaken to characterize magmatic accretion processes and the primary and secondary chemical composition, as well as the tectonic, magnetic, and seismic structure of the uppermost oceanic crust. The target depth for Leg 206 was 500–800 m subbasement, which was achieved with 502 m of basement penetration in Hole 1256D. Cores from Leg 206 will provide an essential link to relate geology to remote geophysical observations (seismics and magnetics) and ground-truth the relationship between seismic stratigraphy and basement lithostratigraphy. Paleomagnetic studies will establish the relative contributions of the major rock types to marine magnetic anomalies, and the position of our site (~5 km) from the center of a magnetic reversal will provide information on crustal cooling rates and the contribution of deep plutonic rocks to surface magnetic anomalies. The reentry hole (Hole 1256D) drilled during Leg 206 provides the first test of the lateral variability of the ocean crust and provides an essential comparison for the models of crustal accretion, hydrothermal alteration, and the secondary mineral/metamorphic stratigraphy principally developed from ODP Hole 504B. This will refine models for the vertical and temporal evolution of ocean crust, including the recognition and description of zones of hydrothermal and magmatic chemical exchange. Physical property measurements of cores recovered from fast-spreading ocean crust will yield information on the porosity, permeability, and stress regime as well as the gradients of these properties with depth. A full suite of wireline logs will supplement geological, chemical, structural, magnetic, and physical property observations on the core. The careful integration of borehole observations with measurements of the recovered core is imperative for the quantitative estimation of chemical exchange fluxes between the ocean crust and oceans.

A major objective of Leg 206 was to establish a cased reentry hole that is open for future drilling to the total depth penetrated during the leg. Although it was never likely that one drilling leg would be enough to reach the dike-gabbro transition zone, our efforts have provided the groundwork for a second leg solely focused on deepening Hole 1256D. The return visit to this site, by the Integrated Ocean Drilling Program, should be able to penetrate deep enough to determine the geological nature of the geophysically imaged "axial melt lens" believed to be

present close to the gabbro–dike transition. Drilling of this boundary in situ will allow the relationships between vigorous hydrothermal circulation, mineralization, dike injection, and the accretion and freezing of the plutonic crust to be investigated.

Rationale for Site Selection

During Leg 206, we drilled ocean crust that formed at a superfast spreading rate in the equatorial Pacific ~15 m.y. ago. Our rationale for choosing this particular location and confidence that drilling crust formed at a superfast spreading rate provides the best chance of reaching gabbros in normal oceanic crust in a two-leg drilling strategy is

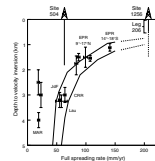
1. There is an inverse relationship between spreading rate and the depth to axial low-velocity zones imaged by multichannel seismic (MCS) reflection studies, making it more likely that a hole can be drilled into the gabbros.
2. A thick sediment blanket (~250 m) covering the chosen site should enhance core recovery through increased cementation of the upper crust and is sufficiently thick to allow installation of a reentry cone with 20-in casing.
3. The chosen site (~15 Ma) is significantly older than Hole 504B (~6.9 Ma) and lower temperatures are predicted at midlevels in the crust, so high borehole temperatures should not become an issue until the gabbros are penetrated.

Purdy et al. (1992) describe an inverse relation between spreading rate and depth to an axial low-velocity zone, interpreted as a melt lens (Fig. F6). Since the Purdy et al. compilation, careful velocity analysis, summarized by Hooft et al. (1996), has refined the conversion from traveltimes to depth, and data from additional sites have been collected (Carbotte et al., 1997). The fastest-rate spreading centers surveyed with modern MCS reflection, ~140 mm/yr full rate at 14°–18°S on the EPR, show reflectors, interpreted as the axial melt lens, at depths of 940–1260 mbsf (Detrick et al., 1993; Kent et al., 1994; Hooft et al., 1994, 1996). At 9°–16°N on the EPR, where spreading rates are 80–110 mm/yr, depths to the melt reflector are mostly 1350–1650 mbsf, where well determined (Kent et al., 1994; Hooft et al., 1996; Carbotte et al., 1997).

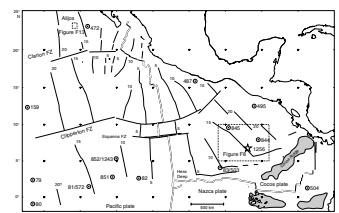
Recent interpretation of magnetic anomalies formed at the southern end of the Pacific/Cocos plate boundary identify crust that was formed at full spreading rates of ~200–220 mm/yr from ~20 to 11 Ma (Wilson, 1996) (Fig. F7). The implication from reflection seismic studies of axial low-velocity zones is that crust formed at such superfast spreading rates should have a relatively thin dike section and the top of the gabbros should occur at shallow depths.

The theoretical basis for expecting an inverse relation between spreading rate and melt lens depth is fairly straightforward. The latent heat released in crystallizing the gabbroic crust must be conducted through the lid of the melt lens to the base of the axial hydrothermal system, which then advects the heat to the ocean. The temperature contrast across the lid is governed by the properties of magma (1100°–1200°C) and thermodynamic properties of seawater (350°–450°C where circulating in large volumes) and will vary only slightly with spreading rate. The heat flux through the lid per unit ridge length will therefore be proportional to the width of the lens and inversely proportional to the lid thickness. For reasons that are not understood, seismic observa-

F6. Depth to axial low-velocity zone, p. 45.



F7. Age map of the Cocos and Pacific plates, p. 46.



tions show uniform width of the melt lens, independent of spreading rate. With width and temperature contrast not varying, the extra heat supplied by more magma at faster spreading rates must be conducted through a thinner lid (dike layer) to maintain steady state (see Phipps Morgan and Chen [1993] for a more complete discussion). To reach the dike–gabbro transition in normal oceanic crust with minimal drilling, it is therefore best to choose the fastest possible spreading rates. A setting similar to the modern well-surveyed area at 14°–18°S could be expected to reach gabbro at a depth of ~1400 m, based on 1100 m to the axial magma chamber reflector and subsequent burial by an additional 300 m of extrusives (Kent et al., 1994). At faster rates, depths could possibly be hundreds of meters shallower. In contrast, seismic velocity inversions at the axes of the Juan de Fuca Ridge and Valu Fa Ridge in Lau Basin occur at depths of ~3 km (Purdy et al., 1992) at an intermediate spreading rate comparable to that at Site 504.

A possible factor for the favorable drilling conditions in the 6.9-m.y.-old crust cored in Hole 504B compared with very young fast-spreading crust from Legs 54 and 142 is the equatorial latitude of formation. High equatorial productivity results in high sedimentation rates (>30 m/m.y.) and the rapid burial of the igneous crust when middle levels of the crust are still hot. Conductive reheating of the upper crust due to a thick sediment blanket and restricted seawater access facilitates drilling by accelerating the cementation in the upper basement and increasing the competency of healed fractures.

The fast spreading rates highlighted in Figure F7 occurred near the equator, and rapid initial sedimentation rates of at least 35 m/m.y. have been confirmed at ODP Sites 844 and 851 from Leg 138 and Site 572 from DSDP Leg 85. A sediment cover of ~240 m was estimated for the proposed drill site.

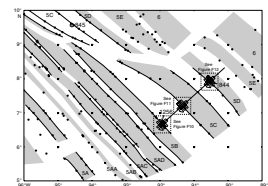
Thermal stresses that resulted in drilling-induced fracturing deep in Hole 504B should be diminished in this older crust (~15 Ma, compared with 6.9 Ma for Hole 504B). Although such fracturing did not prohibit deep penetration in Hole 504B, it did inhibit recovery rates. The predicted lower temperatures at Site 1256 provide some indication that better deep drilling conditions than those in Hole 504B can be expected.

Location Criteria for Deep Drilling of Upper Oceanic Crust Formed by Fast Seafloor Spreading

Full spreading rates for the southern Cocos/Pacific plate boundary (Figs. F7, F8) were ~200–220 mm/yr (Wilson, 1996), 30% to 40% faster than the fastest modern spreading rate. This episode of superfast spreading ended with a reorganization of plate motions at 10.5–11.0 Ma; subsequent plate vectors have been similar to present-day motions. The southern limit of crust formed at the superfast rates is the trace of the Cocos/Nazca/Pacific triple junction, as Nazca/Pacific and Cocos/Nazca spreading rates were not as fast. The older age limit of this spreading episode is hard to determine with the limited mapping and poor magnetic geometry of the Pacific plate. It is at least 18 Ma and could reasonably be 24–25 Ma. The northern limit of this province is entirely gradational, with rates dropping to ~150 mm/yr somewhat north of the Clipperton Fracture Zone. By apparent coincidence, the fastest spreading rates occurred within a few degrees of the equator.

Using the fastest possible spreading rate as a proxy for shallowest occurrence of gabbro still allows a range of possible drilling sites. There is

F8. Isochrons inferred from magnetic anomalies, p. 47.



no reason to expect a difference in crustal structure between the Cocos and Pacific plates, but logistics favor a site on the Cocos plate. Transits from a variety of Central American ports would be only 2–4 days, and sediments are ~200 m thinner than those on the Pacific plate. It seems prudent to choose an anomaly segment at least 100 km long and a site at least 50 km from the end of the segment. For ages 12–16 Ma (Anomalies 5AA–5B) these criteria are easy to satisfy because the southernmost segment of the Pacific-Cocos Ridge had a length of at least 400 km. For ages 17 Ma (Anomaly 5D) and older there is a fracture zone to avoid, but the length of anomaly segments is at least 150 km.

The only serious drawback to this area as a crustal reference section for fast spreading rates is the low original latitude, for which the determination of magnetic polarity from azimuthally unoriented core samples is nearly impossible. Also, the nearly north–south ridge orientation makes the magnetic inclination insensitive to structural tilting. The polarity problem could be solved with a reliable hard rock orienting device, but development efforts for such a tool have been abandoned. Magnetic logging with either the General Purpose Inclinerometry Tool (GPIT) fluxgates that are part of the Formation MicroScanner–Dipole Shear Sonic Imager (FMS-sonic) tool string or, preferably, a separate magnetic tool with functional gyroscopic orientation should also be adequate for polarity determination, as demonstrated in Holes 504B and 896A by wireline logs collected during Leg 148 (Worm et al., 1996).

Alternative sites have other, often more serious, drawbacks. Sites flanking the EPR south of the equator generally have poor accessibility and, for the age range 10–25 Ma, have a complicated tectonic setting and spreading rates are poorly known. North of the equator, sites are available in the same Cocos-Pacific system, which is better understood and more tectonically stable, but there is a severe trade-off between latitude and spreading rate. A magnetically desirable latitude of 20° would reduce the spreading rate to ~60% of the rate for the sites we propose, which may significantly increase the depth to gabbro. To detect structural rotations about a nearly north–south ridge axis, paleolatitude should probably exceed 25°, which means that no site satisfying this criterion will also offer fast spreading rate and short transit to common ports.

REGIONAL GEOLOGY AND TECTONIC SETTING

Geological Setting

Site 1256 (6°44.2'N, 91°56.1'W) lies in 3635 m of water in the Guatemala Basin on Cocos plate crust formed at ~15 Ma on the eastern flank of the EPR (Fig. F7). The site sits astride the magnetic Anomaly 5Bn–5Br magnetic polarity transition (Fig. F8). This crust accreted at a superfast spreading rate (~200–220 mm/yr full rate) (Wilson, 1996) and lies ~1150 km east of the present crest of the EPR and ~530 km north of the Cocos-Nazca spreading center. Cocos plate crust of 23- to 25-Ma age is being subducted along the Central American Trench ~830 km to the northeast. The trace of the Cocos/Pacific/Nazca triple junction passes ~100 km to the southeast, with the elevated bathymetry of the Cocos Ridge recording the trail of the Galapagos plume farther to the southeast (~500 km) (Fig. F7). The Guatemala Basin has relatively subdued bathymetry, and the immediate surroundings of Site 1256 (~300 km)

are relatively unblemished by major seamount chains or large tectonic features high enough to penetrate the sediment cover (~200–300 m).

Site 1256 formed at an equatorial latitude (Fig. F9) within the equatorial high-productivity zone and initially endured very high sedimentation rates (>30 m/m.y.) (e.g., Farrell et al., 1995). Reconstruction Figure F9 is in the reference frame fixed to the Antarctic plate, which is nearly fixed relative to the spin axis and to hotspots. Motion of the Pacific plate relative to Antarctica is from Cande et al. (1995), and motion of the Cocos plate relative to the Pacific plate is from Wilson (1996). Velocities relative to Antarctica are similar to those at present for the Pacific plate but are much faster than those at present for the Cocos plate.

As is described in greater detail below in “Site Survey Results,” Site 1256 sits atop a region of smooth basement topography (<10 m relief) and has a seismic structure reminiscent of typical Pacific off-axis seafloor. Upper Layer 2 velocities are 4.5–5 km/s, and the Layer 2–3 transition is at ~1200–1500 m subbasement. The total crustal thickness at Site 1256 is estimated at ~5–5.5 km. Farther to the northeast of Site 1256 (15–20 km) a trail of ~500-m-high circular seamounts rise a few hundred meters above the sediment blanket (Fig. F10). Basement topography is more pronounced southwest of Site 1256 and in the grid 2 area (Fig. F11), where subparallel narrow ridges (1–2 km) and wider troughs (4–5 km) display ~100–150 m of basement relief.

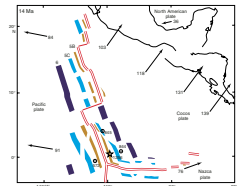
Site Survey Results

The site survey cruise for this leg took place in March and April 1999 aboard the *Maurice Ewing*, led by D. Wilson, A. Harding, and G. Kent. At the urging of the Architecture of Oceanic Lithosphere Program Planning Group, the original plan for four sites in the Guatemala Basin was modified to instead cover three sites there and a separate site near Alijos Rocks west of Southern Baja California (Fig. F7). The suggested advantage of the Alijos site is higher paleolatitude, allowing determination of magnetic polarity with azimuthally unoriented cores. The other significant difference recognized before survey work was lower spreading rate, ~120–130 mm/yr instead of 200–220 mm/yr, with a presumably greater depth to the uppermost gabbros.

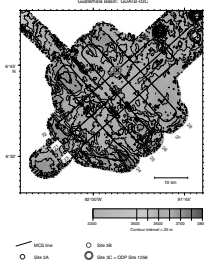
The site survey work focused on seismic reflection and refraction. MCS reflection and refraction experiments to ocean-bottom hydrophones (OBHs) were conducted separately because of differences in desired shot intervals. MCS work used a tuned array of 10 air guns shooting to a new 480-channel, 6-km streamer, with a nominal shot interval of 37.5 m (15–18 s). With a hydrophone spacing of 12.5 m, this geometry gives 80-fold coverage with 6.25-m midpoint spacing. Refraction shooting to grids of 10–11 OBHs using 20 air guns was at a shot interval of 90 s (130–180 m) for most of the grid and 150 s (300 m) for the outermost shots. The grid geometry was designed for well-constrained measurements of velocities in both across-strike and along-strike directions to depths of 1.5–2.0 km and to cover to Mohorovicic Discontinuity (Moho) depths in the across-strike direction only (Figs. F10, F12, F13). Because of time constraints and delays from several causes, refraction surveying was only conducted at two of the three Guatemala Basin sites.

The Guatemala Basin sites have 200–300 m of sediment cover resulting from their formation near the paleoequator. Referring to the sites in the order MCS data were collected, grid 1 was chosen to include ODP Site 844 at a line crossing and to be centered near the magnetic Anom-

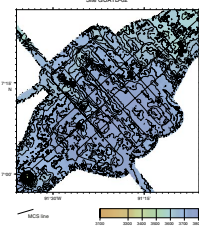
F9. Reconstruction of Site 1256 at 14 Ma, p. 48.



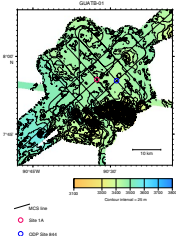
F10. Site survey track map, Site 1256, p. 49.



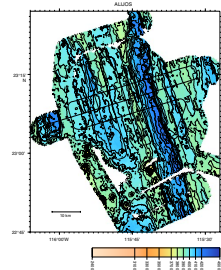
F11. Site survey track map, Site GUATB-02, p. 50.



F12. Site survey track map, Site GUATB-01, p. 51.



F13. Site survey track map, Site ALIJOS, p. 52.



aly 5D(y) boundary, and grids 2 and 3 were centered on Anomalies 5C(y) and 5B(o) along a flow line perpendicular to anomaly strike (Fig. F8). Grids 1 and 3 have refraction data. Grid 1 is quite shallow for its ~17-Ma age at 3400–3500 m, and basement at Site 844 is at 3705 m (Fig. F12). Relief on basement as seen in MCS data is extremely low, with the largest scarps having ~30-m amplitude. Subtle horizontal reflections ~1.6–1.7 s below basement are interpreted to correspond to the Moho. A cluster of seamounts with minimum depth of 2790 m is present near the southern tip of the grid.

Grid 3 is deeper than grid 1 at 3600–3700 m, and basement, at ~3900 m, is near normal depth for the ~15-Ma age (Fig. F10). In the southwest half of the grid, abyssal hill fabric is visible through the sediment cover and larger scarps approach 100-m amplitude. The northeast half of the grid has low relief, comparable to grid 1. Reflection data here commonly show complex reflectors at 1.3–1.8 s below basement, indicating dipping interfaces in the lower crust or upper mantle, probably including some Moho reflections. Upper crustal reflectors at ~0.4–0.8 s into basement are often bright and tend to have gentle (~20°) apparent dips in the isochron direction, with more horizontal apparent dips in the spreading direction (Figs. F14, F15). Analysis of refraction data in this grid shows crustal structure that is fairly typical for off-axis Pacific sea-floor. Upper Layer 2 velocities are 4.5–5 km/s, a gradual transition between Layers 2 and 3 is at ~1.5 km below basement, and total crustal thickness is ~5–5.5 km (Fig. F16). Velocities of the uppermost crust are slowest in the southwestern part of the grid where the abyssal hill relief is greatest.

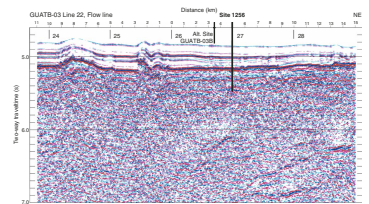
In contrast to the Cocos plate sites, grid 4 near Alijos Rocks has thin (50–100 m) sediment, slightly deep water (3800–4300 m) for the ~16.5-Ma age, and extremely high relief for the fast spreading rate (Fig. F13). Individual scarps are commonly 150 m and up to 400 m. MCS data show few coherent reflections below Layer 2 in preliminary stacks. Receiver gathers for refraction data are broadly similar to the Cocos plate sites, perhaps suggestive of slightly slower velocities at ~1 km below basement.

Magnetic data at the Cocos plate sites show trends parallel to the previously mapped regional trend, with no evidence for isochron offsets at ~1-km detection limit within the grids (Fig. F11) and perhaps 3- to 5-km detection limit outside the grids. The Alijos grid is located within an area where magnetic and topographic features are linear for 30–40 km, but right-stepping offsets of a few kilometers leave the local trend a few degrees counterclockwise of the regional trend.

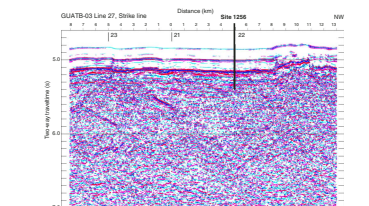
Of the three survey grids with refraction data, grid 3 (the southwesternmost and youngest of the Cocos plate grids) was chosen as the primary target for Leg 206 because its depth and basement relief are closest to normal. Within this grid, several factors affected the final site selection. The slower seismic velocities in southwestern part of the grid indicate more porous and possibly more rubbly material that may lead to poorer drilling conditions. OBH failure on line 23 along the southeastern part of the grid led to limited constraints on velocity determinations there.

A very bright upper crustal reflector is observed on much of line 21 in the northeastern part of the grid and for short distances on lines 27 and 28 where they cross line 21 (see Fig. F15). The reflector dips northwest and projects updip to a ~50-m-high hill that strikes northeast, perpendicular to the normal abyssal hill trend. The character of the reflection and its relation to the nearly vertical velocity gradient determined

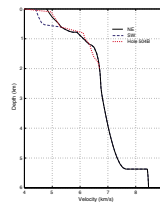
F14. MCS data from line 22, p. 53.



F15. MCS data from line 27, p. 54.



F16. Velocity model based on inversion of refraction data, p. 55.



by refraction analysis are both more consistent with a narrow low-velocity zone rather than a simple interface between materials of different velocity. All of these relations suggest that the reflector might be a thrust fault, possibly driven by thermal contraction of the lower lithosphere. Because such a fault might lead to very poor drilling conditions at about the depths gabbro might be encountered on a return leg, this area was dismissed as a potential site for deep drilling. The remaining area near the northern corner of the grid appears very suitable for deep drilling, and the intersection of lines 22 and 27 (proposed Site GUATB-03C), where the velocity control is best, was the primary drilling location for Leg 206, Site 1256 (Figs. F10, F14, F15).

OPERATIONS

The *JOIDES Resolution* arrived at Pier 6 in Balboa, Republic of Panama, with the first line ashore at 1030 hr on 6 November 2002, marking the end of Leg 205 and the start of Leg 206. All times are reported in local ship time, which is Universal Time Coordinated (UTC) (a list of operation acronyms is given in Table T2) minus 5 hr in Panama and UTC minus 6 hr at Site 1256. A summary of operations completed during Leg 206 is given in Table T3.

Transit to Site 1256

The pilot boarded the vessel at 1404 hr on 11 November, which corresponded to low tide. This time was selected to ensure safe clearance of the derrick under the Bridge of Americas. At 1534 hr, the pilot disembarked and the vessel headed to Site 1256 (proposed Site GUATB-03C in the Leg 206 Scientific Prospectus) in the Guatemala Basin. The 821-nmi transit to Site 1256 was accomplished at an average speed of 11.0 kt and was without incident. The vessel was on station using the Global Positioning System data by 1630 hr on 14 November.

Hole 1256A

Hole 1256A was spudded with the advanced piston corer (APC) at 0640 hr on 15 November. The seafloor depth was estimated at 3634.5 m (3645.2 meters below rig floor [mbrf]) based on core recovery. The single mudline core from this hole was obtained to ensure that a good mudline was recovered and to provide additional material for microbiological and geochemical sampling.

Hole 1256B

Before starting Hole 1256B, the advanced piston corer temperature (APCT; formerly known as the Adara) shoe was held just above seafloor from 0753 to 0813 hr to obtain a temperature measurement of the bottom water. Hole 1256B was then spudded with the APC at 0815 hr on 15 November. The seafloor depth inferred from the recovery was 3634.7 m (3645.4 mbrf).

Piston coring deepened the hole until Core 206-1256B-18H failed to achieve a full stroke of the corer at a depth of 160.1 mbsf. The recovery for the piston-cored interval was 163.91 m (average recovery = 102.4%). Cores were oriented using the Tensor tool starting with Core 206-1256B-3H. In addition to the bottom-water temperature measurement,

T2. Operation acronyms, p. 105.

T3. Operations summary, Leg 206, p. 106.

downhole temperature measurements were attempted with the APCT at 34.6 mbsf (Core 206-1256B-4H), 53.6 mbsf (Core 6H), 82.1 mbsf (Core 9H), 120.1 mbsf (Core 13H), and 158.1 mbsf (Core 17H). The first attempt (Core 206-1256B-4H) did not record a valid temperature because of battery failure in the instrument, but other measurements were successful.

Coring in Hole 1256B continued with the extended core barrel (XCB) system to 251.7 mbsf, where the last core penetrated basaltic basement and recovered 6 cm of basalt. The XCB cored 91.6 m and recovered 60.23 m (average recovery = 65.8%). Recovery below 210 mbsf dropped considerably because chert nodules were getting jammed in the throat of the cutting shoe.

The drill string was pulled free of the seafloor at 1635 hr on 16 November, ending Hole 1256B. The total results for the hole were 251.7 m cored and 224.14 recovered, giving an average recovery of 89.1% (Tables T4, T5).

Jet-In Test

The vessel offset 10 m south of Hole 1256B to conduct a jet-in test. This test was performed in order to establish the length of 20-in surface casing to deploy with the reentry cone in Hole 1256D. The test penetrated 100 m with a maximum pump of 34 strokes/min (spm) and pump pressure of 200 psi. The drill string was then recovered to change the bottom-hole assembly (BHA) for rotary core barrel (RCB) coring in Hole 1256C. The APC/XCB bit was at the rotary table at 0630 hr on 17 November.

Hole 1256C

After assembling the RCB BHA, the pipe was tripped to the seafloor and Hole 1256C was spudded at 1515 on 17 November. The hole was drilled down to 220.1 mbsf before coring began. The first core (206-1256C-1R) contained only a few small pieces of chert in the core catcher. The presence of chert plagued recovery on the next two sedimentary cores, although 4.67 m of nannofossil ooze was recovered in Core 206-1256C-3R. Basement was tagged in Core 206-1256C-4R at a depth of 251.8 mbsf.

Subsequent coring into basement resulted in some spectacular recovery percentages for RCB coring in hard rock, with 10.07 m recovered (recovery = 109.5%) in Core 206-1256C-9R and 10.24 m recovered (recovery = 107.6%) in Core 11R. Recovery from Cores 206-1256C-5R through 11R (252.4–312.8 mbsf) averaged 81.8%. The last two cores (206-1256C-13R and 14R) penetrated 18.3 m and recovered 0.16 m, or 0.9% of the cored interval. This reduced the average recovery in basement to 61.3%. The average rate of penetration (ROP) for RCB coring in basement was 1.4 m/hr. Recovery for the hole, including sediment and basement, averaged 50.8% (Tables T4, T5). The total depth of Hole 1256C is 340.3 mbsf, with the lower 88.5 m in basement.

Logging

At the conclusion of coring, Hole 1256C was prepared for logging with a wiper trip to 83 mbsf. After the bit was released, the hole was displaced with 92 bbl of sepiolite mud and the end of the pipe (EOP) was set at the logging depth of 125.8 mbsf.

T4. Coring summary, Site 1256, p. 108.

T5. Operations summary, Site 1256, p. 109.

The triple combination (triple combo) tool string was deployed first but was unable to pass a bridge at ~203 mbsf (only 77 m below the EOP). Following recovery of the logging tool and de-rigging the Schlumberger equipment, the drill string was lowered to within 20 m of the bottom of the hole to clear obstructions. A second attempt to deploy the triple combo tool string was made with the EOP placed at 231 mbsf. This time the tool string successfully logged across the sediment/basement interface. The FMS/sonic tool string was then deployed but was unable to advance deeper than ~257 mbsf (~5 m into basement). Given the time it would have taken to clear the obstruction and the relatively short interval of basement that could have been logged, we terminated the logging program. The drill string was recovered with the EOP clearing the rotary table at 0345 hr on 23 November.

Hole 1256D

Reentry Cone and 20-in Casing

To prepare for the deployment of the reentry cone and 20-in casing, the assembled reentry cone was positioned over the moonpool doors. The jet-in BHA was lowered and landed into the hanger of the reentry cone. The entire cone, casing, and BHA was then lowered through the moonpool doors at 1606 hr on 23 November. Hole 1256D was spudded at 0025 hr on 24 November when the tip of the 20-in casing shoe contacted the seafloor. Hole 1256D is located ~30 m south of Hole 1256C and ~50 m south of Holes 1256A and 1256D (Fig. F17). It required 10.2 hr to jet the 95 m of casing into the sediment. The mudskirt contacted the seafloor at 1035 hr on 24 November.

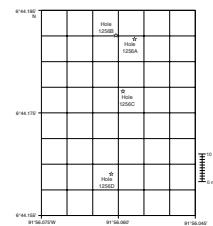
Opening the Hole for 16-in Casing

The next phase of operations required the drilling out of a 21½-in hole below the 20-in casing into basement in order to accept the 16-in casing. Based upon the experience acquired drilling the pilot hole (Hole 1256C), it was planned to set the 16-in casing 20 m into basement with an additional 10 m of 21½-in hole (rathole). In order to drill this large hole, the ODP Drilling Services Department acquired two Downhole Design, Inc. (DDI) B182×215 bi-centered reamers (BCRs). This hardware is designed to be operated with a 97/8-in-diameter pilot rock bit. This combination may be used to drill and ream simultaneously or to open a previously drilled hole. The B182×215 BCR has an 18¼-in pass-through diameter that allows this hardware to fit through the 20-in casing. When drilling, the actual diameter of the cut hole is 21½-in. This was the first time such a device was used in scientific ocean drilling.

The BCR, affixed to a 97/8-in hard-formation tricone drilling bit, reentered the cone at 0620 hr on 25 November and was then lowered to the bottom of the 20-in casing (95 mbsf) to begin drilling a 21½-in hole through the sediment. Because the upper 190 m of the formation was very soft, the bit was advanced at a controlled rate of 35 m/hr.

Basement was entered and reaming progressed to ~17 m into basement when, starting in the late evening of 26 November and continuing into the early morning of the following day, the torque steadily increased. Because of crew unfamiliarity with the operating characteristics of the BCR, it was considered prudent to pull this hardware a little over the halfway point with only 38 rotating hours and inspect the condition of the pilot bit and BCR.

F17. Location map of four holes drilled, Site 1256, p. 56.



When the BCR was on the surface, the reason for the high torque was apparent. One of the three cones on the pilot bit was almost completely destroyed and missing all of the ~30 ball bearings. The tungsten carbide inserts were also severely ground down. Interestingly enough, the other two cones were relatively undamaged and the bi-centered reamer was in excellent shape and gauge with only two teeth missing. There was some junk damage to the sides of the bit and reamer.

Because of the potential that metal fragments remained in the hole, a special hole cleaning assembly was put together. A double junk basket was made up with a slightly used hard-formation tricone bit. The clean-out assembly reentered the cone at 2140 hr on 27 November and by midnight was on the bottom of the hole. The junk baskets were "worked" by running the mud pumps at a combined rate of 100 spm (500 gpm) at 800 psi for very short durations to stir up the loose material at the bottom of the hole. When the pumps were shut off, the cloud of debris would settle back to the bottom and into the open tops of the junk baskets. The junk baskets were worked for 1.5 hr, after which 1 m was drilled (267.1–268.1 mbsf) with the 9⁷/₈-in bit. The bit penetrated 1 m in 2 hr (ROP = 0.5 m/hr) with uniform torque and no suggestion that large junk remained at the bottom of the hole. The clean-out assembly was recovered and on deck by 1140 hr on 28 November. The contents of the junk basket consisted of about a half a bucket of basaltic debris, minor chert fragments, and ground-up metal filings.

The second B182×215 BCR was then connected to a new 9⁷/₈-in tricone bit fitted with three 2⁰/₃₂-in nozzles. The BCR was lowered and reentered the hole at 1755 hr on 28 November. The BCR had reached the bottom of the hole (267.1 mbsf) and was opening new hole by 2000 hr that evening. Drilling was terminated at midnight on 29 November at a depth of 276.1 mbsf. A total of 9.0 m of basement was drilled at an average ROP of 0.4 m/hr. Following the conclusion of the drilling, the hole was flushed with a 40-bbl sepiolite mud sweep. The drilling assembly was picked up above basement to 234 mbsf and lowered to the bottom of the hole. Following a wiper trip to 91 mbsf (inside the 20-in casing) and a return to 276.1 mbsf, the hole was once more flushed with a 50-bbl sepiolite treatment. There was no fill found at the bottom of the hole and no ledges or obstructions detected during the wiper trip. Subsequent to the last mud flush, the hole was displaced with a combination of 150 bbl of sepiolite mud and 100 bbl of heavy mud (10.5 ppg). The bit cleared the reentry cone at 0700 hr on 30 November.

At 1330 hr on 30 November, the bit cleared the rotary table. Inspection revealed that one of the cones from the tricone drilling bit was missing as well as many of the tungsten carbide inserts on the remaining cones. There was noticeable junk damage to the bit body. The BCR appeared to be in gauge with two inserts missing and some junk damage to the bottom sub. During the drilling there was no strong indication of cone loss and, in fact, the torque values for the last 5 hr of rotation were low with very little variation. It was difficult to assess if the cone came off early in the drilling and was ground up or dropped when the bit was picked up off bottom at the end of the hole. The missing cone had the same corresponding orientation relative to the location of the reamer cutting shell as the failed bearing of the tricone pilot bit used in the first BCR.

We decided to deploy the 16-in casing and then drill out the cement shoe with a C-4 RCB core bit mated to a junk basket. If the cone had been ground down in the drilling process, the junk basket would provide a means to clean some of the filings from the hole and we would

have been able to resume coring. If there was high erratic torque once the bit was lowered to the basalt, suggesting that the cone was more or less intact, then we would have needed to make a round trip and go back in with a milling assembly.

Installing the 16-in Casing

At 1330 hr on 30 November, the drill crew began to assemble the 16-in casing string. The total casing string length was 269.5 m. The top of the casing string was topped off with seawater, the Cam-Actuated Drill-Ahead (CADA) running tool was connected to the hanger, and the casing hanger was lowered through the moonpool at 0417 hr on 1 December.

As the casing was being deployed, the drill string was filled with seawater every 20 stands. At 1040 hr on 1 December, with the end of the casing string at 3092 mbrf, the vibration-isolated television camera captured the grim vision of a collapsed joint of casing (the fifth joint from the bottom of the string). The deployment of the casing string was aborted and the string was recovered.

Ultimately, four joints of casing were replaced, as was an additional casing collar damaged during the disassembly of the casing string. The joints above and below the collapsed casing had egg-shaped collars as a result of being directly mated to the collapsed joint and were replaced. Damage to a fourth joint of casing occurred while trying to unscrew a Baker-locked (epoxy) connection. The collapsed joint of casing was cut off in 5-ft sections and removed from the rig floor.

At 1135 hr on 2 December, the 16-in casing once more disappeared beneath the waters of the moonpool. This time, the drill string was filled with water every 10 stands to ensure that there would be no re-prise of collapsed casing. At 2008 hr the same day, the casing began to be lowered into the reentry cone. By this juncture, the wind had shifted and vessel motion became pronounced, with heave approaching 3 m. At 2215 hr and with heave hovering around 4 m, the reentry was terminated with the cement float shoe at 122 mbsf. If operations continued there was a very real possibility of damaging the casing and/or the reentry cone. The casing was pulled out of the cone and raised to 36 m above the seafloor to wait for calmer weather in which to proceed.

At 0545 hr the next day, the heave had reduced to 1.8 m and it was deemed safe to resume operations, after waiting on weather for 5.8 hr. Hole 1256D was reentered at 0650 hr. The bottom of the casing passed the sediment/basement interface without any drag, and by 1200 hr on 3 December the casing shoe was at 257 mbsf or ~7 m into basement. As the driller gently lowered the casing string, the casing stuck at 263 mbsf or ~6 m above casing landing depth. After the casing was worked for 3.75 hr, the string came free and the hanger was successfully landed in the reentry cone. Confirmation of the hanger engagement with the throat of the reentry cone was made by the application of 10,000 lb of overpull. The casing was cemented with 38 bbl of cement followed by 10 bbl of drill (fresh) water and chased by 213 bbl of seawater. The CADA running tool was released by clockwise rotation of the drill pipe at 1955 hr.

Cleaning Hole 1256D

The RCB BHA was assembled, lowered, and then reentered the cone at 1500 hr on 4 December. After the cement plug was drilled out, a core

barrel was dropped and the bit was carefully lowered to the bottom of the hole and rotation established. The hole was worked for a couple of hours, but erratic and fairly high torque suggested that metal fragments of the tricone bit cone that had broken off during reaming operation (see above) remained at the bottom of the hole. This was confirmed when the core barrel was recovered with a nose section of the drilling bit cone captured in the core catcher. A fresh barrel was dropped in attempt to recover some more fragments, but this was not successful. The drill string was then tripped to the rig floor, where a couple of metal fragments were found lodged between the cones and cutting guides.

A fishing assembly was made up of a 9-in fishing magnet and two junk baskets. The fishing magnet has been in inventory for many years, but this was the first time that it was used to “fish” metal junk from the bottom of the hole. The design of this tool incorporates a permanent magnet in which the magnetic flux is concentrated in a controlled field around the bottom pole plate of the unit. The pole plate is highly magnetic, with a strong field extending completely across the bottom of the tool. Because no magnetism emanates to any other part of the tool, the outside case is not magnetized and the tool can be deployed inside cased holes without losing its effectiveness. The tool has circulation holes that terminate at the bottom of the magnet, which resides inside the fishing (mill) guide.

The fishing assembly reentered Hole 1256D at 2358 hr on 5 December. At 0230 hr the next morning, the driller began working the junk baskets and the fishing magnet. The magnet was lowered to ~1 m from the bottom of the hole, and the pumps were cycled on and off in brief intervals at 80 to 100 spm (400 to 500 gpm) to stir up the material from the bottom for capture in the junk baskets. After 1 hr of working the fishing assembly, the drill string was recovered.

Once on deck, several pounds of metal ranging from fine cuttings to moderate-sized (~5 cm) fragments of cone were removed from the magnet. Significantly, there was very little material in the boot baskets, suggesting that the bottom of the hole was clean. When all the metal recovered from this exercise was combined with material retrieved previously from the bottom of the hole was weighed, it totaled 6 lb. The bottom of the hole was considered clean enough to run in with a core barrel.

RCB Coring in Basement

Basement drilling operations consist of coring with the RCB system for the life of a bit, which is ~60 to 65 hr of coring time. After each bit is recovered, a new bit is installed on the end of the BHA, the drill string is tripped to the reentry cone, the hole is reentered, and coring proceeds. We used six RCB coring bits, which includes five for coring in addition to the one already deployed for drilling out the cement plug and debris at the bottom of the hole, as discussed above.

An RCB BHA was assembled with a new RBI CC-7 bit (the second of six RCB bits used in Hole 1256D) and a junk basket and then was lowered into the reentry cone at 2130 hr on 6 December. Just before coring was started, the driller worked the junk basket to clean any small fragments that may have remained in the hole. Coring was initiated in Hole 1256D at 0100 hr on 7 December with generally very good results. The average recovery from 276.1 to 368.9 mbsf (Cores 206-1256D-2R through 15R) was an excellent 84.4%, with an average ROP of 2.3 m/hr. Some of the core barrels from this cored interval recovered >100%. The

recovery from 368.9 to 406.0 mbsf (Cores 206-1256D-16R through 21R) averaged 21.7%, with an average ROP of 3.8 m/hr. A drift measurement (deviation of the hole from vertical) made with the Tensor tool at 368.9 mbsf (119 m into basement) recorded an angle of 1.8°.

By the time the hole was deepened to 406.0 mbsf (156 m into basement), the bit had accumulated 49.6 hr. We decided to perform a round trip of the drill string to inspect the condition of the bit and use that as a basis for establishing the rotating hours to core before the next bit change. After pulling the bit up to 388 mbsf, the drill string became stuck. The driller could not lower or raise the drill pipe, although circulation was maintained. The drill string was worked free after 3 hr, following the application of up to 250,000 lb of overpull. The hole was backreamed from 387.6 to 254.0 mbsf and flushed with a 40-bbl sepiolite treatment on the way out of the hole. The bit was pulled free of the cone at 1435 hr on 10 December and was on deck at 2040 hr the same day. The bit was in excellent condition with no missing inserts, and no excessive wear was observed. The average recovery for the second bit run (the first bit was the one damaged by junk in the hole) was 67% with a cored interval of 129.9 m. The average ROP was 2.6 m/hr.

After attaching a new CC-7 RCB bit (the third bit) to the BHA, the ninth reentry of the leg was made at 0410 hr on 11 December. By 0845 hr, rotary coring in Hole 1256D resumed. The hole was deepened from 406.0 to 494.0 mbsf at an average ROP of 1.4 m/hr. The ROP values with this bit ranged from 3.2 m/hr to a lethargic 0.4 m/hr at the bottom of the interval. Rotary coring with this bit increased the penetration into basement from 156.0 m to 244.0 m (average recovery = 47%). A hole angle measurement was made at 451 mbsf (201 m into basement) and recorded a value of 0.8°.

After accumulating 62.9 rotating hours, the CC-7 bit was recovered. It was in good condition, considering the rotating hours in basement, and had sustained a few chipped teeth, some erosional wear, and was $\sim 1/8$ in under gauge. The tungsten carbide inserts exhibited normal dulling characteristics, but the loss of gauge and unknown remaining life in the bearings suggested that 60 to 65 rotating hours would be a prudent choice for the next bit.

The fourth bit, a new CC-9 RBI RCB bit, was attached to the BHA. The cutting structure of the CC-9 bit is only slightly less aggressive than the CC-7 but possesses more inserts on the surface of each bit cone. Because the CC-9 has a less invasive cutting surface than the CC-7, it should have a smoother cutting action in the very hard basalt at the bottom of the hole (ROP = ~ 0.5 m/hr). It was also felt that the smoother action of this core bit should result in improved recovery in the rubble zones between massive flows.

At 1435 hr on 15 December, the drill string entered the reentry cone, and by 1800 hr coring was resumed in Hole 1256D. At the request of the Co-Chief Scientists, a nonmagnetic core barrel was made up and deployed on odd-numbered cores starting with Core 206-1256D-39R (513.5 mbsf). By the afternoon of 18 December, the hole had been deepened to 552.5 mbsf, or 302.5 m into oceanic basement. After accumulating 57.8 rotating hours, the pipe was tripped and the bit was at the rotary table at 0740 hr on 19 December. The average recovery for this bit was 37% with an average rate of penetration of 1.3 m/hr. The used bit was found to be $\sim 1/8$ in under gauge and contained the expected dulling characteristics of a bit with 58 rotating hours in basement. The tungsten carbide inserts had sustained some chipping in the

nose and heel of the cones. There was minor erosional wear on the cone face, and the cone bearings were effective.

The fifth bit, a new CC-9 RBI RCB bit, was attached to the BHA, the pipe was tripped down, and Hole 1256D was reentered for the eleventh time at 1550 hr on 19 December. After the subsea camera was retrieved, coring was resumed at 1915 hr the same day. Routine coring continued until 2000 hr on 22 December. By this time, we had cored an additional 84.0 m into oceanic basement (average recovery = 40%) and amassed 59.4 rotating hours. The average rate of penetration for this bit was 1.4 m/hr, and the overall average rate of penetration stood at 1.7 m/hr. The average recovery for the hole had dropped to 50%. The depth of the hole was 655.0 mbsf, or 405.0 m below the sediment/basement interface. The bit was at rotary table at 0625 hr 23 December. It exhibited the same characteristics regarding cone wear and erosion as the previous CC-9 bit. The bit body was $\sim 1/16$ in under gauge.

The sixth and final CC-9 bit was attached to the BHA, and the pipe was tripped down to the reentry cone. The drill string reentered the cone at 1540 hr on 23 December after 1 hr of maneuvering the vessel in dynamic positioning mode. Coring in the hole resumed at 1845 hr that same day. Routine rotary coring deepened the hole to a total depth of 752.0 mbsf, or 502 m into basement, by noon on 27 December. The average recovery for the 97.0-m cored interval was 39% and was accomplished at an average ROP of 1.5 m/hr, or a total of 64.9 rotating hours. The overall average recovery for the hole was 47.8%. The average ROP for all coring bits was 1.6 m/hr.

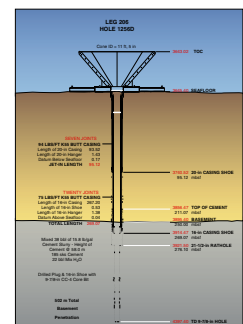
There was insufficient time to perform another bit change, so it was decided to recover the drill string and change the BHA to a logging configuration. The bit cleared the seafloor at 1515 hr on 27 December and was at the rotary table at 2300 hr. The bit was inspected and found to have lost teeth in the nose and heel area of the cones. There were also some chipped teeth and missing tungsten carbide inserts on the shank body, which was consistent with the experience of the previously recovered two CC-9 bits. The bit body was $1/16$ in under gauge.

Coring Summary for Hole 1256D

Coring in Hole 1256D began into a massive flow (igneous Unit 1256D-1) that extended from Core 206-1256D-2R (276.1 mbsf) to near the base of Core 12R (350.3 mbsf), for a thickness of ~ 74.2 m. The recovery in this unit was 93%. Below this, the recovery dropped and the penetration rate slowed, sometimes with rates as low as 0.5 m/hr. The low recovery can be attributed to a variety of reasons, the most important of which are related to the formation. The thin and fractured flows along with minor amounts of pillow basalt have a tendency to fragment when cored. These fragments would occasionally jam in the core catcher, core liner sleeve, and even the core liner and prevent additional core from being recovered. We removed the liner starting with Core 206-1256D-52R (600.7 mbsf) to reduce the prospects for rubble jamming associated with the core liner and liner sleeve. In an attempt to further improve recovery, we also frequently recovered a core barrel after a 4- to 5-m advance (half cores).

Hole 1256D was cased to 269 m, which is 19 m into basement, and was cored from 276.1 to 752.0 mbsf (Fig. F18; Tables T4, T5). The overall recovery in Hole 1256D was 47.8%, with 227.3 m of core recovered from 475.9 m cored. The average penetration rate for all coring bits was 1.6 m/hr.

F18. Reentry cone and casing installed in Hole 1256D, p. 57.



Logging

The logging BHA was made up of a drag-type open-throat bit without a float valve. The logging bit reentered the hole at 0622 hr on 28 December for the thirteenth and final time. The pipe was set to 60 m below the reentry cone. Five tool strings were deployed, starting with triple combo tool string. The borehole proved to be in very good shape and gave no problems on any of the logging runs. Very little debris had fallen into the hole between coring and logging operations, and, as a result, all tool strings could be lowered to ~750 mbsf, within ~2 m of the total hole depth.

The first pass of the triple combo tool string went smoothly from 750 up to 529 mbsf, at which point the wireline heave compensator (WHC) failed and could not be restarted. The triple combo tool string was run up to the pipe, and then a short repeat pass was made to overlap the interval from 529 mbsf to the pipe. The WHC was fixed after the triple combo run and was used without further difficulty on all subsequent runs. The caliper showed the average hole size to be ~12 in, with some of the hole being $9\frac{7}{8}$ in and the largest breakouts approaching 17 in.

The FMS-sonic tool string was deployed next. After lowering the tool string to the bottom of the hole, the FMS would not function, owing to a power problem. The sonic tool was functional, so we decided to log with it and then come out of the hole to troubleshoot the FMS problem. After removing the sonic tool, the FMS tool functioned properly and three passes were made.

The Bundesanstalt für Geowissenschaften und Rohstoffe (BGR) magnetometer was deployed on the next two logging runs, with a third attempt on the last run of the logging operations (see below). In all attempts, the tool failed because the gyro unit was consuming more power than could be supplied because of large rotations and vertical accelerations of the tool.

Two passes were made with the Ultrasonic Borehole Imager (UBI) on the next logging run, with the first pass being run slower (100 m/hr) for higher resolution (0.2-in resolution). This was the first time in the history of ODP that the UBI was used to image hard rocks. A repeat pass was made with the vertical resolution of 0.4 in.

The next tool to be deployed was the Well Seismic Tool (WST). The air gun was used, and 12 stations located along the igneous section were recorded. WST operations were delayed for 45 min because of the proximity of a pod of pilot whales to the experiment.

Finally, as time was available, the BGR magnetometer was redeployed and the speed to run the tool to pipe depth was slowed (600 m/hr, compared with the 3000 m/hr usually used). Unfortunately, at 3680 mbrf, operation of the tool ceased again, and logging was abandoned. Logging operations ended at 2030 hr on 30 December.

Transit to Balboa

Following logging, the pipe was tripped out of the hole, the beacon was recovered, and the ship was offset away from the reentry cone. The final pipe trip took 7 hr, with the logging bit clearing the rotary table at 0325 hr on 31 December 2002.

We got under way for Balboa, Panama, at 0330 hr on 31 December. The 824-nmi transit from Site 1256 took 75.5 hr at an average speed 10.9 kt, with the ship arriving at the Merchant Ship Anchorage at 0829 hr on 3 January 2003. After anchoring overnight, the pilot boarded the

ship at 0834 hr and the ship got under way, passing under the Bridge of Americas at ~1045 hr. Leg 206 officially ended with the first line to shore in Balboa, Panama, at 1100 hr on 4 January 2003.

PRINCIPAL RESULTS

Leg 206 is the first leg of a two-leg program to sample a complete section of upper oceanic crust through the extrusive lavas, sheeted dike complex, and into the upper oceanic gabbros. Site 1256 was drilled into ~15-m.y.-old crust formed during an episode of superfast accretion at the EPR. Seismic observations (e.g., Purdy et al., 1992) suggest an inverse relationship between spreading rate and the depth to axial low-velocity zones at mid-ocean ridges. These low-velocity zones are hypothesized to be partially molten magma chambers that, when frozen, will form the uppermost gabbros. If this is the case, gabbroic rocks should be at their shallowest in superfast spreading crust and drilling crust formed at this rate will provide the best opportunity to sample a complete section of upper oceanic crust. At least in terms of seismic structure, ocean crust formed at fast spreading rates is relatively simple and probably best conforms to the ideal stratigraphy envisioned for Penrose-type ocean crust. Although perhaps only 20% of the present-day mid-ocean ridges are spreading at fast rates (>80 mm/yr), ~50% of the present ocean basins formed at this style of ridge axis. Hence, one deep drill hole through a complete upper crustal section can be reasonably extrapolated to describe a significant portion of the Earth's surface.

Before we embarked on our major aims of drilling operations at Site 1256 it was first necessary to thoroughly characterize the sedimentary overburden above the oceanic crust and determine the stratigraphy, sedimentation and mass accumulation rates, and the role of fluid processes in the sedimentary blanket. Following the sampling of the sedimentary section, operations then concentrated on the underlying basement, and a reentry cone and casing string to basement were installed to enable deep drilling of the upper oceanic crust.

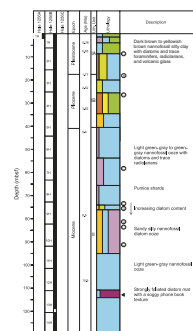
Four holes were drilled at Site 1256 (Table T4). Hole 1256A was a single piston core, shot to establish the mudline at Site 1256. In Hole 1256B, the complete sedimentary sequence was drilled by APC and XCB coring and the uppermost basement was tagged at 250.7 mbsf. Further samples of the sedimentary sequence were recovered by RCB drilling from 220.1 mbsf in Hole 1256C, and this pilot hole was drilled into the upper basement to a depth of 340.3 mbsf (88.5 m subbasement). After the successful installation of the reentry cone and casing strings to basement in Hole 1256D, coring of the lavas resumed and continued until the end of the leg, when the hole was prepared for wireline logging. Hole 1256D was opened to a total depth of 752 mbsf, or 502 m into basement. Hole 1256D was left clear of junk and in excellent condition for deepening during a future scientific drilling expedition.

Sedimentary Overburden at Site 1256

Lithostratigraphy

Drilling in Holes 1256A, 1256B, and 1256C recovered a complete section of the sedimentary stratigraphy at Site 1256 (Fig. F19). The sediments are subdivided into two principal lithologic subdivisions, al-

F19. Simplified lithostratigraphic column, Site 1256, p. 58.



though more complex structure is revealed by the paleomagnetism, geochemistry, and physical property investigations. Unit I is clay rich with a few carbonate-rich intervals, whereas Unit II is predominantly biogenic carbonate.

Lithologic Unit I (0–40.6 mbsf) comprises clay-rich sediments with Pleistocene dark brown to yellow-brown silty clays (Subunit 1A) (Table T6) with calcareous nannofossils, overlying light olive-gray to yellowish brown Pliocene to upper Miocene sandy clays to silts with calcareous nannofossil-rich intervals (Subunit IB). The Subunit IA/IB transition is taken as the Pleistocene/Pliocene boundary with a change in the relative contribution of clastic and biogenic components apparent in the color reflectance and magnetic susceptibility. Bioturbation is moderate to abundant throughout lithologic Unit I with *Planolites*, *Chondrites*, *Zoophycos*, and *Skolithos* the most common trace fossils identified. Rare volcanic ash is present in Unit I, and a quartz- and feldspar-rich ash layer was recovered in interval 206-1256B-3H-2, 34–36 cm.

Lithologic Unit II (40.6–250.7 mbsf) (Table T6) comprises upper Miocene to middle Miocene light greenish gray to dark gray calcareous nannofossil ooze with varying amounts of clay and other microfossil groups. Diatoms are a significant minor component that increase in abundance with depth, forming a siliceous biogenic ooze at 85 mbsf. With the exception of two intervals, the remainder of the sedimentary section is dominated by light greenish gray to white, nearly pure calcareous nannofossil ooze. Bioturbation is common throughout Unit II, and trace fossils include calcified solid and rind burrows as well as *Planolites* and *Skolithos*.

The interval from 111 to 115 mbsf consists of a laminated diatom mat comprising abundant tubular diatom tests with minor nannofossils. From 140 to 195 mbsf the nannofossil ooze has significant but variable clay and diatom components, which are most clearly recognized by changes in the color reflectance and density.

Chert nodules are a common feature in the sediments from ~111 mbsf down to the basement. Distinct chert layers at 111 and 158 mbsf were identified by increased resistivity and low porosity in the down-hole measurements, and very poor recovery in the lowermost sediment cores indicates that further chert layers are present between 230 mbsf and the basement. Red-brown iron oxide-rich silicified sediments directly overlie the basement (within 1 m), and these may be recrystallized metalliferous sediments.

Rare 5-cm-wide dark greenish gray granular glauconite bands were identified at 76–82 and 217–225 mbsf. At the base of the sedimentary sequence, the nannofossil ooze has a distinct pale bluish hue and X-ray diffraction determined a significant mica component, possibly celadonite or glauconite, in the sediment, perhaps derived from the recrystallization of biogenic opal and hydrothermally derived iron oxides.

Biostratigraphy

A biostratigraphic framework for Site 1256 has been established by the inspection of calcareous microfossil assemblages in core catcher and additional samples from the sedimentary sequence. Calcareous nannofossils are generally abundant and moderately to well preserved, albeit with some fragmentation. Assemblages above ~25 mbsf have been affected by etching and those below ~118 mbsf show the effects of dissolution and overgrowth. There was no evidence for significant reworking of fossils, and more than a dozen nannofossil datums were determined,

T6. Sedimentary overburden unit summary, p. 111.

providing a modest biostratigraphic resolution for the Pleistocene through middle Miocene (Table T7).

The biostratigraphic sequence at Site 1256 is generally similar to those recorded from nearby sites in the Guatemala Basin, Sites 844 and 845 (Mayer, Pisias, Janecek, et al., 1992). Sedimentation rates are discussed in greater detail below, but the drastic decrease from high (>35 m/m.y.) sedimentation rates in the eastern equatorial Pacific in the middle Miocene to much lower (8–14 m/m.y.) rates in the late Miocene, referred to as the “carbonate crash” (Farrell et al., 1995), is also observed at Site 1256.

Paleomagnetism

Alternating-field demagnetization of sedimentary split core sections and discrete samples was used to construct a magnetostratigraphic record of the sedimentary overburden at Site 1256. Nearly all chrons and subchrons are recorded from Chron C1n (Brunhes Chron; 0.0–0.780 Ma) through most of Subchron C5n.2n (9.920–10.949 Ma) (Figs. F20, F21; Table T8). The termination of Subchron C5n.2n (9.920 Ma) is clearly identified at 92.53 mbsf, but the onset of Subchron C5n.2n (10.949 Ma) could not be identified, either due to a coring gap or poor resolution of the characteristic remanent magnetization below 110 mbsf. From 110 mbsf to basement, the sediments have extremely weak intensities, resulting in a paleomagnetic signal dominated by noise. Thus, no polarity stratigraphy could be determined for this part of the sedimentary section.

The age assignments from Site 1256 magnetostratigraphy are in very good agreement with the biostratigraphic constraints from calcareous nannofossil datums (Fig. F22). The magnetostratigraphy provides higher resolution in the late Miocene up to the Brunhes/Matuyama reversal at 0.78 Ma, whereas the biostratigraphy provides constraints within the late Pleistocene, where there is an absence of polarity reversals, and in the middle Miocene, where the paleomagnetic signal was poorly resolved.

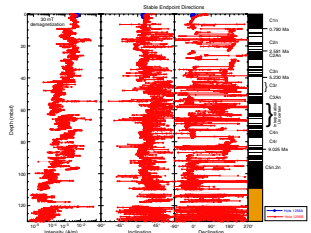
Sedimentation Rates

Sedimentation rates vary from ~6 to 36 m/m.y., with the rate being about four times faster in the middle Miocene than the average rate during the late Miocene to present (Fig. F23). Linear sedimentation rates were estimated for five intervals (Fig. F22) within which the slope of the age vs. depth data from the magnetostratigraphy and biostratigraphy was constant or nearly so (Fig. F22). The lowermost linear sedimentation rate is 36.4 m/m.y., calculated for interval 9.92–13.6 Ma (95–212.65 mbsf). When this rate is extrapolated to the basement at 250.7 mbsf, the mean age obtained for the basement is 14.6 Ma, consistent with the ~15-Ma age of the oceanic crust estimated from marine magnetic anomalies (Fig. F9).

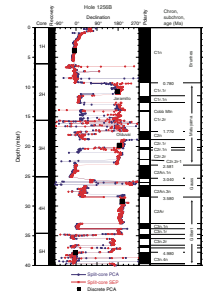
The high sedimentation rate in the middle Miocene can be attributed to the productivity being very high while the site was near the paleo-equator and to complete preservation on young, shallow seafloor above the lysocline. The more recent slower rates can be attributed to lower productivity away from the equator and to partial dissolution as the seafloor subsided toward the carbonate compensation depth (CCD). The rapid decrease in sedimentation rate in the late Miocene, however, requires an influence additional to the northward drift and subsidence

T7. Calcareous nannofossil datums, p. 112.

F20. Magnetostratigraphy from SEPs from split-core sections, p. 60.

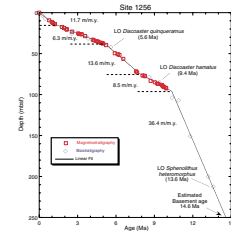


F21. Magnetostratigraphy from PCA and SEPs from split-core sections and discrete samples, p. 61.

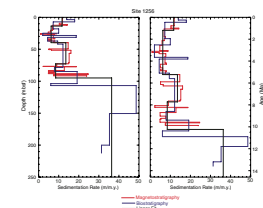


T8. Magnetostratigraphy, p. 113.

F22. Neogene age-depth plot, Hole 1256B, p. 64.



F23. Sedimentation rates, p. 65.



of the Site 1256 ocean crust. A similar pattern of sedimentation rate variations was observed at Sites 844 and 845, with the event that occurred at the end of middle Miocene being referred to as a carbonate crash (Farrell et al., 1995; Lyle et al., 1995). The carbonate crash extended from ~11.2 to 7.5 Ma, with the crash nadir at ~9.5 Ma in the equatorial Pacific (Farrell et al., 1995). Presumably, the beginning of the carbonate crash at Site 1256 corresponds to the base of the diatom mat (115 mbsf), which has an age of ~10.9 Ma. The carbonate content in this interval is ~12 wt%, whereas it averages ~79 wt% below. Although the density of carbonate analyses for Site 1256 is relatively low, the crash nadir would presumably occur in the vicinity of the extreme carbonate low (0.25 wt%) at 89.55 mbsf, which has an age of ~9.6 Ma (within Subchron 4Ar.2n). Late Miocene sedimentation rates in the tropical eastern Pacific are complex in detail and must reflect changes in either productivity or the CCD (Farrell et al., 1995; Lyle et al., 1995). Similar carbonate crash events are also observed in the Caribbean, and it has been suggested that the P_{CO_2} of ocean waters in this region may have been influenced by either the onset of North Atlantic Deep Water formation or the partial closing of the Panama Gateway (Lyle et al., 1995; Shipboard Scientific Party, 1997; Roth et al., 2000).

Geochemistry

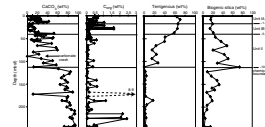
The sediment deposited at Site 1256 is composed of calcium carbonate, terrigenous grains, and biogenic silica with no discernible metalliferous component (Fig. F24). Total organic carbon concentrations are low throughout the sedimentary sequence. Calcium carbonate is dominant below 115 mbsf, although at 187 mbsf the terrigenous component increases to 20%. At ~115 mbsf, biogenic silica is the most abundant phase. Above 115 mbsf, the proportion of terrigenous material increases toward the surface and is the most important component in lithologic Unit I (above 40.6 mbsf).

Ba/Ti ratios are commonly used as a chemical proxy of the biogenic productivity in the overlying waters because sedimentary calcium carbonate, opal, and organic carbon are commonly altered during diagenesis. Ba/Ti ratios are between 2 and 10 in the upper 112 m of Site 1256, and values below 112 mbsf are within the range of 20 to 30, typical of the eastern equatorial Pacific Ocean (Fig. F25). There was a significant decrease in biogenic production following an extended episode of high productivity between 14.6 and 10.8 Ma, with the exception of a brief interval of low productivity at 12.9 Ma. More significantly, productivity decreased significantly at 10.8 Ma and has remained low to modern day. This change in productivity could be a response to the northward movement of the Cocos plate away from the equator, where productivity and, hence, Ba/Ti are commonly higher.

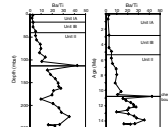
The primary influence on the interstitial water chemistry at Site 1256 is diffusive exchange between seawater and basement fluids (Fig. F26). A chert bed located at 159 mbsf and observed in the downhole logs is continuous enough to form a low-diffusivity barrier that causes abrupt jumps in cation (e.g., magnesium and calcium) concentrations in many of the depth profiles. The concentrations of lithium and potassium mimic those of magnesium in the interstitial waters and are strongly influenced by diffusion between seawater and basement.

The low organic carbon content limits the extent of pore water sulfate reduction ($SO_4^{2-} > 17.5$ mM), as seen in decreases in alkalinity in the pore waters with depth. Alkalinity, conversely, reflects the dissolu-

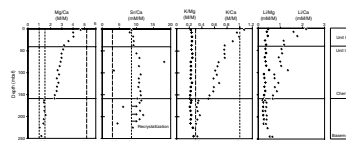
F24. Calcium carbonate, organic carbon, terrigenous matter, and biogenic silica, p. 66.



F25. Ba/Ti ratios, p. 67.



F26. Mg/Ca, Sr/Ca, K/Mg and K/Ca, and Li/Mg and Li/Ca, p. 68.



tion and reprecipitation of biogenic calcite, and this process is also shown by the increases in the Sr/Ca ratio of the pore waters with depth. Silica concentrations clearly illustrate the dissolution of biogenic organisms during diagenesis and the precipitation of chert.

Physical Properties

Changes in physical properties are mostly gradual downhole, with the exception of those properties that are sensitive to the major lithologic and compositional changes at the lithologic Unit I/Unit II boundary (40.6 mbsf), at the diatom mat (111–115 mbsf), and ~40–45 m above basement (at ~205–210 mbsf), below which chert and glauconite increase. Density and porosity are dominated by gradual compaction, with lesser effects of grain composition (Fig. F27). *P*-wave velocity is nearly uniform and low at ~1540 m/s, with a slight increase below 205 mbsf. Magnetic susceptibility is moderate in the clay-rich parts of lithologic Unit I and drops to very low in the nannofossil oozes.

Heat Flow

Downhole temperatures were measured during APC coring of Hole 1256B at depths of 53.6–158.1 mbsf and in the bottom water. Heat flow values average 113 mW/m², with a slight but possibly significant decrease downhole (Fig. F28). This value is close to the predictions for conductive cooling of oceanic lithosphere, implying that hydrothermal circulation is no longer a major mechanism of heat transport at Site 1256.

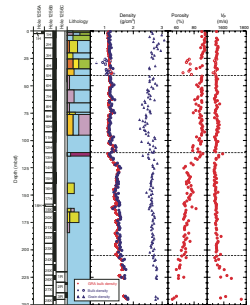
Ocean Crust Formed at Superfast Spreading Rate

Hole 1256C, our single-bit pilot hole, was cored 88.5 m into basement, and Hole 1256D, the cased reentry hole, was cored 502 m into basement during Leg 206. Hole 1256D is located ~30 m due south of Hole 1256C (see Fig. F17). The basement/sediment interface was encountered at 251.8 and ~250 mbsf in Holes 1256C and 1256D, respectively, in a water depth of 3634.7 m. Recovery from both holes was good, and excellent in places, with an average recovery of 61.3% and 47.8% in Holes 1256C and 1256D, respectively.

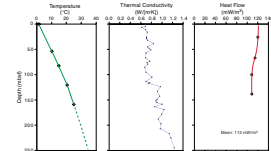
Igneous Stratigraphy

A summary of the igneous stratigraphy is presented in Figure F29. We divided the basement into 22 units in Hole 1256C and 26 units in Hole 1256D (Tables T9, T10). The igneous basement is dominated by thin (tens of centimeters to ~3 m) basaltic sheet flows separated by chilled margins, which make up ~60% of the cored interval in both holes. Massive flows (>3 m thick) are the second most common rock type in both holes, including the thick ponded flow near the top of each hole. Minor intervals of pillow lavas (~20 m) and hyaloclastite (a few meters) and a single dike were recovered in Hole 1256D. We drilled a massive ponded flow (~35 to >74 m thick) in both Holes 1256C and 1256D, which is a clear marker unit for correlation of the igneous stratigraphy between holes. So far we have been unable to determine the transition from axial eruptions to lavas that flowed out onto the ridge flanks; however, the thickness of some of the massive ponded flows requires significant basement relief in order to pool the magmas, which

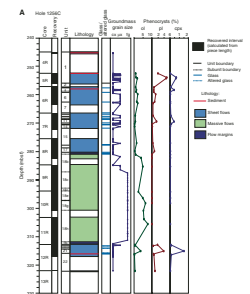
F27. Bulk density, grain density, porosity, and *P*-wave velocity, p. 69.



F28. Temperature, thermal conductivity, and heat flow, Hole 1256B, p. 70.



F29. Summary of basement stratigraphy, p. 71.



T9. Igneous unit and contact log, Hole 1256C, p. 114.

T10. Igneous unit and contact log, Hole 1256D, p. 115.

would only be developed significantly off axis (>3–5 km) (e.g., Macdonald et al., 1996).

Upper Units of Hole 1256C (Units 1256C-1 to 1256C-17)

The upper 27 m of basement in Hole 1256C (251.8–278.7 mbsf) is composed of thin basaltic sheet flows a few tens of centimeters to ~3 m thick, separated by chilled margins and containing rare intervals of recrystallized sediment (Fig. F29). The basalt is aphyric to sparsely phyric, with plagioclase, olivine, and clinopyroxene phenocrysts (in order of decreasing abundance). The groundmass is cryptocrystalline to microcrystalline in flow interiors, decreasing in average grain size toward the margins (Fig. F30), and preserving glassy margins in some cases (Fig. F29; Table T11).

Massive Pondered Flow: Igneous Units (1256C-18 and 1256D-1)

Units 1256C-18 and 1256D-1 each consist of a single cooling unit of cryptocrystalline to fine-grained basalt, which we interpret as a pondered lava flow. A total of 32 m of this unit was cored in Hole 1256C, of which 29 m was recovered. In Hole 1256C the deformed upper surface of the flow was encountered at 280.27 mbsf and consists of ~75 cm of cryptocrystalline to glassy aphyric basalt. The groundmass of the interior of the flow is fine grained but abruptly becomes cryptocrystalline ~1.5 m from the base of the flow. The base of the flow has been deformed and recrystallized, probably during and shortly after emplacement (Fig. F31).

This pondered flow is much thicker in Hole 1256D than in Hole 1256C, and although an exact thickness of the flow in Hole 1256D cannot be calculated because the top was not cored, the flow has a minimum thickness of 74.2 m. Although the top of Unit 1256D-1 is somewhat shallower than the top of Unit 1256C-18 (<276.1 mbsf, compared to 280.27 mbsf in Hole 1256C), we interpret the two units to be parts of a single pondered lava flow where the interior at the locations of both holes was liquid at the same time. The dramatic increase in thickness over 30 m of lateral distance suggests steep paleotopography, with Hole 1256D deeper in the depression that was filled in by the flow.

Lower Units of Hole 1256D (1256D-2 to 1256D-26)

The remainder of the section in Hole 1256D (with the exception of Units 1256D-3, 4a, 4c, 8c, 16d, and 21) consists of sheet flows tens of centimeters to ~3 m thick with uncommon massive flows 3.5–16 m thick (see Table T10). These flows are aphyric to sparsely phyric, cryptocrystalline to microcrystalline basalt and are distinguished by chilled margins or by increasing grain size toward the interiors of flows where the margins were not recovered (Fig. F32). Chilled margins are common, and the locations of glass and altered glass in the hole are compiled in Table T11.

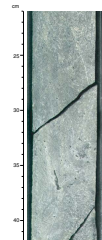
We distinguished pillow basalt from thin sheet flows on the presence of curved glassy margins oblique to the sides of the core and radial pipe vesicles oriented perpendicular to the chilled margins. We cored one ~20-m-thick interval of aphyric to sparsely phyric cryptocrystalline pillow basalt with glassy chilled margins near the top of the section (Unit 1256D-3). We recovered two hyaloclastite intervals in the basement (Subunit 1256D-4c and Unit 1256D-21) (Fig. F33). These intervals consist of angular to rounded clasts of basaltic glass several centimeters to <10 cm in diameter and smaller (<1 cm) curved shards of glass within a matrix of altered glass. We also recovered an interval of volcanic breccia

F30. Typical texture of sheet flow interior, p. 73.



T11. Locations of glass, Holes 1256C and 1256D, p. 116.

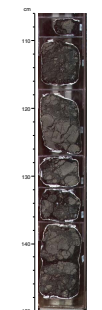
F31. Folded recrystallized material at base of pondered flow, p. 74.



F32. Typical textures of massive lavas and thin sheet flows, p. 75.



F33. Hyaloclastite consisting of glassy blocks and angular clasts, p. 76.



composed of angular fragments of cryptocrystalline basalt embedded in a matrix of altered glass (Subunit 1256D-4a) (Fig. F34).

Petrography

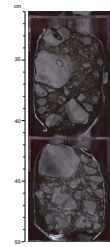
The basalts show a large variation in grain size and textures from holohyaline in the outermost chilled margins of lava flows and hyaloclastite clasts through aphanitic groundmass, consisting of cryptocrystalline varioles, to the coarser intergranular textures in the lava pond. The basaltic lavas are dominantly aphyric to sparsely phytic, with 72% of the examined thin sections having <5 vol% phenocrysts and 18% being aphyric (Fig. F35). The modal peak for Site 1256 is slightly shifted toward higher abundance of phenocrysts when compared to sheeted dikes from Hole 504B, which formed at an intermediate spreading rate but which are also dominantly aphyric (Dick, Erzinger, Stokking, et al., 1992) with a sharp peak at <2 vol% phenocrysts. In contrast, flows and dikes from the slow-spreading MAR show bimodal phenocryst abundance with peaks at <10 and >18 vol% (Bryan and Moore, 1977; Hekinian, 1982; Hodges, 1978; O'Donnell and Presnall, 1980; Sato et al., 1978; Shipboard Scientific Party, 1988).

Phenocrysts are dominantly olivine (average = 68% among all phenocrysts for Hole 1256C and 70% for Hole 1256D) with subordinate amounts of plagioclase (average = 31% among all phenocrysts for Hole 1256C and 25% for Hole 1256D) and clinopyroxene phenocrysts (average = 5.4% among all phenocrysts for Hole 1256C and 4.7% for Hole 1256D). Most clinopyroxene is augite. Rare spinel is present in a few samples as tiny inclusions in completely altered olivine phenocrysts.

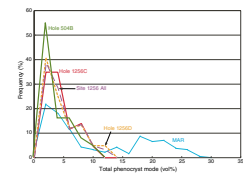
The ratio of three phenocryst phases (clinopyroxene, plagioclase, and olivine) is shown in Figure F36 compared to the sheeted dikes from Hole 504B and lava flows and dikes from the MAR. Nearly 50% of the basalt lavas from Site 1256 plot on the plagioclase-olivine join. The Hole 504B dikes mostly contain all three major phases and have slightly higher proportions of clinopyroxene than the Site 1256 lavas. In contrast, the majority of the MAR lavas and dikes plot on the plagioclase-olivine join. With respect to both the phenocryst abundance and proportions, the Site 1256 lavas have intermediate characteristics between these two extremes.

Olivine is the most common phenocryst phase (0.1–11 vol%), but fresh olivine was found only within fresh glass of some chilled margins of lava flows and hyaloclastite. Plagioclase is the second most abundant phenocryst phase and is mostly subhedral to euhedral crystals clotted together or with clinopyroxene, though discrete euhedral platy to stubby crystals are also present. Most plagioclase phenocrysts from Hole 1256C and from the upper units of Hole 1256D are unzoned. Zoning is more common in lower units from Hole 1256D, and crystals may be either normally or reversely zoned or both. Normally zoned plagioclases commonly have clear cores with euhedral outlines, surrounded by thin, less calcic rims. Inclusions are uncommon except for some glass blebs and clinopyroxene aligned along twin planes of the host plagioclase (Fig. F37). Much less common is plagioclase with resorbed cores, mottled with bleblike inclusions of clinopyroxene, magnetite, and glass, and enclosed in a less calcic mantle. In contrast, reversely zoned plagioclase has dusty resorbed cores with euhedral, more calcic mantles, which are enclosed by sodic rims. The dusty inclusions are small skeletal to dendritic magnetite, tiny acicular clinopyroxene, and thin plagioclase laths and pale brown glass mostly altered to clay minerals. Al-

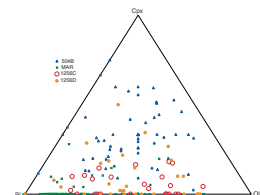
F34. Cryptocrystalline basalt embedded in altered glass, p. 77.



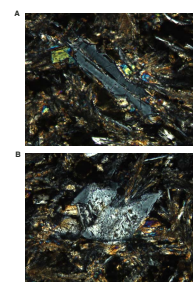
F35. Modal abundance of phenocrysts in basalts, p. 78.



F36. Phenocrystic Cpx-Pl-Ol in basalts, p. 79.



F37. Plagioclase phenocryst clots, p. 80.



though clinopyroxene is the least abundant phenocryst phase, it is present in >40% of the thin sections examined. Augite phenocrysts are typically subhedral to euhedral, stubby to short prismatic crystals that commonly form crystal clots with platy plagioclase. The most common variety is black to dark green augite, but a pale yellowish green prismatic pyroxene that resembles the groundmass pigeonite in the coarse basalt lava from the massive ponded lava flow is also observed.

The groundmass is composed of plagioclase, augite, and magnetite, with or without minor amounts of glass, pigeonite, green clinopyroxene, quartz, apatite, and granophyric intergrowths of quartz and sodic plagioclase. Dark green clinopyroxene is present as the outermost rims surrounding augite and pigeonite and as a discrete prismatic crystal in the coarser fine-grained basalt. Groundmass clinopyroxene and plagioclase show a variety of textures that correspond to different cooling rates or the degree of undercooling but are mostly radially arranged to form spheroidal or fan-shaped crystal aggregates. Groundmass plagioclase is present as very tiny acicular crystals, thin planar laths, curved very thin planar crystals, skeletal fan-shaped or bowtie-shaped crystals in finer-grained samples, and platy and more stubby crystals in coarser-grained samples. Pigeonite is much less abundant than augite and commonly forms intergrowths with augite, where prismatic pigeonite is sandwiched between pale brown-green augite lamellae. Dendritic chains to equant skeletal crystals of Fe-Ti oxide minerals are a ubiquitous groundmass phase. In coarser-grained samples, host magnetite has exsolved ilmenite lamellae during cooling. Fine-grained and some microcrystalline basalts contain interstitial mesostasis of quartz-albite granophyric to vermicular intergrowths, quartz, granular to prismatic clinopyroxene (mostly altered to secondary clay minerals), acicular apatite, and dendritic to skeletal magnetite

Lava Pond (Units 1256C-18 and 1256D-1)

Unit 1256C-18 is a >30-m-thick massive lava body that begins at 280.3 mbsf with a holohyaline-cryptocrystalline lava surface, which develops downhole into intergranular to coarse variolitic fine-grained massive basalt and to cryptocrystalline, recrystallized basalt at the base of the flow (312 mbsf). The uppermost 0.7 m is composed of aphanitic lava with folded glassy chilled margins and volcanic rubble, including glassy clasts, and is interpreted as the folded and jumbled surface crust of a lava flow. The basal 1.6 m is unusual aphanitic basalt consisting of deformed and recrystallized variolitic groundmass and late magmatic veins. In Hole 1256D we encountered a fine-grained massive lava (Unit 1256D-1) from the first core at 276.1 mbsf, ~4 m above the top of Unit 1256C-18, which continued downhole to 350 mbsf. Unit 1256D-1 is lithologically correlated to the thick massive lava unit in Hole 1256C but is much thicker (>74 m thick) and lacks both the quenched upper surface and the basal recrystallized basalt lava. Such a thick lava flow could potentially have formed as a lava pond, where rapidly delivered lava accumulated in a depression, or as an inflated sheet flow, with slowly delivered lava confined by its own chilled margin. We interpret these massive basaltic units to be a thick ponded lava and not an inflated sheet flow on the following grounds:

1. The absence of inflation-related structures on the upper surface of and within the massive lava;
2. The absence of fine-grained coalesced flow lobe contacts;

3. The largest groundmass grain size and highest incompatible element concentrations present in the upper part of the massive lava body, suggesting the presence of a more differentiated late solidified melt horizon in the upper one-third of the lava body; and
4. The scarcity of subhorizontal vesicle-rich layers and segregated melt lenses commonly observed in inflated sheet flows elsewhere in Hole 1256D.

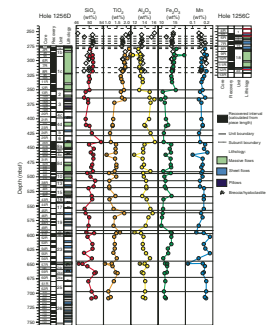
The ponding of such a massive lava flow (>74 m thick) requires a significant basement topography near the axis to pool the magma. Small basement faults with throws of ~100 m are apparent in the site survey seismic sections of the region surrounding Site 1256, and faults of such magnitude are commonly observed 5–10 km from the axis of the EPR (Macdonald et al., 1996). The very smooth basement topography at Site 1256 may result from the infill of small ridge flank grabens by large lava flows. The topography required to accumulate such thick lava suggests that magma may have flowed a significant distance off axis (>5 km) before ponding. Assuming that the ponded lava drilled at Site 1256 has not merely filled an isolated small depression but has pooled against some form of buttress, it would have a significant volume (5×10^4 to 1×10^6 m³/m of ridge crest). Such an eruption would drain a significant fraction of the lava in an axial melt lens if, in fact, these geophysically imaged features are the source of the magmas (10×10^4 to 2×10^5 m³/m of ridge crest). Very large lava flows, with much larger volumes than those needed to supply the massive ponded flow at Site 1256, have been discovered on modern fast-spreading ridges (e.g., 8°S EPR) (Macdonald et al., 1989).

Geochemistry

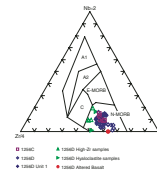
Petrographically fresh samples were selected from the basement cores of Holes 1256C and 1256D and analyzed for major and trace element concentrations using the shipboard inductively coupled plasma-atomic emission spectrophotometer (ICP-AES). There are general downhole variations, with Mg#, Cr, Ni, and Ca/Al ratios broadly increasing with depth, whereas TiO₂, Fe₂O₃, Zr, Y, Nb, V, and Sr broadly decrease with depth (Fig. F38). Superimposed on these broad trends are smaller-scale variations, for example, near-constant Mg# in lavas of Units 1256D-2 through 1256D-6 that is higher than those in the units immediately above and below. On a Zr-Y-Nb ternary diagram (Fig. F39), all lavas from Site 1256 plot in the N-MORB field.

TiO₂ and Zr behave similarly, as demonstrated by a relatively coherent pattern of increasing TiO₂ with increasing Zr (Fig. F40). Two groups are apparent on this diagram, one more evolved group with high Zr and TiO₂, which includes all samples from Hole 1256C and Unit 1256D-1, and a single sample from deeper in Hole 1256D. The deeper samples (>365 mbsf) from Hole 1256D form the low-Ti, low-Zr group. Relatively high Ti and Zr in the shallow samples is consistent with their lower Mg# and higher concentrations of incompatible elements and suggests that they are more evolved than deeper lavas. Two anomalous groups of lavas are notable compared to this general trend of decreasing evolution with depth: one group of samples within Unit 1256C-18 that have very high K₂O (Fig. F41) and one group of four samples with anomalously high Zr for a given TiO₂ value.

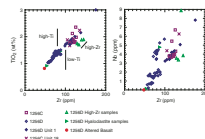
F38. Shipboard geochemical analyses, p. 81.



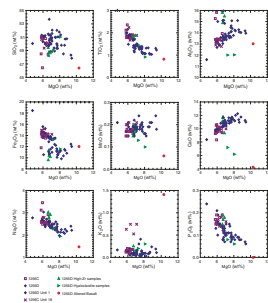
F39. Nb-Zr-Y ternary diagram, p. 86.



F40. Zr vs. TiO₂ and Nb, p. 87.



F41. Elemental abundance vs. MgO, p. 88.



The massive ponded flow forms the majority of the evolved group distinguishable on the Zr vs. TiO₂ diagram, but samples from 294 to 306 mbsf in Hole 1256C (approximately the middle to lower two-thirds of Unit 1256C-18) have exceptionally high K₂O (0.53–0.74 wt%, compared with 0.05–0.20 wt% for other Hole 1256C and Unit 1256D-1 samples). This order-of-magnitude increase in K₂O coincides with an increase in natural gamma radiation (NGR) measurements, but neither the chemical nor the NGR anomaly are apparent in Hole 1256D. This large increase in K₂O is not matched by variations in Mg# or other measures of fractionation, and some other explanation must be invoked, such as an along-rift geochemical zonation in source composition or tapping a small pod of more evolved magma or local assimilation of an unknown high-K sediment or altered lava.

In the lavas directly below the large massive flow there is a sharp increase in Mg# accompanied by a simultaneous increase in some trace elements with widely varying compatibility (e.g., Zr, Sr, Ni, and Cr) in Unit 1256D-2 (Fig. F38). The combination of high Mg# and high incompatible element concentrations argues against differentiation as the cause of the enrichments and suggests that there is variation in the primitive magma composition.

Alteration

Rocks from throughout Holes 1256C and 1256D exhibit a dark gray background alteration, where the rocks are slightly to moderately altered, olivine is replaced, and pore spaces are filled by saponite and minor pyrite. This background alteration is reflected in the distribution of dark gray rocks (Fig. F42) and of pyrite and saponite (e.g., Fig. F43) and is the result of low-temperature seawater interaction at low cumulative seawater/rock ratios.

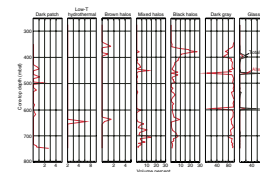
The local effects of late magmatic/hydrothermal fluids are restricted to within the massive ponded lava near the top of the section (Units 1256C-18 and 1256D-1, i.e., mainly at 276–330 mbsf). These effects include granophyric intergrowths of plagioclase and quartz in veins and interstitial areas, secondary green clinopyroxene reaction rims on primary augite, trace interstitial biotite and blue-green phyllosilicate biotite (chlorite?), and partial replacement of primary calcic plagioclase by albite.

Vein-related alteration is manifested as different-colored alteration halos along veins. The black halos contain celadonite and have been interpreted to result from the presence of upwelling distal low-temperature hydrothermal fluids enriched in iron, silica, and alkalis (Edmond et al., 1979; see summary in Alt, 1999). The iron oxyhydroxide-rich mixed halos are later features, which formed by circulation of oxidizing seawater. The biotite has a similar origin and formed along fractures that were not bordered by previously formed black halos.

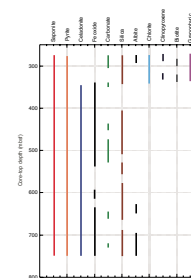
This vein-related alteration occurs irregularly throughout Hole 1256D below the massive Unit 1256D-1 but is concentrated in two zones, at 350–450 and 635–750 mbsf (Fig. F44). These zones correspond to peaks in frequency and proportion of celadonite and iron oxyhydroxide veins and minima in the abundance of pyrite veins (Figs. F45, F46). These were likely zones of greater permeability and, consequently, increased fluid flow.

Vein carbonate is more common above ~530 mbsf, but despite lower frequency of occurrence, overall higher abundances are present at greater depths (Figs. F44, F46). The absolute amount of CaCO₃ in the

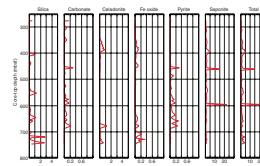
F42. Distributions of alteration types, p. 90.



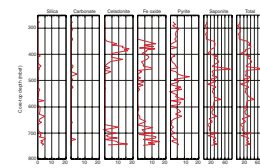
F43. Distribution of secondary minerals, p. 91.



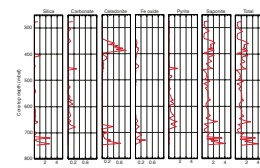
F44. Secondary minerals contained in veins, breccia, and interflow sediment, p. 92.



F45. Abundance of secondary mineral veins, p. 93.



F46. Volume percent secondary mineral veins, p. 94.



basement as Site 1256 is very low relative to other basement sites (Alt and Teagle, 1999).

Three peaks in glass abundance are present at 400, 460, and 600 mbsf (Fig. F42), corresponding to hyaloclastites in the core. These are important because of the substantial degree of glass alteration with the presence of saponite cementing the breccia, resulting in corresponding peaks in the abundances of secondary minerals (saponite) at these depths (Fig. F44).

The appearance of albite and saponite partially replacing plagioclase below 625 mbsf indicates a change in alteration conditions (Figs. F43, F44). This change may result in part because of slightly higher temperatures at depth or more evolved fluid compositions (e.g., decreased K/Na and elevated silica).

Overall, the basalts recovered from Site 1256 do not exhibit a general decrease in seawater interaction with depth and there is no simple decrease in the number of alteration halos or the amount of iron oxyhydroxide with depth. In contrast, alteration appears to have been concentrated in different zones that may be related to the architecture of the basement such as lava morphology, distribution of breccia and fracturing, basement topography, and the influence of these on porosity and permeability.

Alteration of the basement section of Hole 1256D is compared with other sites in Figure F47. Compared with most of these sites, Hole 1256D contains much smaller amounts of brown, mixed, and black alteration halos. The abundance of carbonate veins in Hole 1256D is also lower than at many other sites. Site 1256 is, however, quite similar to another section of crust generated at a fast-spreading ridge, Site 801. The latter site, however, contains two low-temperature hydrothermal deposits and associated intense hydrothermal alteration. One important feature is the lack of any oxidation gradient with depth in Hole 1256D, in contrast to the stepwise disappearance of iron oxyhydroxide and celadonite in Hole 504B and the general downward decrease in seawater effects at Sites 417 and 418.

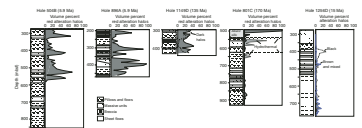
Structure

Both primary magmatic and postmagmatic structures were described in the basement rocks of Holes 1256C and 1256D. Primary igneous features include magmatic fabrics, laminations, flattened vesicles, folds, shear-related structures, late magmatic veins, and fracturing. Postmagmatic structures include veins, shear veins, microfaults, joints, and breccia. The distribution of these features is shown in Figure F48.

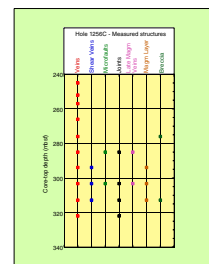
Late magmatic features are mainly restricted to within the massive ponded lava near the top of the basement and include felsic veins (usually >0.5 mm wide) and glassy veins (usually <0.5 mm wide). Felsic veins are characterized by quartz + alkali feldspar (or albite) symplectites showing a granophyric texture ± clinopyroxene ± magnetite ± plagioclase ± apatite. Glassy veins are almost totally replaced by saponite, which grows with face-controlled geometries and is commonly associated with vesicles and amygdules. Late magmatic veins are either planar features, or fill tension gashes or form sigmoidal pull-aparts. Some late magmatic veins show evidence of multiple episodes of folding. Shear bands and tension gashes that cut these folds indicate a progressive transition from predominantly ductile to brittle-ductile deformation.

Veins are the most prominent structural features observed in rocks recovered from Holes 1256C and 1256D. Veins mostly have a planar or

F47. Distribution of alteration zones, p. 95.



F48. Measured structures, p. 96.



To estimate the amount of fluid intrusion into the recovered cores, chemical and particulate tracers were deployed in Hole 1256C. Perfluoro(methylcyclohexane) was used as the chemical perfluorocarbon tracer (PFT) and 0.5- μm latex fluorescent microspheres were used as the particulate tracer. The tracer tests were conducted while coring Cores 206-1256C-7R, 9R, and 11R with the RCB. The PFT tests indicated drilling fluid intrusion into the center of the core in amounts above the detection limit. Fluorescent microspheres were rare in the crushed interior of the rock, even though they were detected on the outside of the cores and in the drill water. The low abundance of microspheres detected in the interior of the cores indicates very low levels of drill water intrusion, which is consistent with the PFT tests.

Downhole Measurements

A full suite of logging tools were run in Hole 1256D following the suspension of coring operations (Fig. F52). The tools utilized, in order of deployment, were the triple combo tool string, the FMS-sonic tool string, the BGR gyromagnetometer, the UBI, and the WST. This is the first time the UBI has been used in a hard rock hole. Because of tool failure during the first attempts to run the BGR magnetometer, this tool was rerun following the completion of the WST experiment. Unfortunately, despite lowering the BGR tool at a very slow rate (600 m/hr), rapid rotational and vertical accelerations resulted in an unusually high current demand by the gyro and failure of the instrument before it entered the open hole.

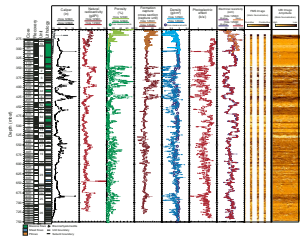
Hole 1256D was in excellent condition, and no constrictions or ledges impeded the passage of the various wireline strings throughout the logging schedule. Caliper readings from both the triple combo and the FMS tool strings show the borehole diameter to be mostly between 11 and 14 in, with only four short intervals >16 in. The hole conditions were ideal for those tools that require contact with the wall of the borehole. Despite the limitations of deploying the UBI tool in a larger than optimal borehole, many fractures were imaged by the tool.

The downhole measurements and images recorded show large variability, reflecting the massive units, lava flows, pillow lavas, and hyaloclastites recovered in Hole 1256D. Combined measurements of FMS and UBI coupled with other measured parameters will allow the stratigraphy of different rock types and flow thicknesses to be determined and structural features to be measured (Fig. F52). Multiple passes by the GPIT allow the cored basement to be subdivided into a number of magnetic subunits that will be compared with observed variations in rock type postcruise.

Whole-Core Images

The exterior of all whole-round core pieces that could be rotated smoothly through 360° were imaged on the DMT Digital Color Core-Scan system. Correlations between the whole-round core images and electrical or acoustic representations of the borehole wall, derived from downhole log measurements, allow determination of the true core depth (as opposed to ODP curated depth) in intervals with greater or less than 100% recovery. Distinctive features such as lithologic boundaries, fractures, veins, and breccias can be depth-matched to allow repositioning of core pieces. The certainty of the correlation will vary with recovery, the continuity of the pieces, and the number of distinctive

F52. Downhole logging results, p. 101.



features within a particular interval. Individual pieces or sequences of pieces that can be correlated can then be shifted to the appropriate depths with respect to the log data. This enables direct comparison between structural, physical, and chemical properties measured on the core and those recorded downhole.

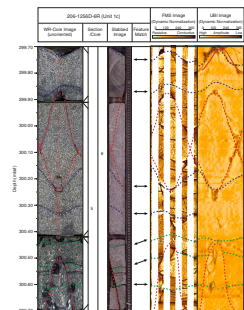
Individual core pieces (and associated structural data) that can be confidently depth-matched can then ultimately be reoriented or rotated so they are oriented with respect to true geographic north using data from the GPIT, which is included in the tool string with both the FMS and the UBI. Preliminary attempts at correlation and reorientation of core pieces, using the methods described in Haggas et al. (2001), show potentially good matches between the unrolled core images and the FMS and UBI data from Hole 1256D (Fig. F53). Because the procedures involved in correlating the whole-round core images to FMS and UBI images are very time intensive, further depth matching and core reorientation will be completed postcruise.

CONCLUSIONS

During Leg 206 we successfully accomplished the initial phase of a multileg drilling program that aims to sample a complete section of upper oceanic crust through the extrusive lavas, the sheeted dike complex, and into the gabbros. The main achievements of Leg 206 include the following:

1. Installed a reentry cone and large-diameter (20 and 16 in) casing through the 250 m of sediment overlying basement and 19 m into basement, with the lower portion cemented in place. The cone and casing allow multiple reentries and maintain hole stability, both essential for deepening Hole 1256D through the dikes and into gabbros. The large-diameter casing leaves open the possibility that at least two more casing strings could be installed in Hole 1256D should future legs need to isolate unstable portions of the hole.
2. Achieved moderate to high recovery through the upper 502 m of the igneous oceanic crust created by superfast seafloor spreading, which has allowed us to characterize the upper crust as a sequence of massive flows and thin sheet flows with minor amounts of pillow basalts and breccias. The sequence is slightly altered and has N-MORB composition. It was extruded over sufficient time to record stable geomagnetic field directions and to capture transitional directions in the upper units as the geomagnetic field reversed.
3. Recorded a full sequence of downhole logs, including the first images obtained by the UBI in hard rock in an ODP hole. Additional high-resolution images from the FMS should aid in orienting and positioning cores as well as filling in coring gaps in the igneous stratigraphy of Hole 1256D.
4. Concluded operations with Hole 1256D clean of debris, in excellent condition, and ready for the next phase of deep ocean crust drilling.

F53. Unrolled core images and FMS/UBI images, p. 102.



REFERENCES

- Alt, J.C., 1999. Very low grade hydrothermal metamorphism of basic igneous rocks. In Frey, M., and Robinson, D. (Eds.), *Very Low Grade Metamorphism*: Cambridge (Blackwell), 169–201.
- , in press. Alteration of the upper ocean crust: mineralogy, chemistry, and processes. In Elderfield, H., and Davis, E. (Eds.), *Hydrogeology of the Ocean Crust*: Cambridge (Cambridge Univer. Press).
- Alt, J.C., Laverne, C., Vanko, D.A., Tartarotti, P., Teagle, D.A.H., Bach, W., Zuleger, E., Erzinger, J., Honnorez, J., Pezard, P.A., Becker, K., Salisbury, M.H., and Wilkens, R.H., 1996. Hydrothermal alteration of a section of upper oceanic crust in the eastern equatorial Pacific: a synthesis of results from Site 504 (DSDP Legs 69, 70, and 83, and ODP Legs 111, 137, 140, and 148.) In Alt, J.C., Kinoshita, H., Stokking, L.B., and Michael, P.J. (Eds.), *Proc. ODP, Sci. Results*, 148: College Station, TX (Ocean Drilling Program), 417–434.
- Alt, J.C., and Teagle, D.A.H., 1999. The uptake of carbon during alteration of ocean crust. *Geochim. Cosmochim. Acta*, 63:1527–1535.
- Bickle, M.J., and Teagle, D.A.H., 1992. Strontium alteration in the Troodos ophiolite: implications for fluid fluxes and geochemical transport in mid-ocean ridge hydrothermal systems. *Earth Planet. Sci. Lett.*, 113:219–237.
- Bryan, W.B., and Moore, J.G., 1977. Compositional variations of young basalts in the Mid-Atlantic Ridge rift valley near lat 36°49'N. *Geol. Soc. Am. Bull.*, 88:556–570.
- Cande, S.C., and Kent, D.V., 1995. Revised calibration of the geomagnetic polarity timescale for the Late Cretaceous and Cenozoic. *J. Geophys. Res.*, 100:6093–6095.
- Cande, S.C., Raymond, C.A., Stock, J., and Haxby, W.F., 1995. Geophysics of the Pitman Fracture Zone and Pacific-Antarctic plate motions during the Cenozoic. *Science*, 270:947–953.
- Carbotte, S., Mutter, C., Mutter, J., and Ponce-Correa, G., 1997. Influence of magma supply and spreading rate on crustal magma bodies and emplacement of the extrusive layer: insights from the East Pacific Rise at lat 16°N. *Geology*, 26:455–458.
- COSOD II, 1987. *Rep. 2nd Conf. Scientific Ocean Drilling*: Washington/Strasbourg (JOIDES/European Sci. Found.).
- Detrick, R., Collins, J., Stephen, R., and Swift, S., 1994. In situ evidence for the nature of the seismic Layer 2/3 boundary in oceanic crust. *Nature*, 370:288–290.
- Detrick, R.S., Harding, A.J., Kent, G.M., Orcutt, J.A., Mutter, J.C., and Buhl, P., 1993. Seismic structure of the southern East Pacific Rise. *Science*, 259:499–503.
- Detrick, R.S., Toomey, D.R., and Collins, J.A., 1998. Three-dimensional upper crustal heterogeneity and anisotropy around Hole 504B from seismic topography. *J. Geophys. Res.*, 103:30485–30504.
- Dick, H.J.B., Erzinger, J., Stokking, L.B., et al., 1992. *Proc. ODP, Init. Repts.*, 140: College Station, TX (Ocean Drilling Program).
- Dick, H.J.B., and Mével, C., 1996. *The Oceanic Lithosphere and Scientific Drilling into the 21st Century*. Woods Hole, MA (ODP-InterRidge-IAVCEI).
- Edmond, J.M., Measures, C., Magnum, B., Grant, B., Sclater, F.R., Collier, R., Hudson, A., Gordon, L.I., and Corliss, J.B., 1979. On the formation of metal-rich deposits at ridge crests. *Earth Planet. Sci. Lett.*, 46:19–130.
- Farrell, J.W., Raffi, I., Janecek, T.R., Murray, D.W., Levitan, M., Dadey, K.A., Emeis, K.-C., Lyle, M., Flores, J.-A., and Hovan, S., 1995. Late Neogene sedimentation patterns in the eastern equatorial Pacific. In Piasias, N.G., Mayer, L.A., Janecek, T.R., Palmer-Julson, A., and van Andel, T.H. (Eds.), *Proc. ODP, Sci. Results*, 138: College Station, TX (Ocean Drilling Program), 717–756.
- Francheteau, J., Armijo, R., Cheminée, J.L., Hekinian, R., Lonsdale, P., and Blum, N., 1992. Dyke complex of the East Pacific Rise exposed in the walls of Hess Deep and the structure of the upper oceanic crust. *Earth Planet. Sci. Lett.*, 111:109–121.

- Gillis, K.M., and Roberts, M.D., 1999. Cracking at the magma–hydrothermal transition: evidence from the Troodos ophiolite, Cyprus. *Earth Planet. Sci. Lett.*, 169:227–244.
- Haggas, S., Brewer, T.S., Harvey, P.K., and Iturrino, G., 2001. Relocating and orienting cores by the integration of electrical and optical images: a case study from Ocean Drilling Program Hole 735B. *J. Geol. Soc. London*, 158:615–623.
- Hekinian, R., 1982. *Petrology of the Ocean Floor*: Amsterdam (Elsevier).
- Hodges, F.N., 1978. Petrology and chemistry of basalts from DSDP Leg 46. In Dmitriev, L., Heirtzler, J., et al., *Initial Repts., DSDP*, 46: Washington, D.C. (U.S. Govt. Printing Office), 227–233.
- Hooft, E.E.E., Detrick, R.S., and Kent, G.M., 1994. Seismic structure and indicators of magma budget along the southern East Pacific Rise. *J. Geophys. Res.*, 102:27.
- Hooft, E.E.E., Schouten, H., and Detrick, R.S., 1996. Constraining crustal emplacement processes from the variation of seismic Layer 2A thickness at the East Pacific Rise. *Earth Planet. Sci. Lett.*, 142:289–309.
- Karson, J.A., Klein, E.M., Hurst, S.D., Lee, C.E., Rivizzigno, P.A., Curewitz, D., Morris, A.R., and Hess Deep 1999 Scientific Party, 2002. Structure of uppermost fast-spread oceanic crust exposed at the Hess Deep Rift: implications for subaxial processes at the East Pacific Rise, *Geochem. Geophys. Geosyst.*, 3, 10.1029/2001GC000155.
- Kent, G.M., Harding, A.J., Orcutt, J.A., Detrick, R.S., Mutter, J.C., and Buhl, P., 1994. Uniform accretion of oceanic crust south of the Garrett transform at 14°15'S on the East Pacific Rise. *J. Geophys. Res.*, 99:9097–9116.
- Lyle, M., Dadey, K.A., and Farrell, J.W., 1995. The late Miocene (11–8 Ma) eastern Pacific carbonate crash: evidence for reorganization of deep-water circulation by the closure of the Panama Gateway. In Pisias, N.G., Mayer, L.A., Janecek, T.R., Palmer-Julson, A., and van Andel, T.H. (Eds.), *Proc. ODP, Sci. Results*, 138: College Station, TX (Ocean Drilling Program), 821–838.
- Macdonald, K.C., Fox, P.J., Alexander, R.T., Pockalny, R., and Gente, P., 1996. Volcanic growth faults and the origin of Pacific abyssal hills. *Nature*, 380:125–129.
- Macdonald, K.C., Haymon, R., and Shor, A., 1989. A 220 km² recently erupted lava field on the East Pacific Rise near lat 8°S. *Geology*, 17:212–217.
- Mayer, L., Pisias, N., Janecek, T., et al., 1992. *Proc. ODP, Init. Repts.*, 138 (Pts. 1 and 2): College Station, TX (Ocean Drilling Program).
- Menard, H.W., 1964. *Marine Geology of the Pacific*: New York (McGraw-Hill).
- Murray, R.W., Schrag, D.P., and Wheat, C.G., 2002. *Opportunities in Geochemistry for Post-2003 Ocean Drilling*: Tyngsboro, MA (JOI/USSSP).
- O'Donnell, T.H., and Presnall, D.C., 1980. Chemical variations of the glass and mineral phases in basalts dredged from 25°–30°N along the Mid-Atlantic Ridge. *Am. J. Sci.*, 280A:845–868.
- Ocean Drilling Program, 1996. *Understanding Our Dynamic Earth through Ocean Drilling: Ocean Drilling Program Long Range Plan Into the 21st Century*: Washington (Joint Oceanographic Institutions).
- Phipps Morgan, J., and Chen, Y.J., 1993. The genesis of oceanic crust: magma injection, hydrothermal circulation, and crustal flow. *J. Geophys. Res.*, 98:6283–6297.
- Plank, T., Ludden, J.N., Escutia, C., et al., 2000. *Proc. ODP, Init. Repts.*, 185 [CD-ROM]. Available from: Ocean Drilling Program, Texas A&M University, College Station TX 77845-9547, USA.
- Pollack, H.N., Hurter, S.J., and Johnson, J.R., 1993. Heat flow from the Earth's interior: analysis of the global data set. *Rev. Geophys.*, 31:267–280.
- Purdy, G.M., Kong, L.S.L., Christeson, G.L., and Solomon, S.C., 1992. Relationship between spreading rate and the seismic structure of mid-ocean ridges. *Nature*, 355:815–872.
- Raitt, R.W., 1963. The crustal rocks. In Hill, M.N. (Ed.), *The Sea—Ideas and Observations on Progress in the Study of the Seas* (Vol. 3): *The Earth Beneath the Sea*: New York (Wiley-Interscience), 85–102.

- Richardson, C.J., Cann, J.R., Richards, H.G., and Cowan, J.G., 1987. Metal-depleted root zones of the Troodos ore-forming hydrothermal systems, Cyprus. *Earth Planet. Sci. Lett.*, 84:243–253.
- Roth, J.M., Droxler, A.W., and Kameo, K., 2000. The Caribbean carbonate crash at the middle to late Miocene transition: linkage to the establishment of the modern global ocean conveyor. In Leckie, R.M., Sigurdsson, H., Acton, G.D., and Draper, G. (Eds.), *Proc. ODP, Sci. Results*, 165: College Station, TX (Ocean Drilling Program), 249–273.
- Sato, H., Aoki, K., Okamoto, K., and Fujita, B., 1978. Petrology and chemistry of basaltic rocks from Hole 396B, IPOD/DSDP Leg 46. In Dmitriev, L., Heirtzler, J., et al., *Initial Repts., DSDP*, 46: Washington, D.C. (U.S. Govt. Printing Office), 115–141.
- Schiffman, P., and Smith, B.M., 1988. Petrology and oxygen isotope geochemistry of a fossil seawater hydrothermal system within the Solea Graben, northern Troodos ophiolite, Cyprus. *J. Geophys. Res.*, 93:4612–4624.
- Shipboard Scientific Party, 1988. Site 648. In Detrick, R., Honnorez, J., Bryan, W.B., Juteau, T., et al., *Proc. ODP, Init. Repts.* (Pt. A), 106/109: College Station, TX (Ocean Drilling Program), 52–53.
- , 1997. Site 998. In Sigurdsson, H., Leckie, R.M., Acton, G.D., et al., *Proc. ODP, Init. Repts.*, 165: College Station, TX (Ocean Drilling Program), 49–130.
- Shor, E.N., 1985. A chronology from Mohole to JOIDES. In Drake, E.T., and Jordan, W.M. (Eds.), *Geologists and Ideas; A History of North American Geology*. Spec. Publ.—Geol. Soc. Am., 4:391–399.
- Stein, C.A., and Stein, S., 1994. Constraints on hydrothermal heat flux through the oceanic lithosphere from global heat flow. *J. Geophys. Res.*, 99:3081–3096.
- Stephen, R.A., Kasahara, J., Acton, G.D., et al., 2003. *Proc. ODP, Init. Repts.*, 200 [CD-ROM]. Available from: Ocean Drilling Program, Texas A&M University, College Station TX 77845-9547, USA.
- Teagle, D.A.H., Alt, J.C., and Halliday, A.N., 1998. Tracing the chemical evolution of fluids during hydrothermal recharge: constraints from anhydrite recovered in ODP Hole 504B. *Earth Planet. Sci. Lett.*, 155:167–182.
- Vanko, D., and Laverne, C., 1998. Hydrothermal anorthitization of plagioclase within the magmatic/hydrothermal transition at mid-ocean ridges: examples from deep sheeted dikes (Hole 504B, Costa Rica Rift) and a sheeted dike root zone (Oman ophiolite). *Earth Planet. Sci. Lett.* 162:27–43.
- Vine, F.J., and Matthews, D.H., 1963. Magnetic anomalies over oceanic ridges. *Nature*, 199:947–949.
- Wilson, D.S., 1996. Fastest known spreading on the Miocene Cocos-Pacific plate boundary. *Geophys. Res. Lett.*, 23:3003–3006.
- Worm, H.-U., Böhm, V., and Bosum, W., 1996. Implications for the sources of marine magnetic anomalies derived from magnetic logging in Holes 504B and 896A. In Alt, J.C., Kinoshita, H., Stokking, L.B., and Michael, P.J. (Eds.), *Proc. ODP, Sci. Results*, 148: College Station, TX (Ocean Drilling Program), 331–338.

Figure F1. Scientific drilling of the oceanic lithosphere, 1968–2003. World map of the oceans showing the distribution of drill holes into in situ ocean basement formed at mid-ocean ridges. Despite >30 yr of ocean drilling, there are still relatively few drill holes in oceanic crust and a very poor sampling distribution in terms of basement depth, crustal age, and spreading rate. Note the clustering of drill sites along the Mid-Atlantic Ridge and in the eastern Pacific Ocean. Stars = holes drilled by DSDP and ODP.

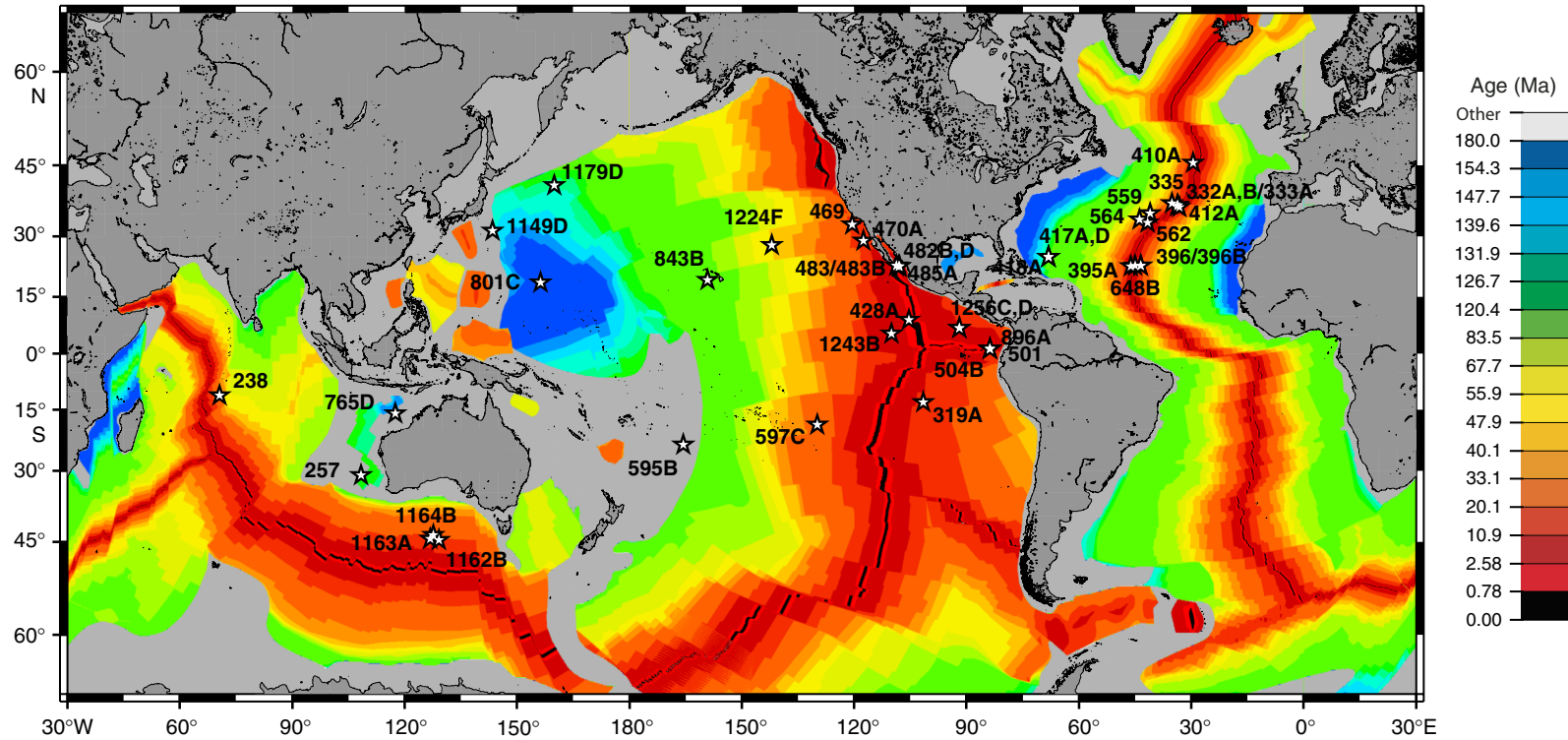


Figure F2. Basement age vs. depth of basement penetration for scientific drill holes >50 m into in situ ocean crust formed at mid-ocean ridges. Note that the boundaries between the erupted lavas, the dike-lava transition zone, and the sheeted dike complex/upper gabbro boundary are placed at arbitrary depths based loosely on Hole 504B stratigraphy. Predictions based on marine seismic reflection studies indicate that the combined thickness of the lava-dike sequences should decrease with spreading rate, but this is yet to be tested and whether it is the dikes or lavas that is thinned is so far unknown. Black lines = DSDP drill holes, blue lines = ODP drill holes, red lines = Holes 1256C and 1256D.

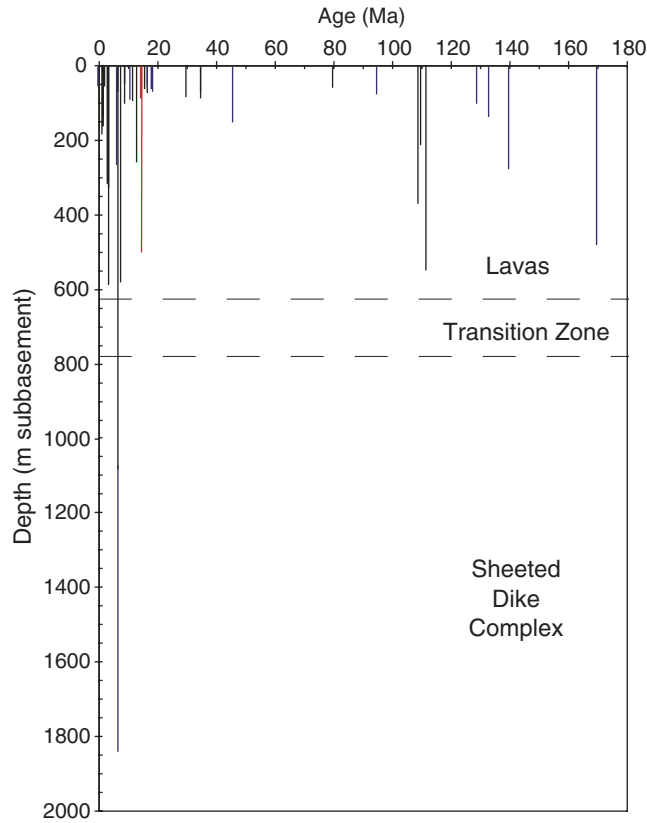


Figure F3. Depth of penetration of drill holes into in situ basement subdivided by ocean basin. Black lines = DSDP drill holes, blue lines = ODP drill holes, red lines = Holes 1256C and 1256D.

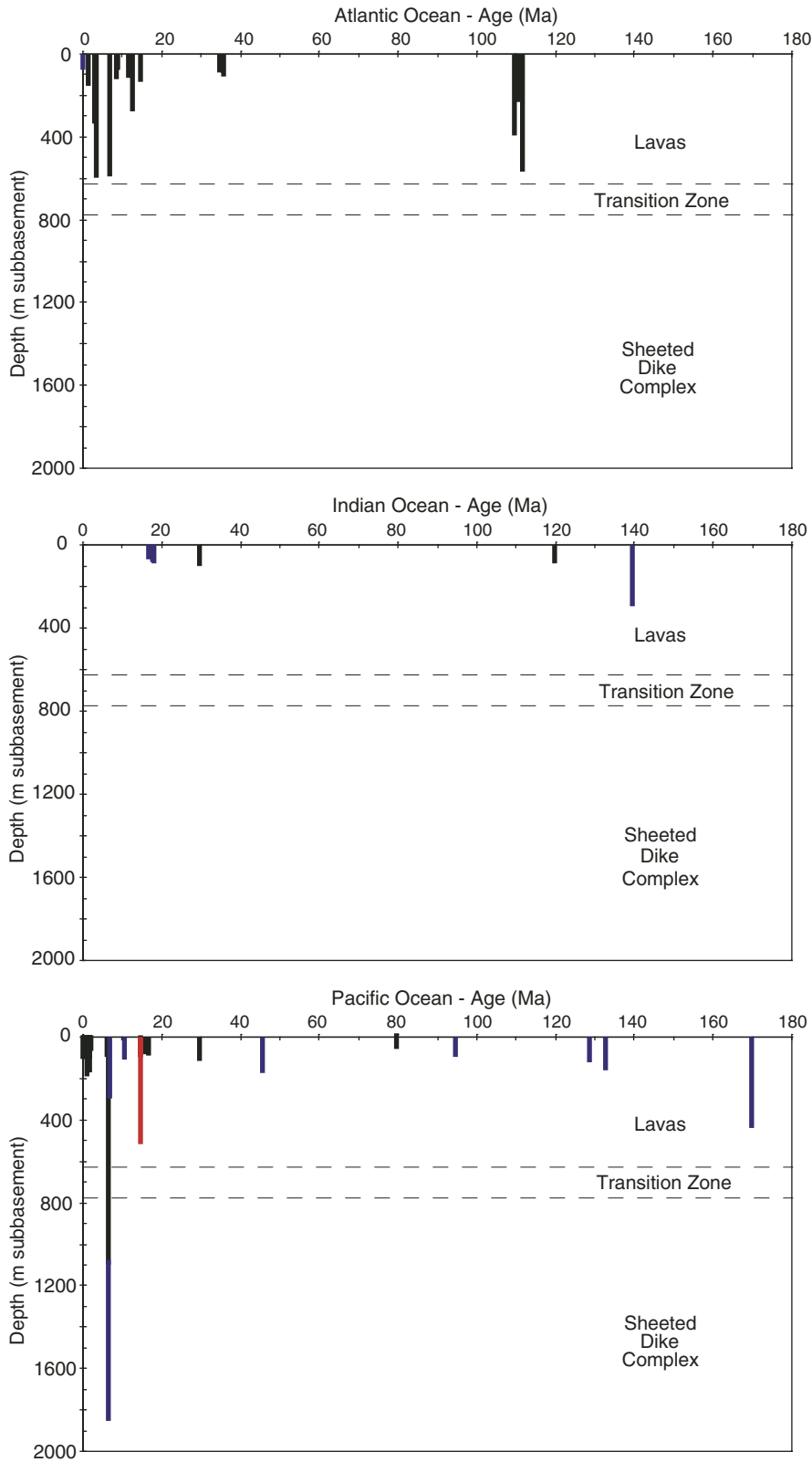


Figure F4. Depth of penetration of drill holes into in situ basement clustered by broad spreading rate subdivisions where slow < 40 mm/yr < intermediate < fast < 80 mm/yr. Black lines = DSDP drill holes, blue lines = ODP drill holes, red lines = Holes 1256C and 1256D.

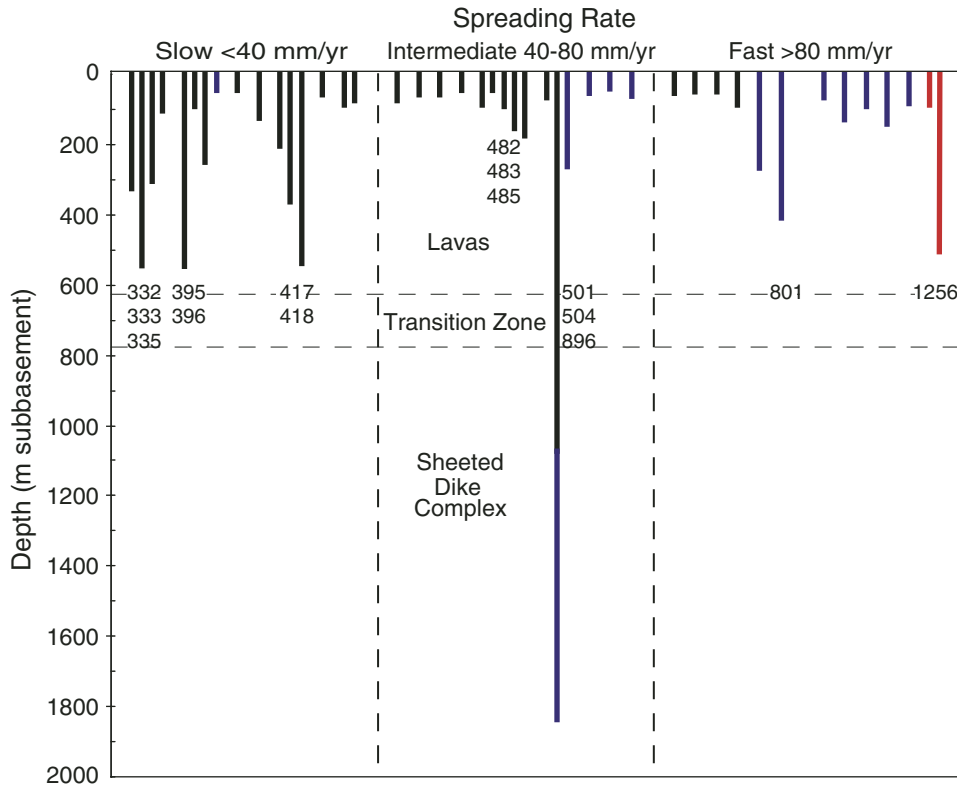


Figure F5. Schematic cross section of oceanic crust created by superfast seafloor spreading (after Karson et al., 2002). Approximate boundaries of seismic layers are given to the left. Black arrows = subsidence of gabbroic matrix, yellow arrows = deformation related to faulting, fracturing, and block rotation in the sheeted dikes and lower lavas.

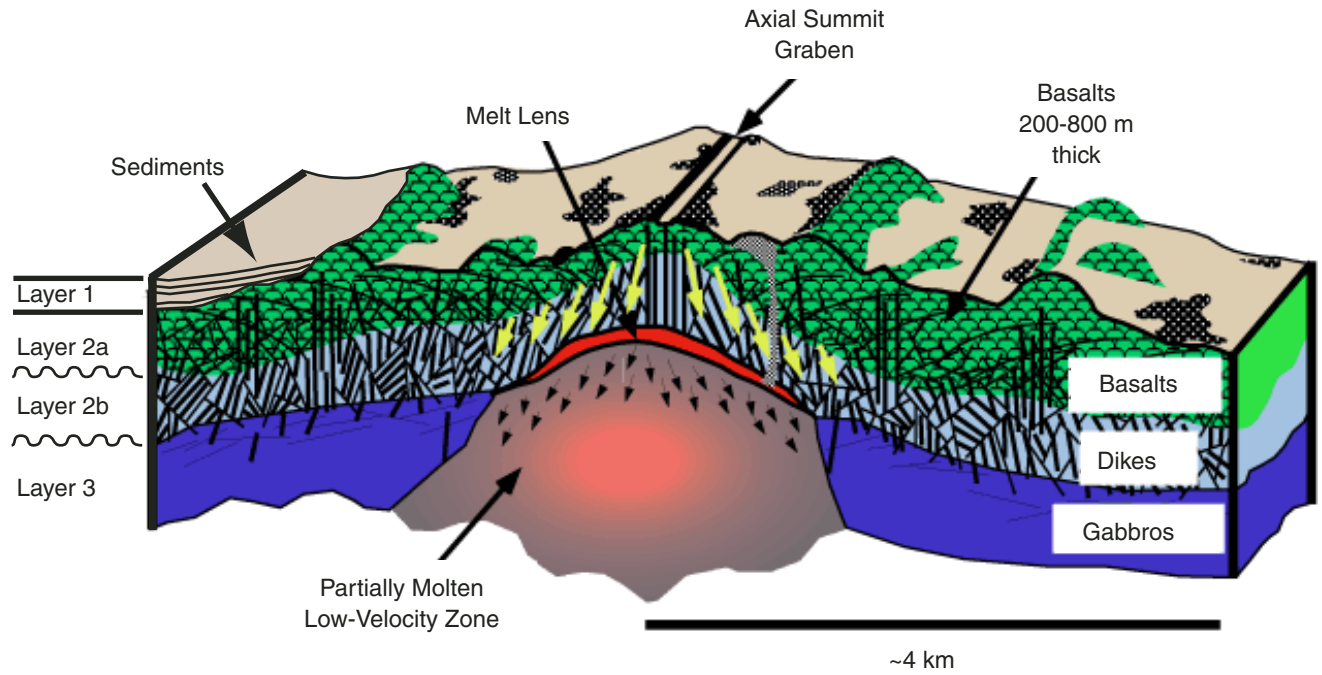


Figure F6. Depth to axial low-velocity zone plotted against spreading rate, modified from Purdy et al. (1992) and Carbotte et al. (1997). Depth vs. rate predictions from two models of Phipps Morgan and Chen (1993) are shown, extrapolated subjectively to 200 mm/yr (dashed lines). Penetration to date in Holes 504B and 1256D is shown by solid vertical lines. MAR = Mid-Atlantic Ridge, EPR = East Pacific Rise, JdF = Juan de Fuca Ridge, Lau = Valu Fa Ridge in Lau Basin, CRR = Costa Rica Rift.

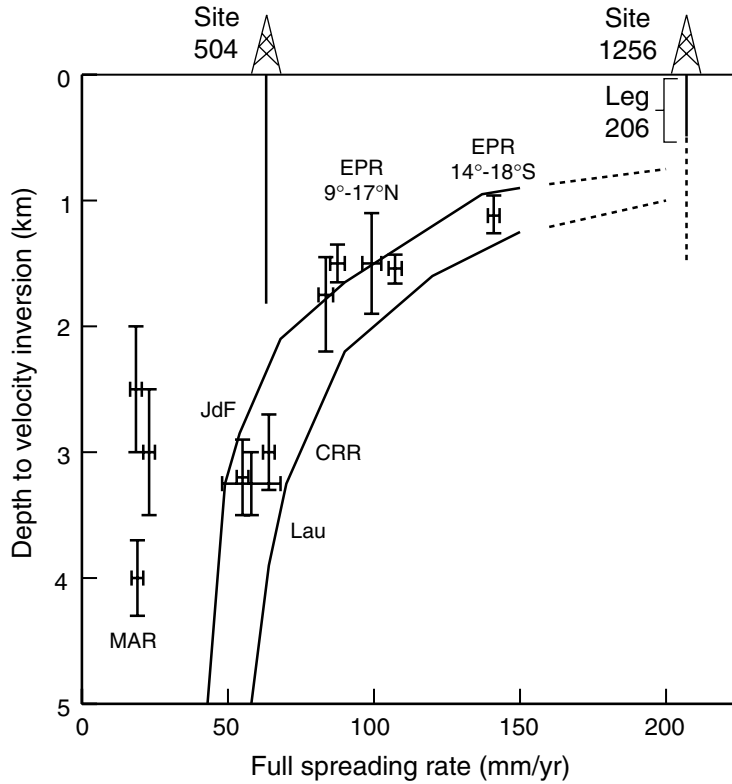


Figure F7. Age map of the Cocos plate and corresponding regions of the Pacific plate. Isochrons at 5-m.y. intervals have been converted from magnetic anomaly identifications according to the timescale of Cande and Kent (1995). Selected DSDP and ODP sites that reached basement are indicated by circles. The wide spacing of 10- to 20-m.y. isochrons to the south reflects the extremely fast (200–220 mm/yr) full spreading rate. Dashed box shows location of figure showing details of magnetic anomalies near Site 1256 (Fig. F8, p. 47). FZ = fracture zone.

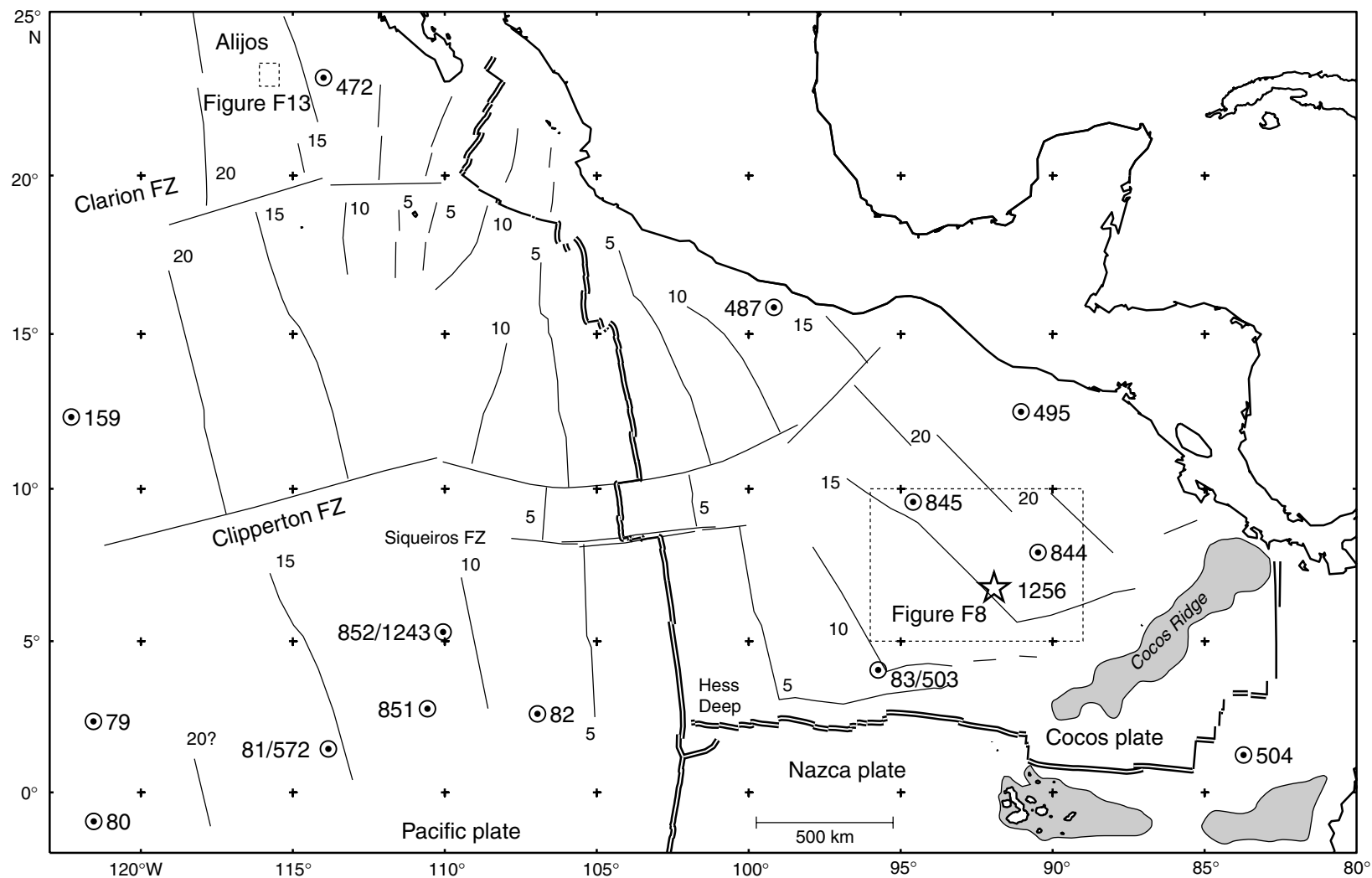


Figure F8. Details of isochrons inferred from magnetic anomalies near Site 1256. Gray shading shows normal magnetic polarity, based on digitized reversal boundaries (small circles; after Wilson, 1996). Bold line shows location of Guatemala basin multichannel seismic tracklines from the site survey conducted in March–April 1999. Dashed boxes show the locations shown in Figures F10, p. 49, F11, p. 50, and F12, p. 51. Anomaly ages: 5A = ~12 Ma, 5B = ~15 Ma, and 5D = ~17 Ma.

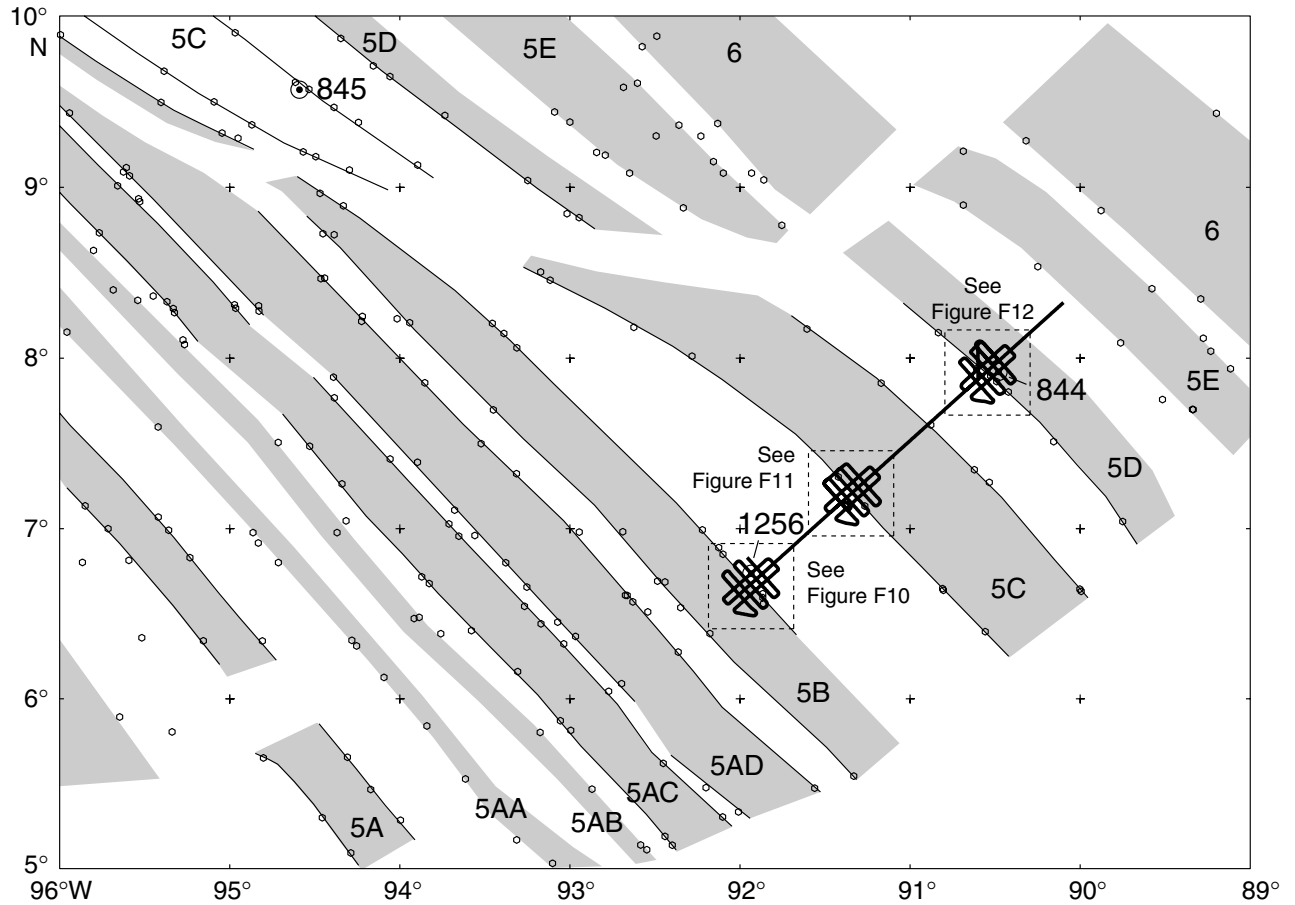


Figure F9. Reconstruction of Site 1256 and vicinity at 14 Ma, ~1 m.y. after formation of the site at the East Pacific Rise. Positions and plate velocities (arrows labeled in millimeters per year) are relative to the Antarctic plate, which is reasonably fixed relative to the spin axis and hotspots. Reconstructed positions of mapped magnetic Anomalies 5B, 5C, and 6 (ages 15–20 Ma), and existing DSDP/ODP drill sites are shown by shaded bars and circles, respectively.

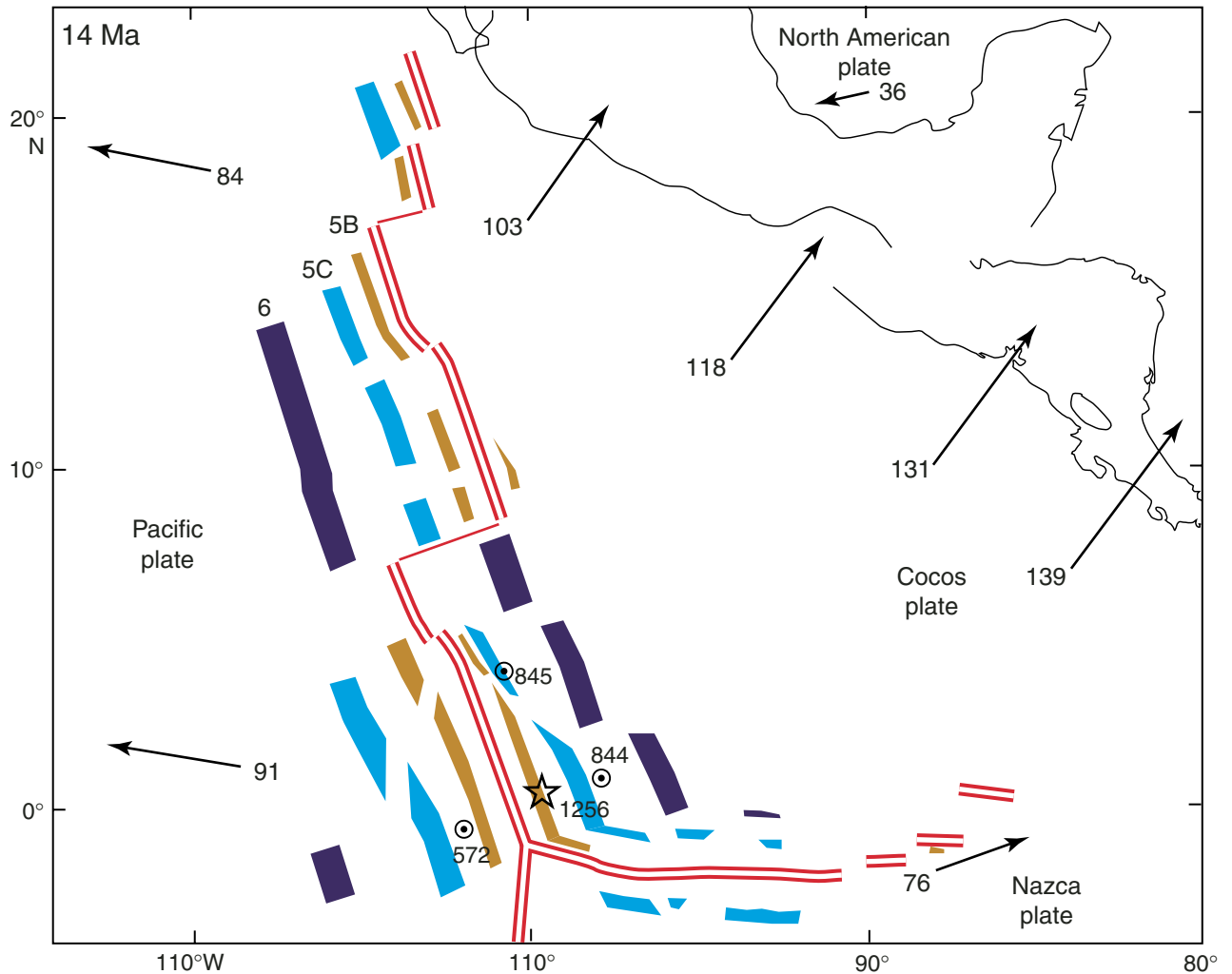


Figure F10. Bathymetry and site survey track map for Site 1256 (proposed Site GUATB-03). Abyssal hill relief of up to 100 m is apparent in the southwest part of the area; relief to the northeast is lower and less organized. Line numbers 21–28 identify multichannel seismic (MCS) lines for subsequent figures.

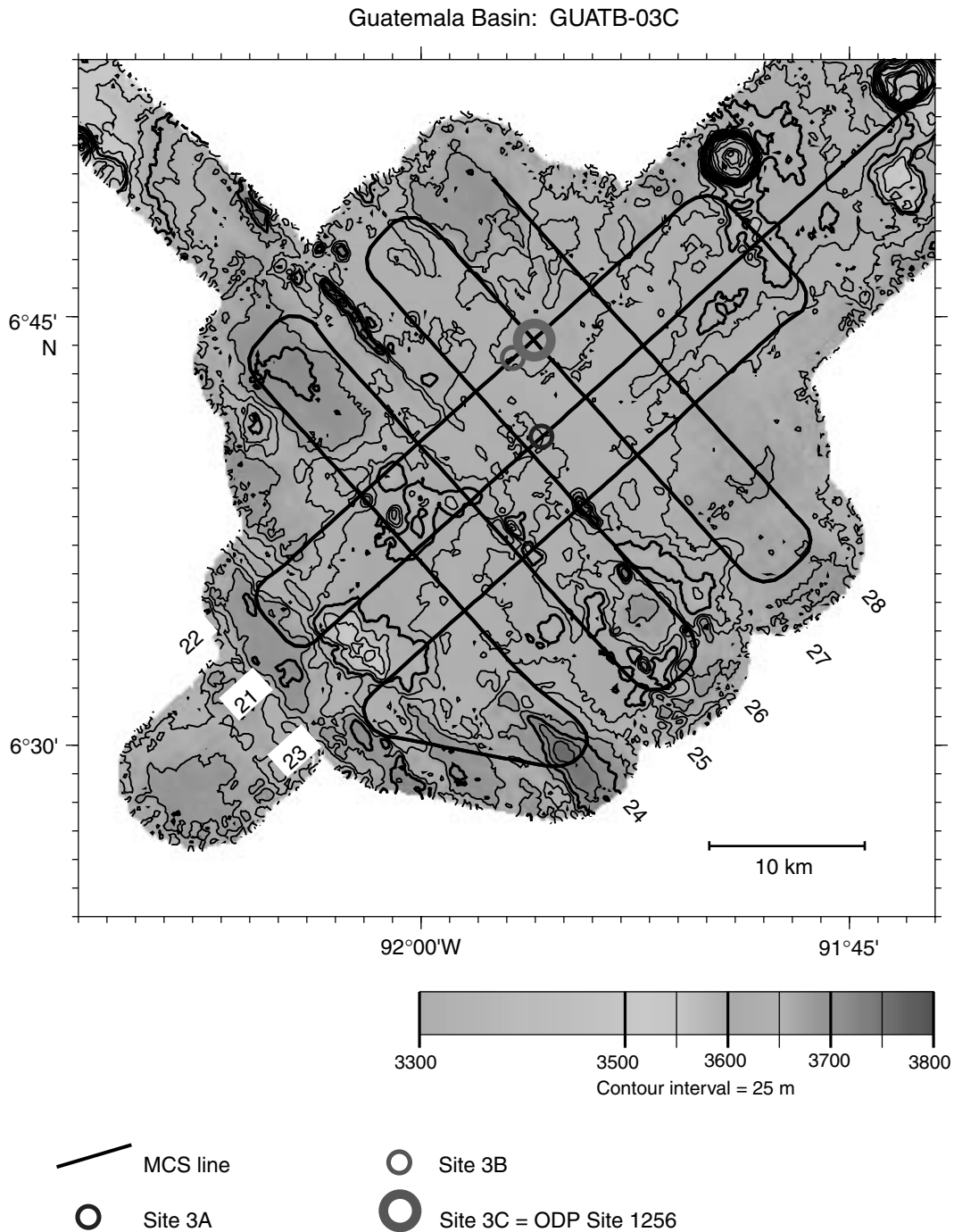


Figure F11. Bathymetry and site survey multichannel seismic (MCS) track map for proposed Site GUATB-02. Abyssal hill relief of ~100 m is more pronounced than for most nearby regions.

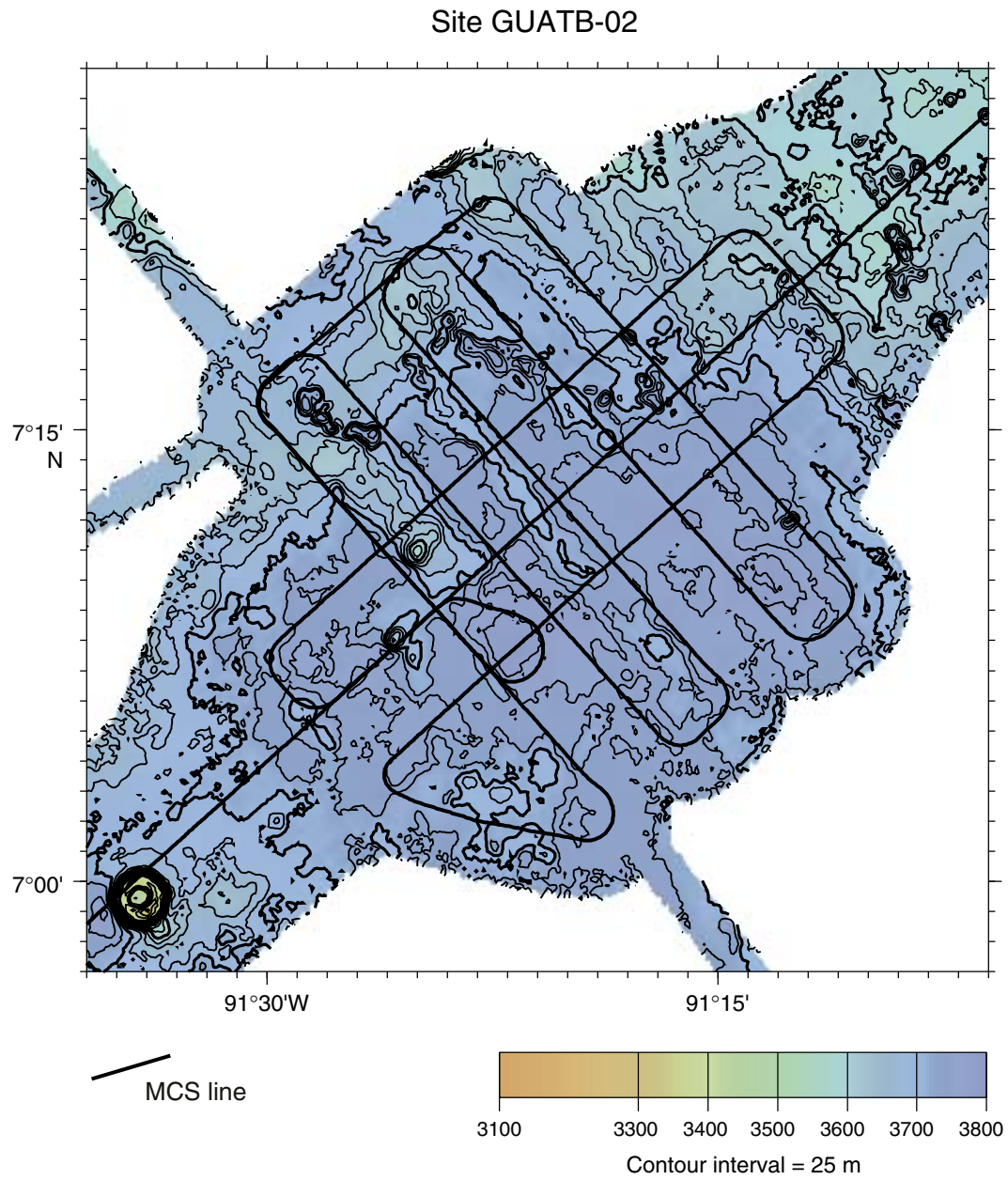


Figure F12. Bathymetry and track maps for proposed alternate Site GUATB-01. Site GUATB-01 has very shallow depths and low relief, excluding seamounts, in contrast to proposed Site ALIJOS (Fig. F13, p. 52), which is slightly deep and has very high relief. MCS = multichannel seismic survey.

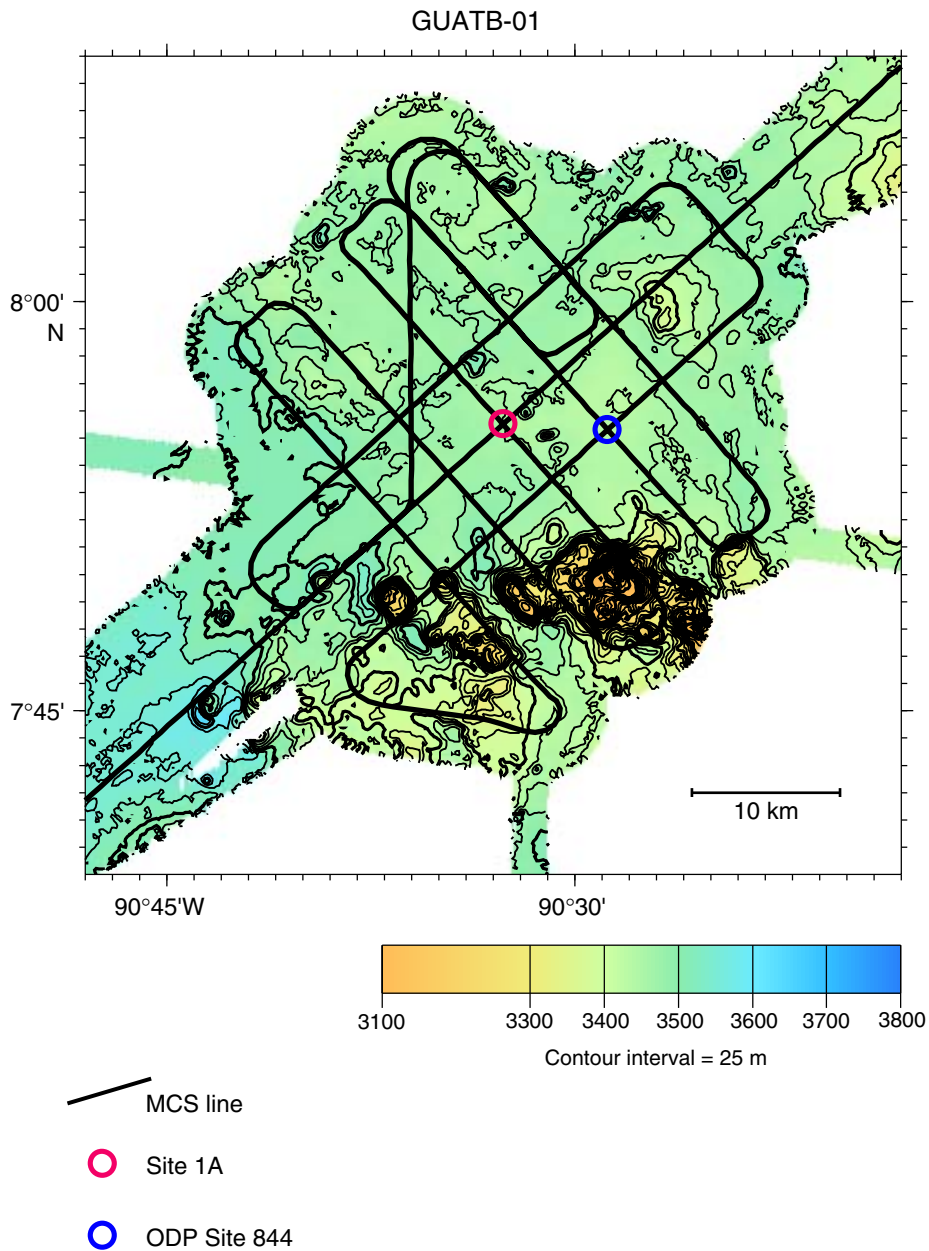


Figure F13. Bathymetry and track maps for proposed Site ALIJOS, a surveyed site that was not drilled.

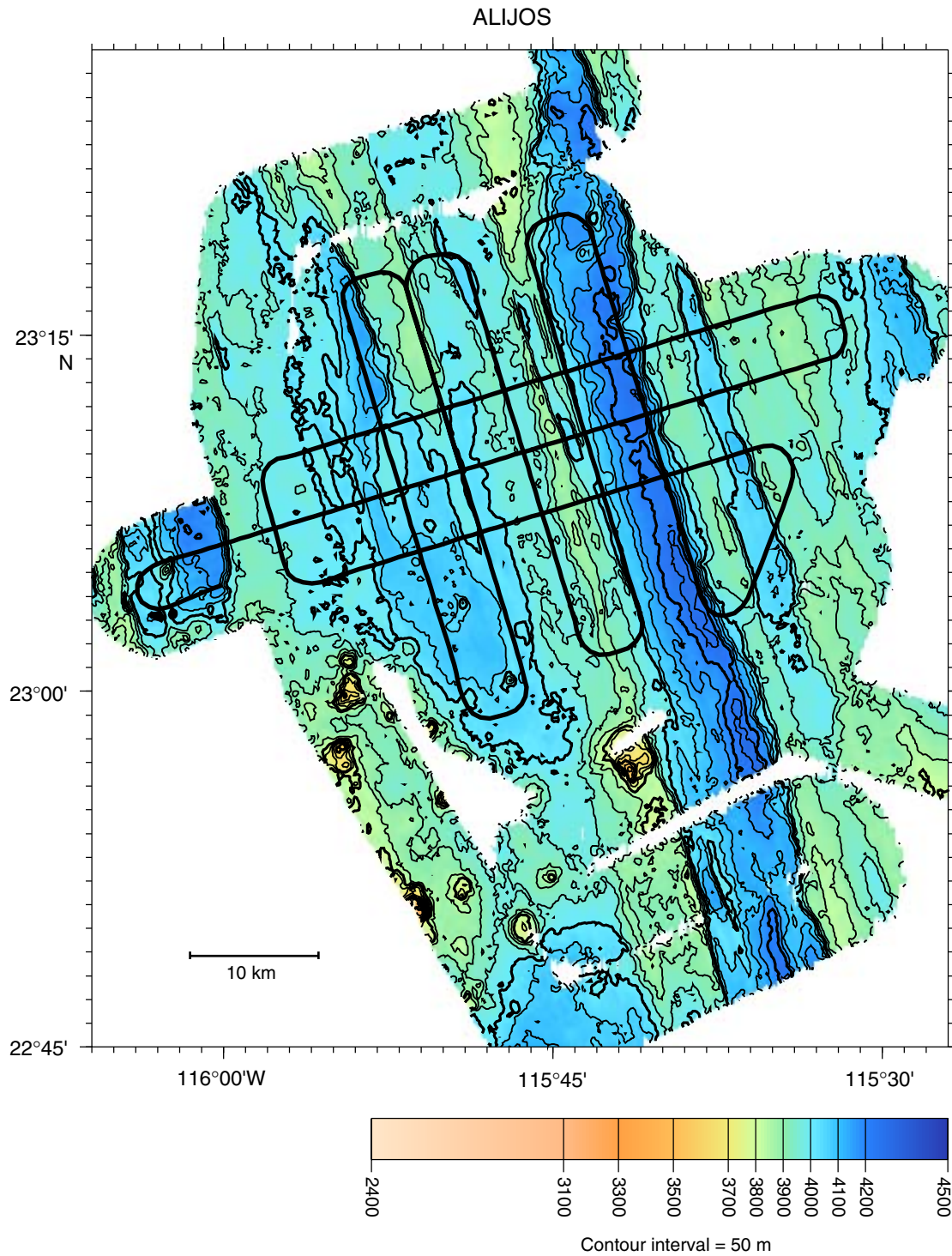


Figure F14. Stacked, migrated section of MCS data from line 22, showing positions of primary proposed drill Site GUATB-03C (Site 1256) and proposed alternate Site GUATB-03B. Crossing positions of lines 24–28 are labeled.

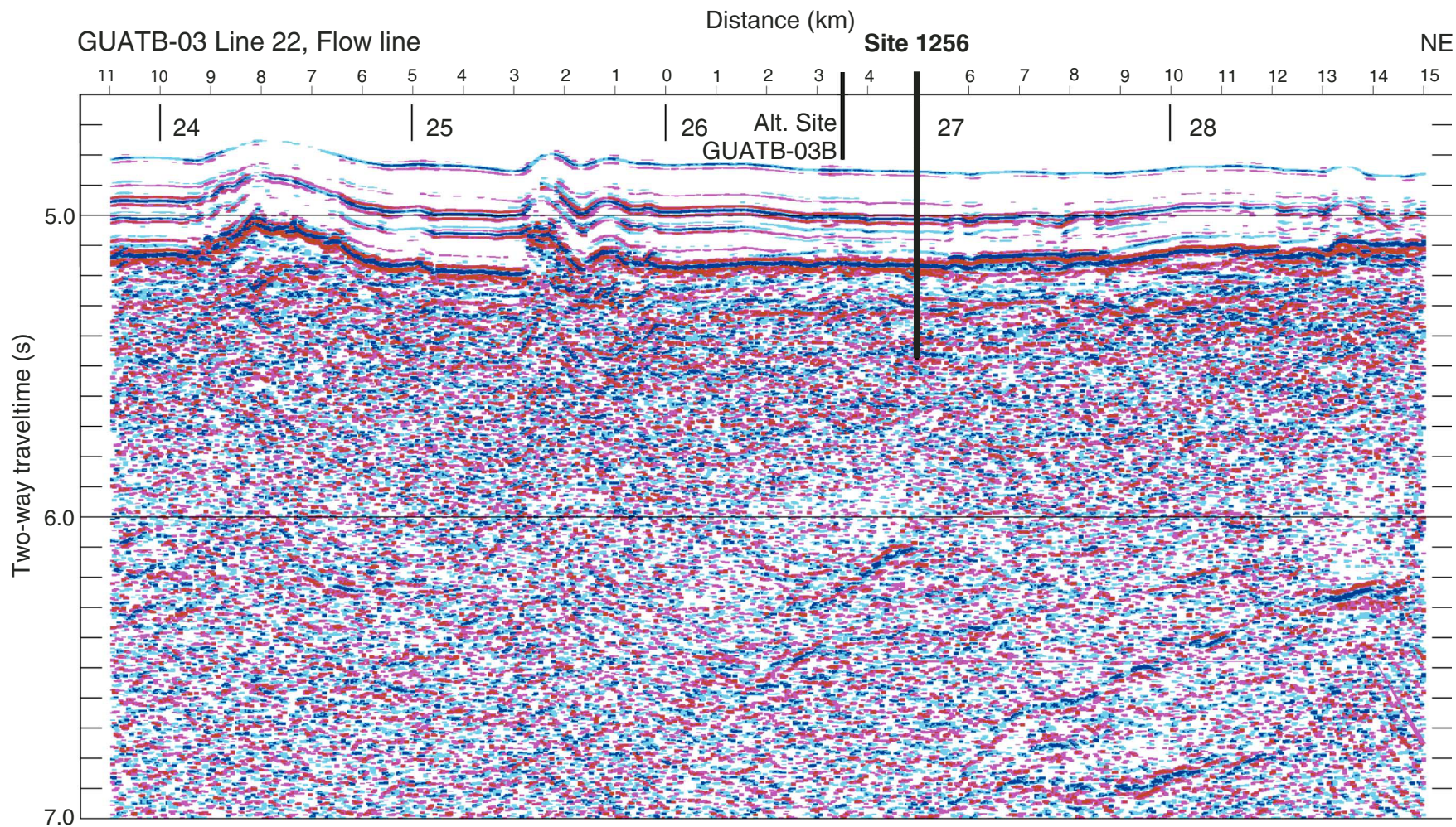


Figure F15. Stacked, migrated section of MCS data from line 27, showing the primary proposed drill Site GUATB-03C and crossing positions of lines 21–23. The bright reflector at 5.5–5.7 s near the line 21 crossing may be a thrust fault, and site selection decisions avoided this feature.

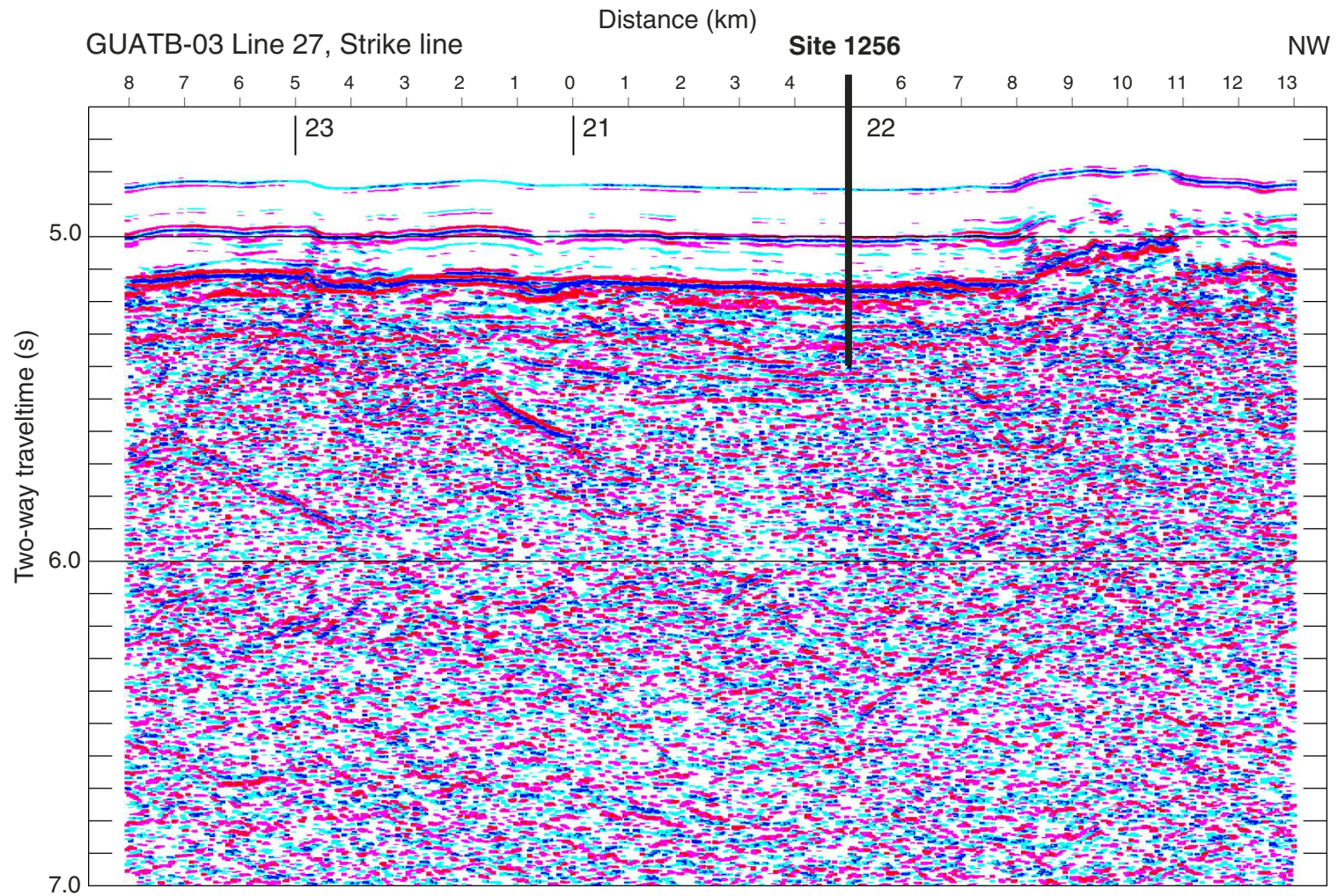


Figure F16. One-dimensional velocity model based on inversion of refraction data. At shallow depths, separate inversions were performed on northeast and southwest data subsets, with slightly faster velocities found to the northeast where abyssal hill topography is very subdued. The Layer 2/3 boundary is present in the depth range 1.2–1.5 km. The velocity model of Detrick et al. (1998) for Site 504, also based on ocean-bottom hydrophone refraction, is shown for comparison. Apparent differences are dominated by differences in the inversion techniques, but the differences at 1.3–1.7 km may be barely above uncertainty.

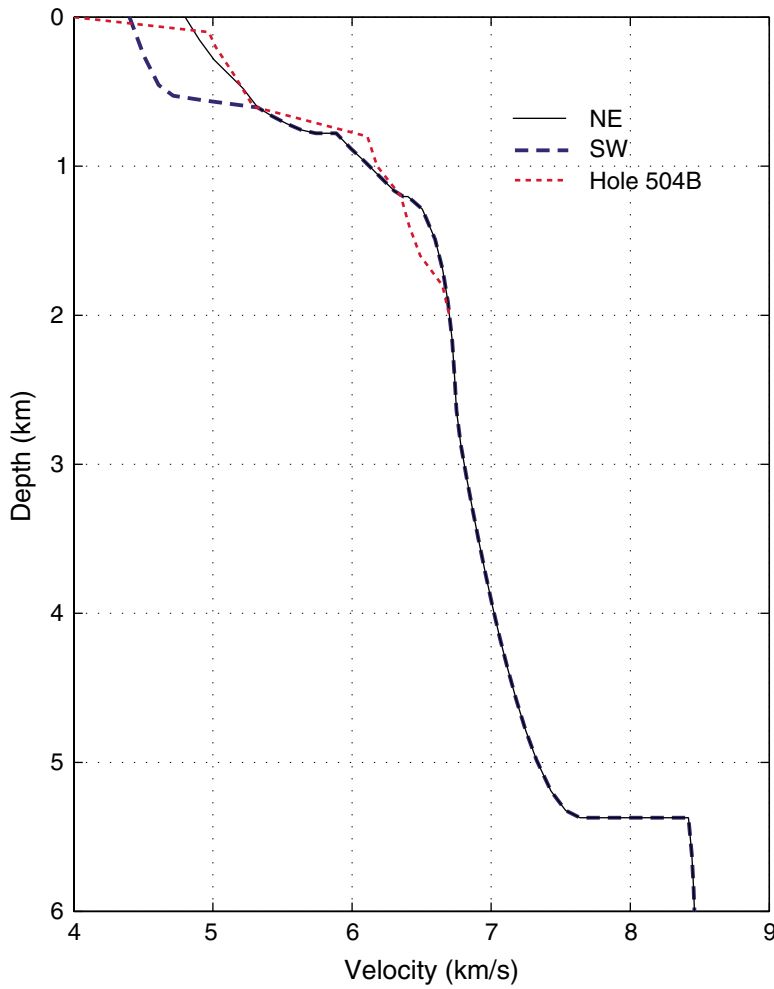


Figure F17. Location map showing positions of the four holes drilled at Site 1256.

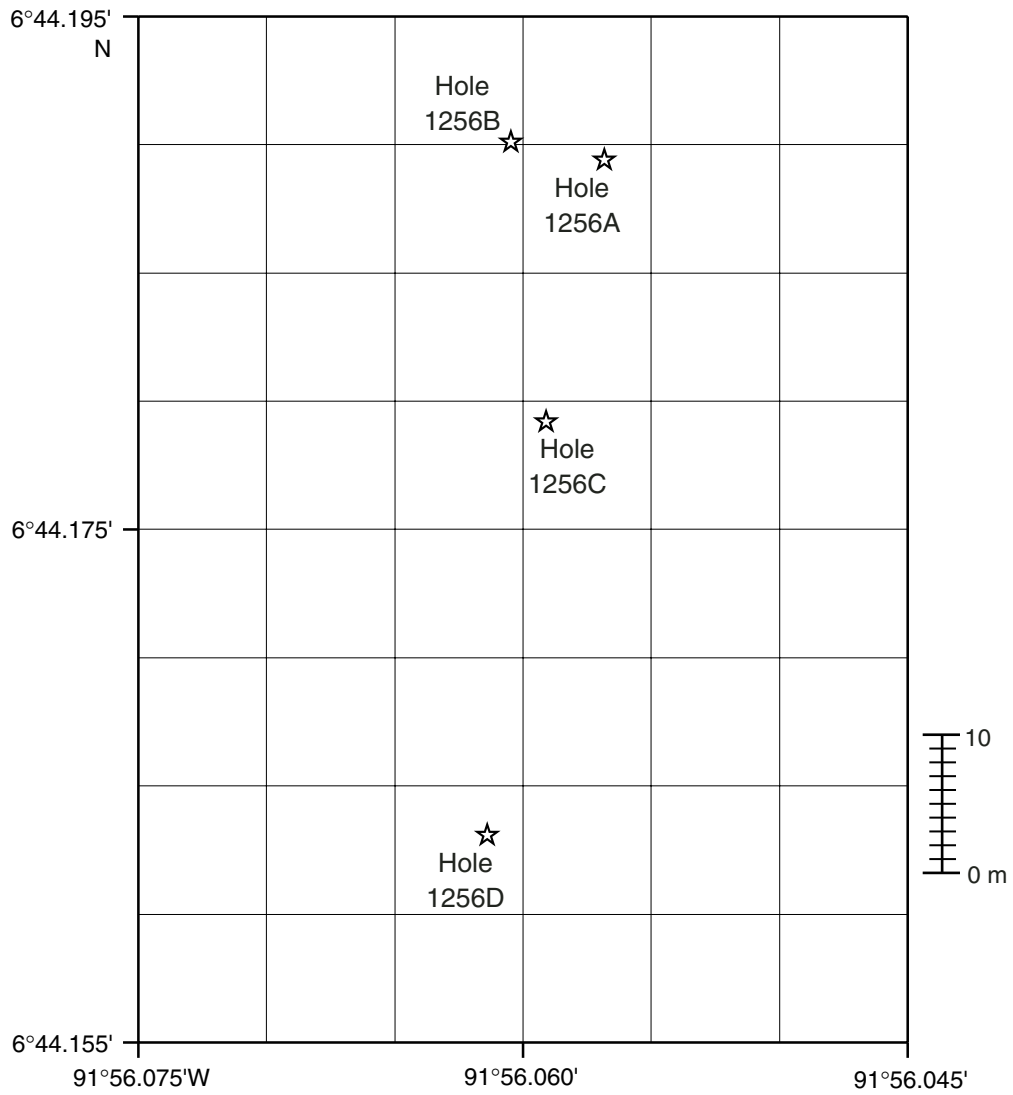


Figure F18. Schematic of the reentry cone and casing installed in Hole 1256D. TOC = top of casing, ID = inner diameter, TD = total depth.

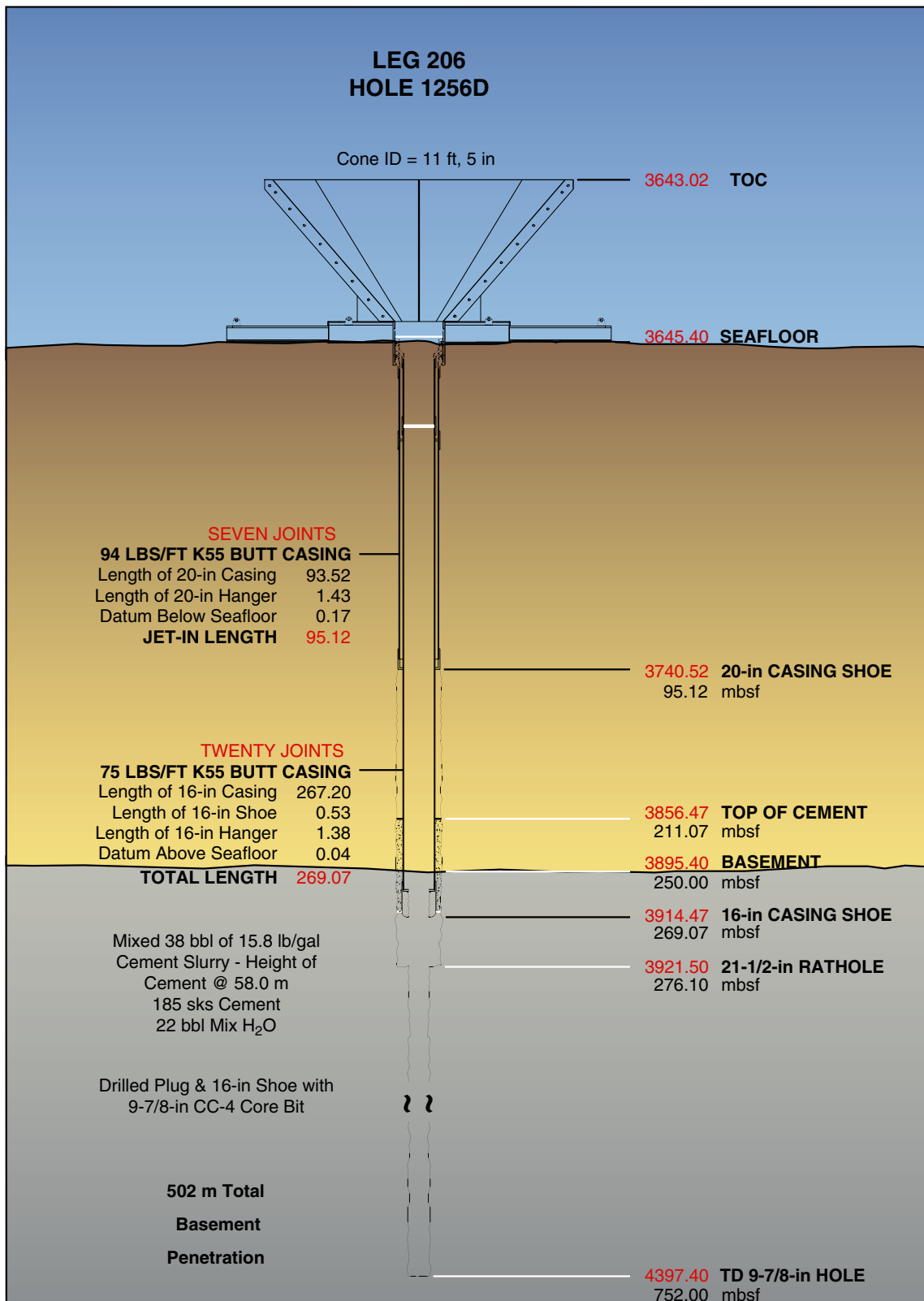


Figure F19. Simplified lithostratigraphic column for Site 1256. The lithology column gives the approximate relative abundance of major components (>10%) contributing to the rock name, following the conventions used for the AppCore core description sheets. (Continued on next page.)

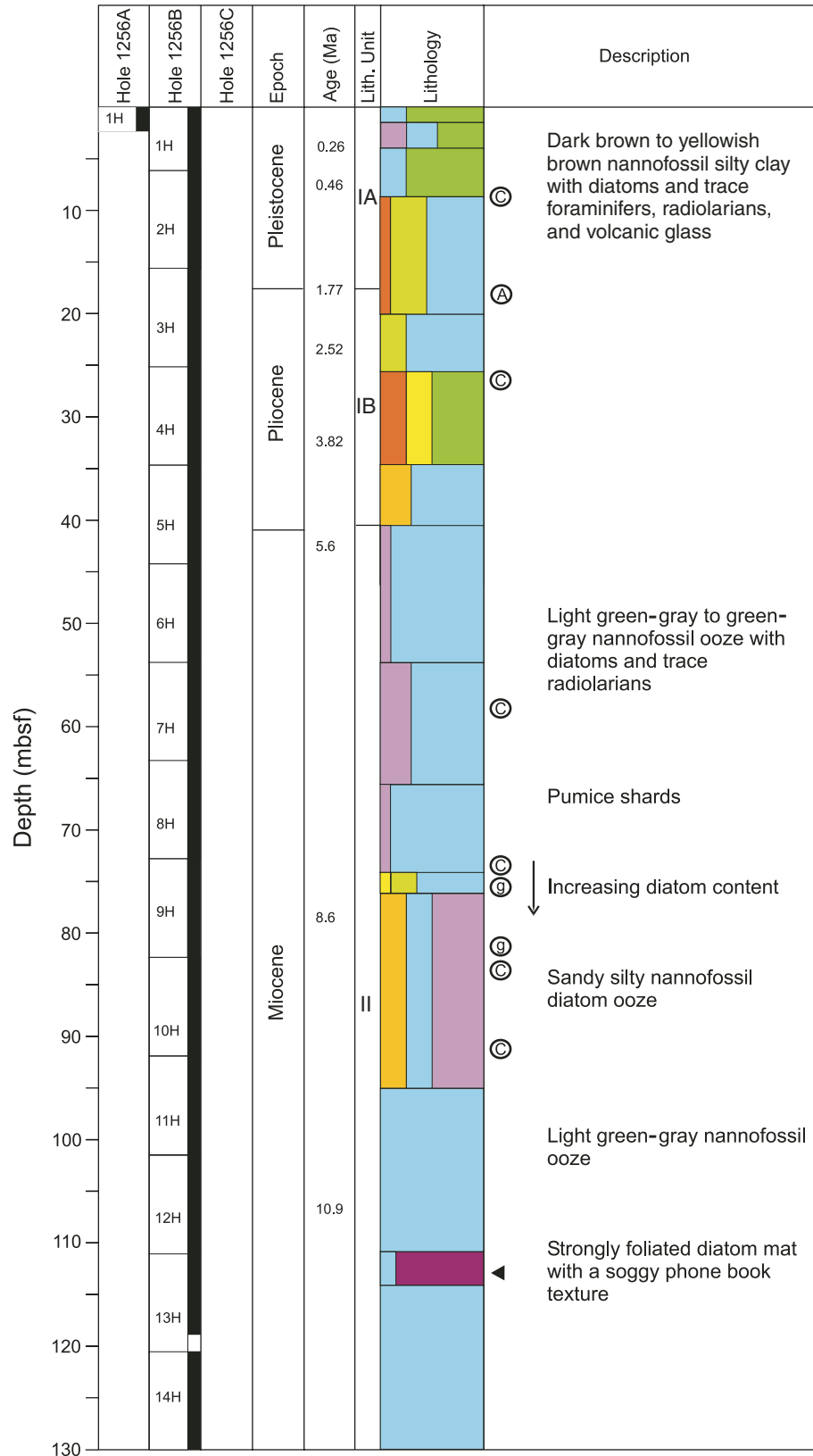


Figure F19 (continued).

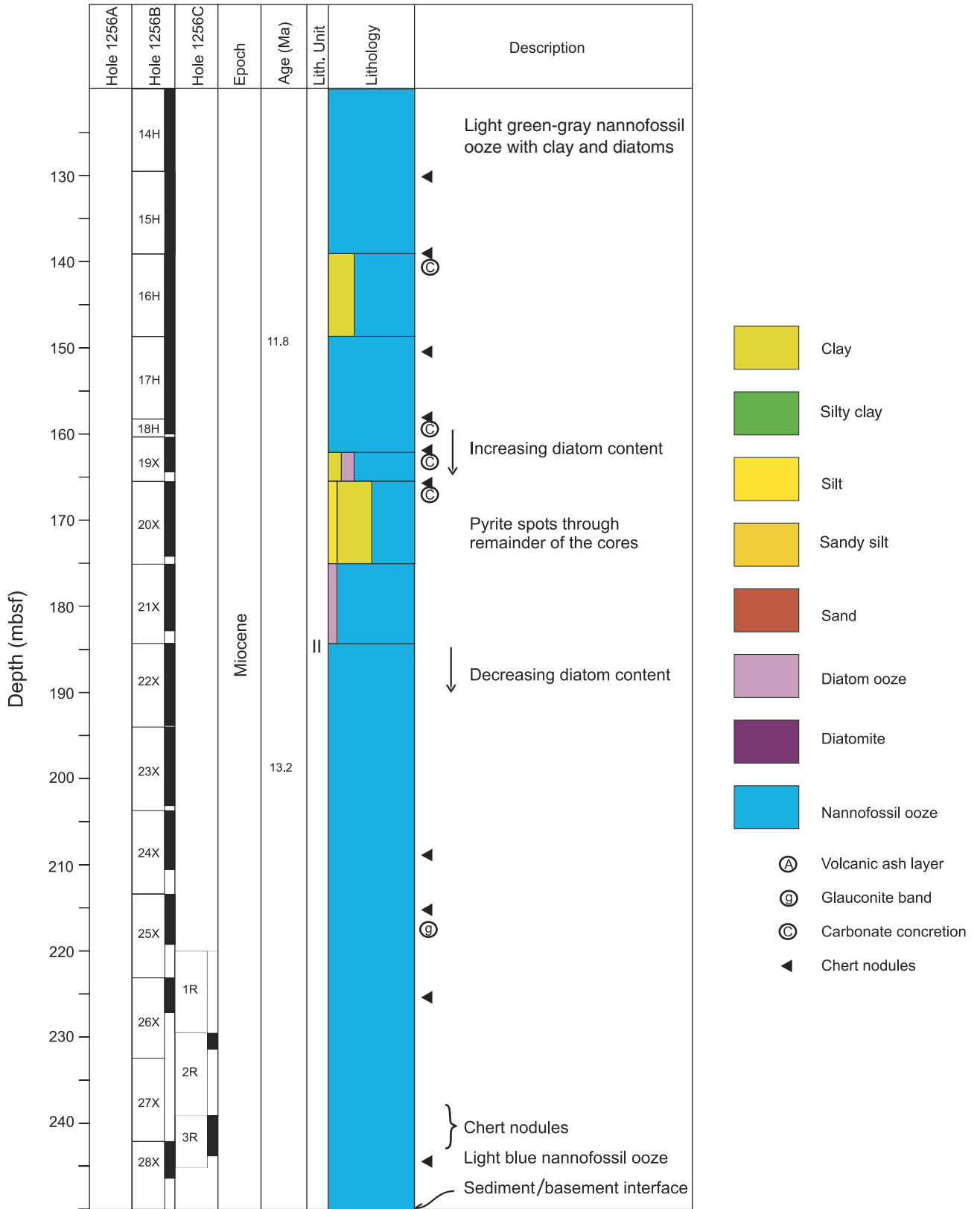


Figure F20. Magnetostratigraphy and inclination and declination of the cored interval as estimated from stable endpoints from split-core sections. Also shown is the intensity of magnetization following 30-mT alternating-field demagnetization. The brackets indicate intervals where the interpretation is uncertain. Orange box = an interval where the magnetic polarity could not be determined.

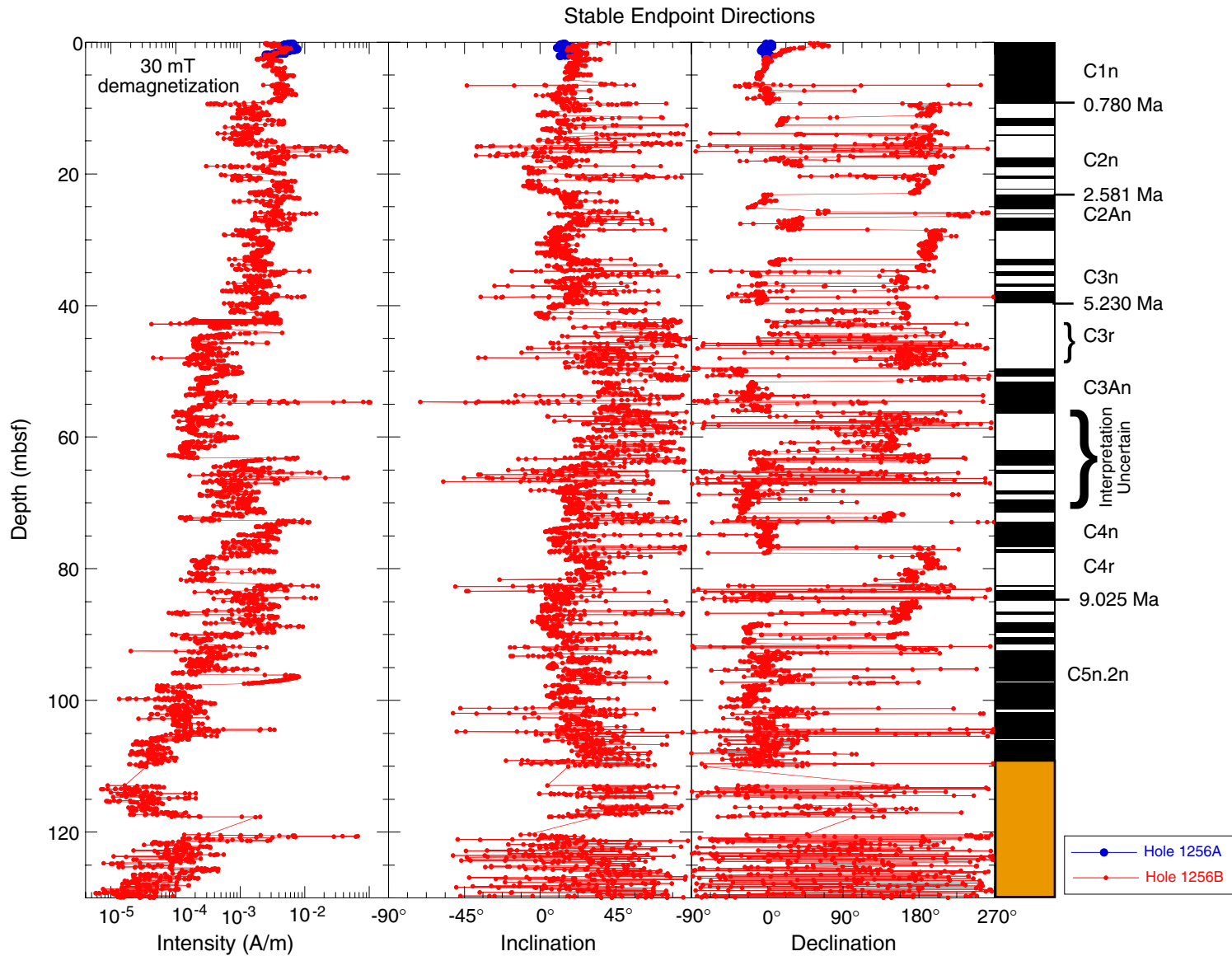


Figure F21. Magnetostratigraphy and declination of the cored interval as estimated from principal component analysis (PCA) and stable endpoints (SEP) from split-core sections and discrete samples. (Continued on next two pages.)

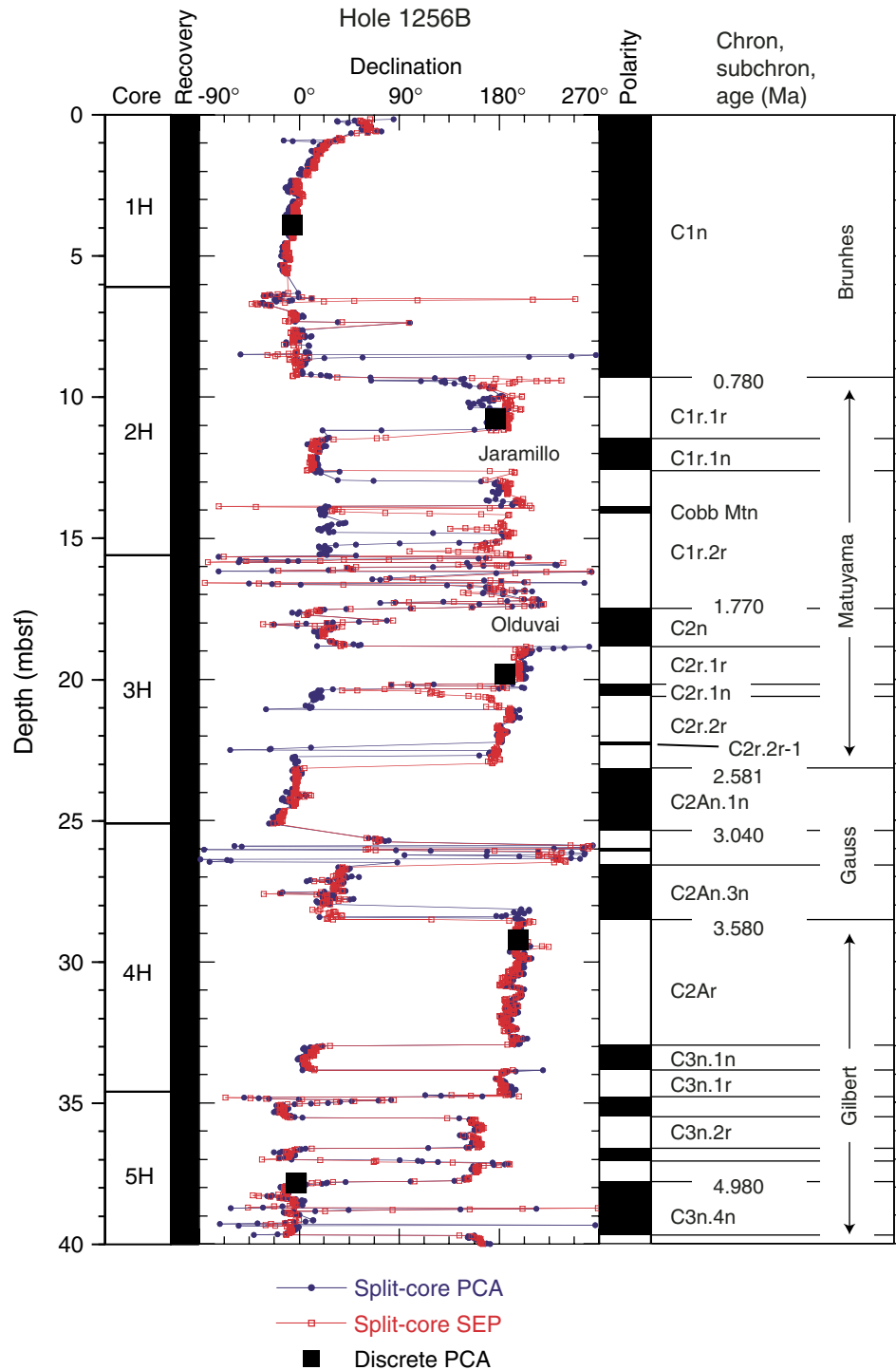


Figure F21 (continued).

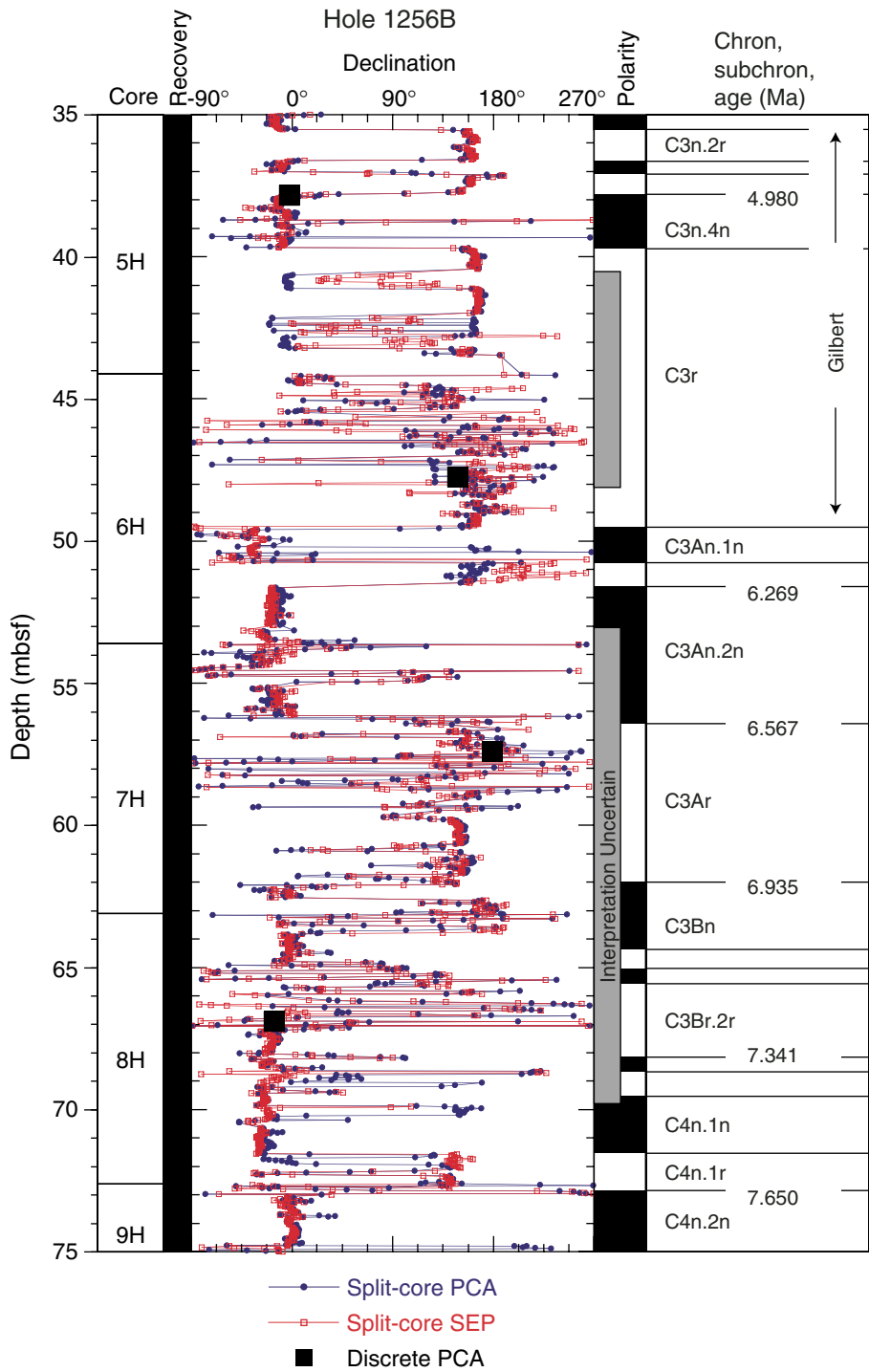


Figure F21 (continued).

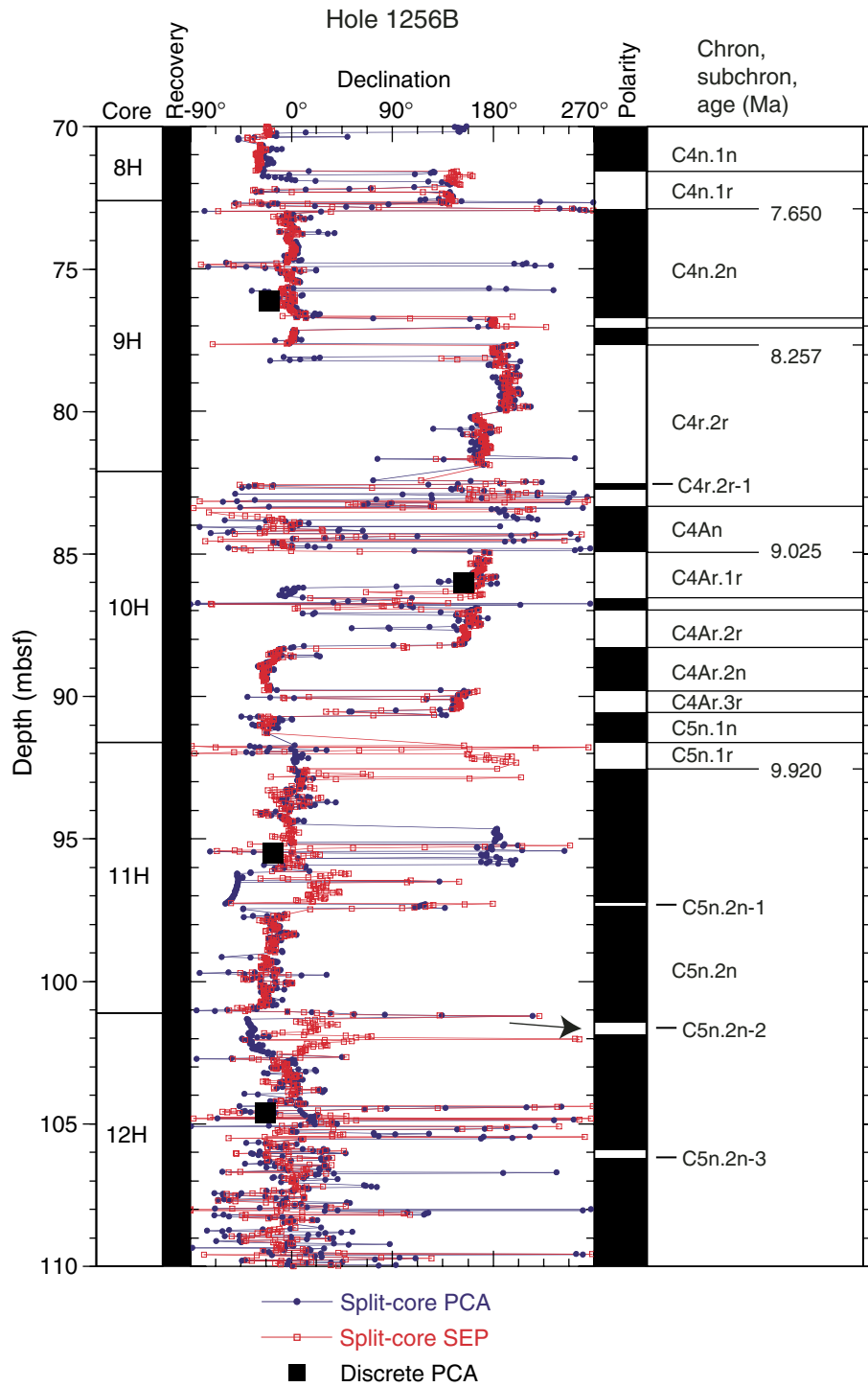


Figure F22. Age-depth plot of Neogene calcareous nannofossil datums (diamonds) and geomagnetic reversals (squares) from Hole 1256B. Nannofossil datum ages and depths are given in Table T7, p. 112 (see also "Biostratigraphy," p. 23), and geomagnetic reversal ages and depths are given in Table T9, p. 114 (see also "Paleomagnetism," p. 33). FO = first occurrence, LO = last occurrence.

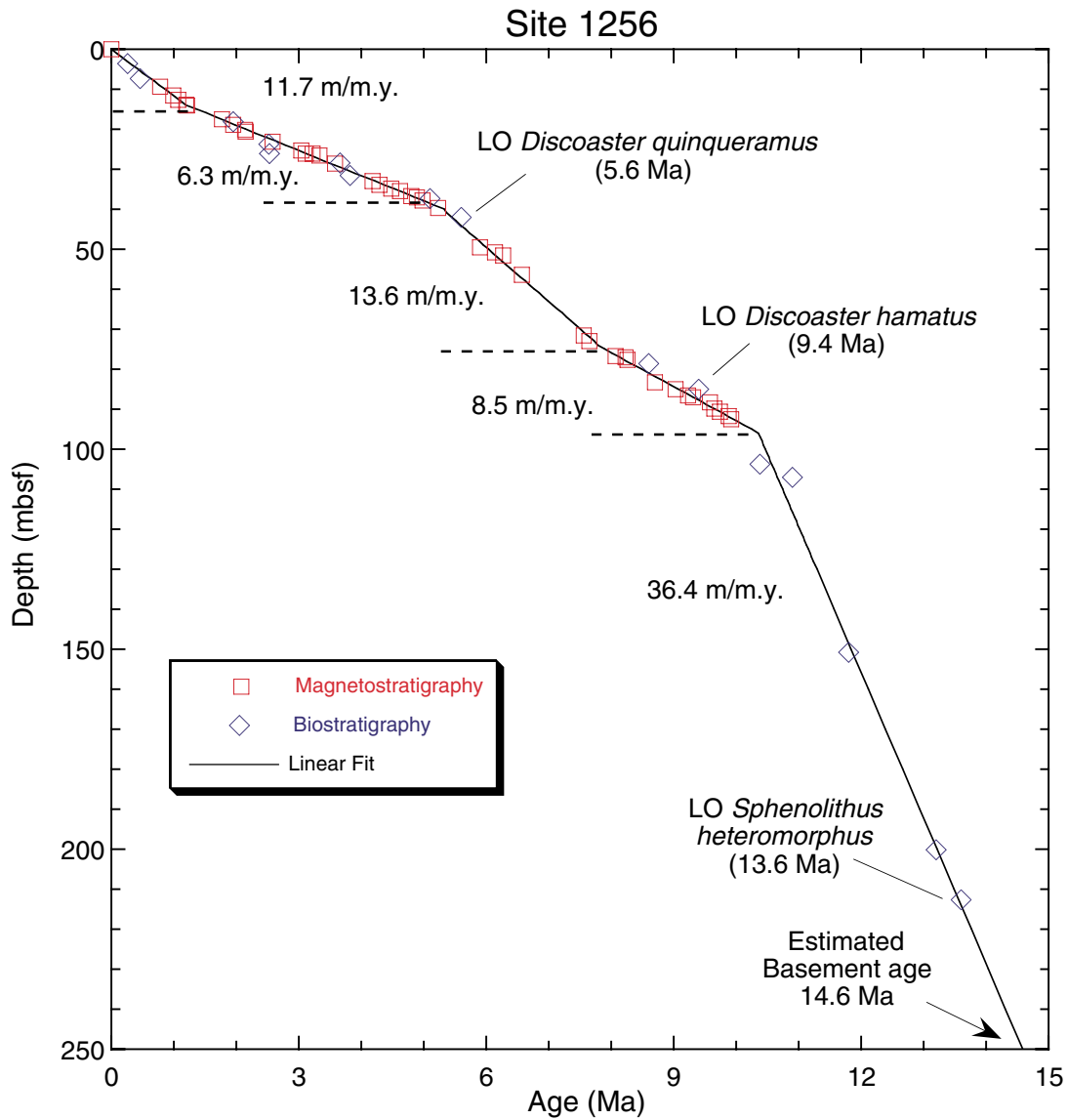


Figure F23. Sedimentation rates as constrained by the magnetostratigraphy, biostratigraphy, and a linear sedimentation rate model. The linear rates are shown extrapolated to basement.

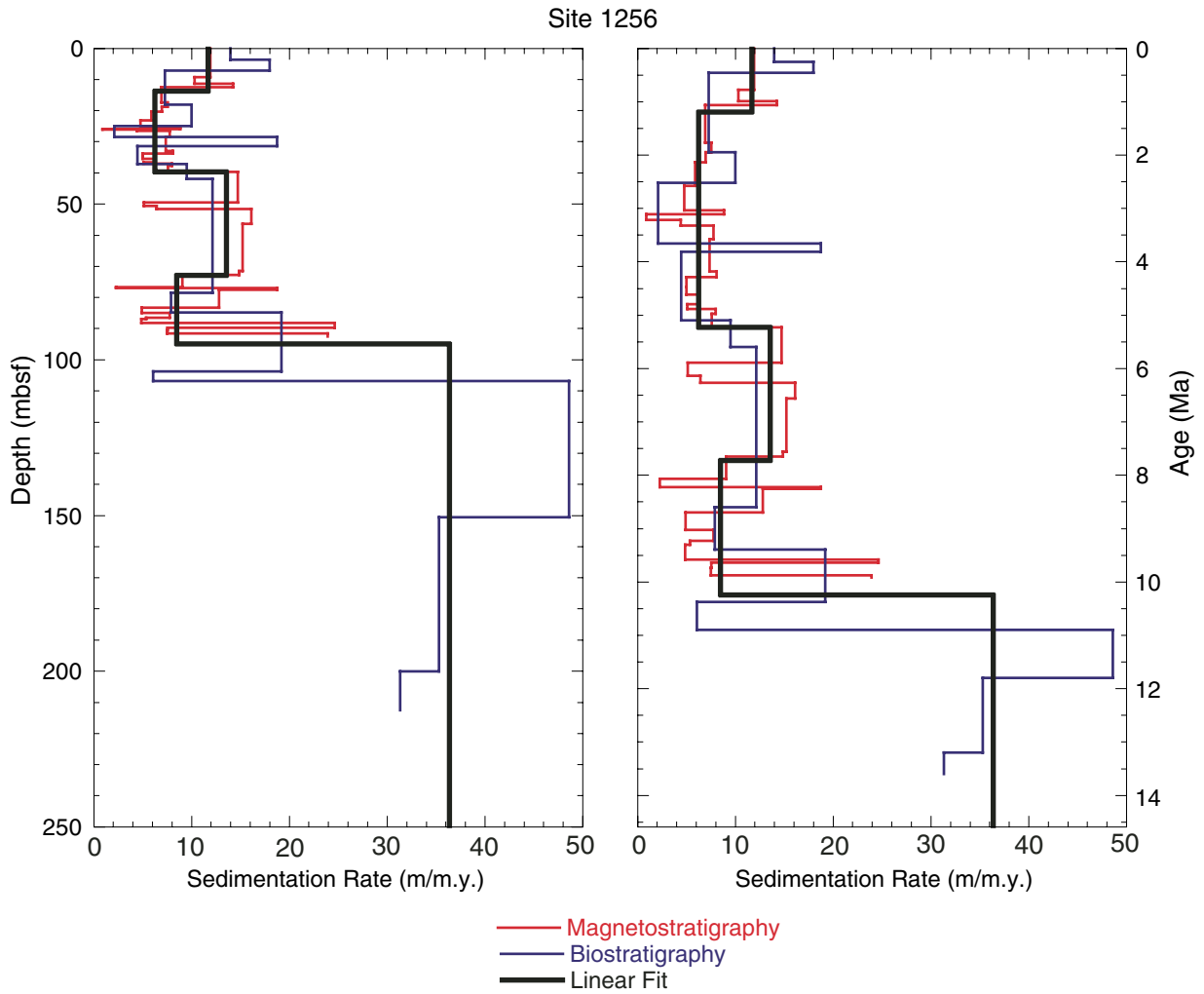


Figure F24. Depth profiles of calcium carbonate, organic carbon, terrigenous matter, and biogenic silica in sediments.

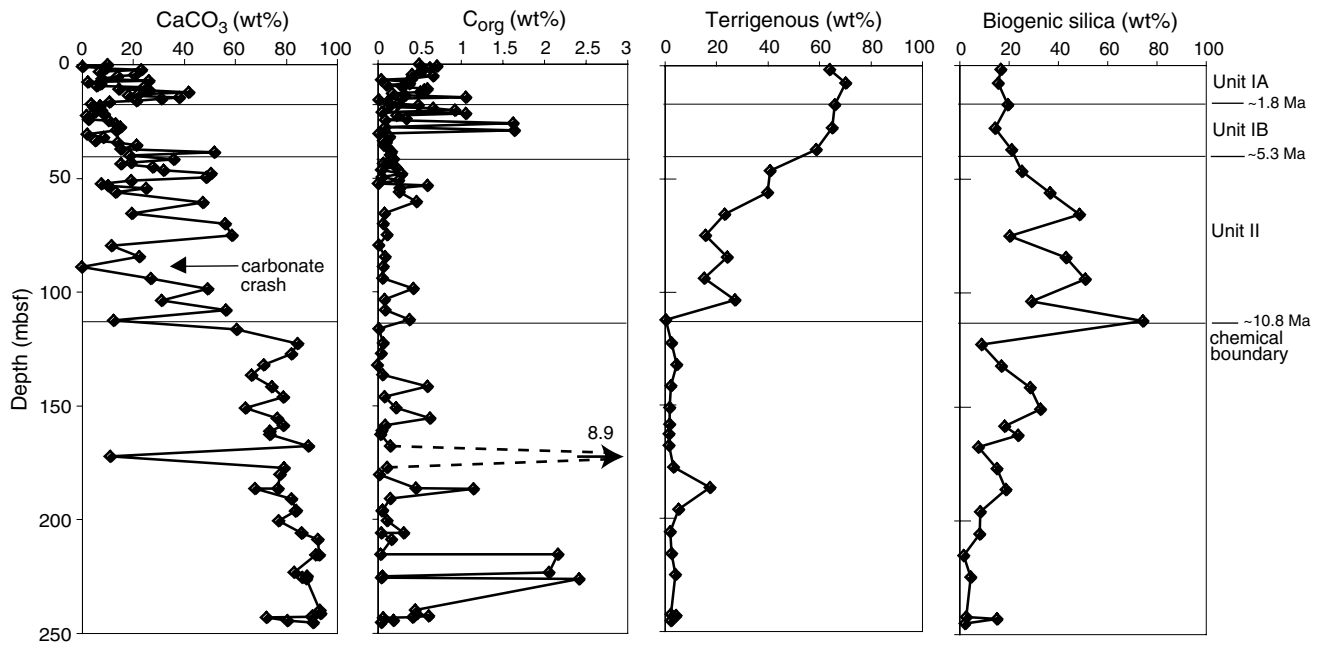


Figure F25. Depth and age profile of Ba/Ti ratios, a chemical proxy for productivity, in sediments.

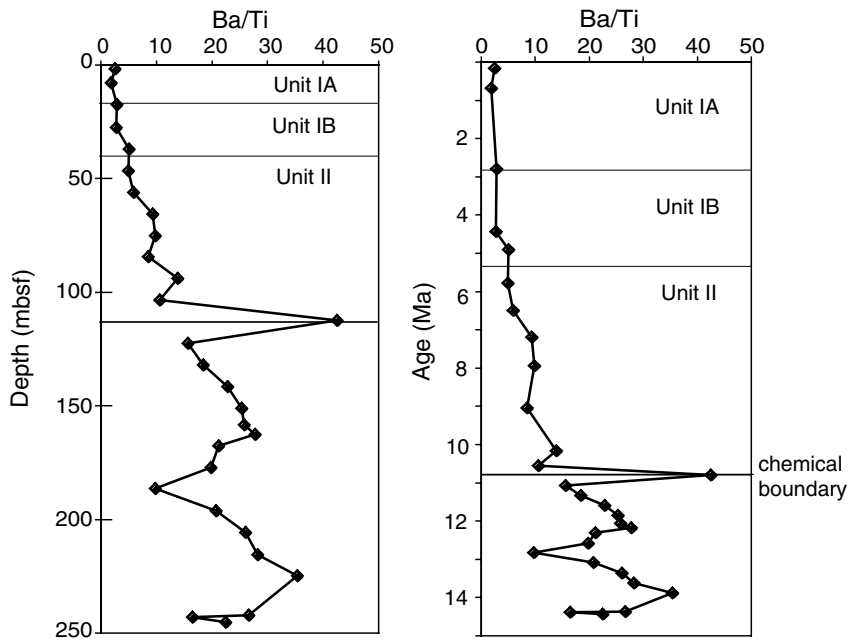


Figure F26. Depth profiles of Mg/Ca, Sr/Ca, K/Mg and K/Ca, and Li/Mg and Li/Ca in interstitial waters from Hole 1256B. JDF = values observed at Juan de Fuca Ridge flank, representing basement fluid (long dashed lines). SW = seawater values (short dashed lines). Ca/Mg and K/Ca display diffusion between seawater and basement fluids. Sr/Ca values are larger than what is observed at Juan de Fuca Ridge flank, suggesting a strong influence of recrystallization taking place. Li/Mg and Li/Ca ratios are similar to the Ca/Mg profile.

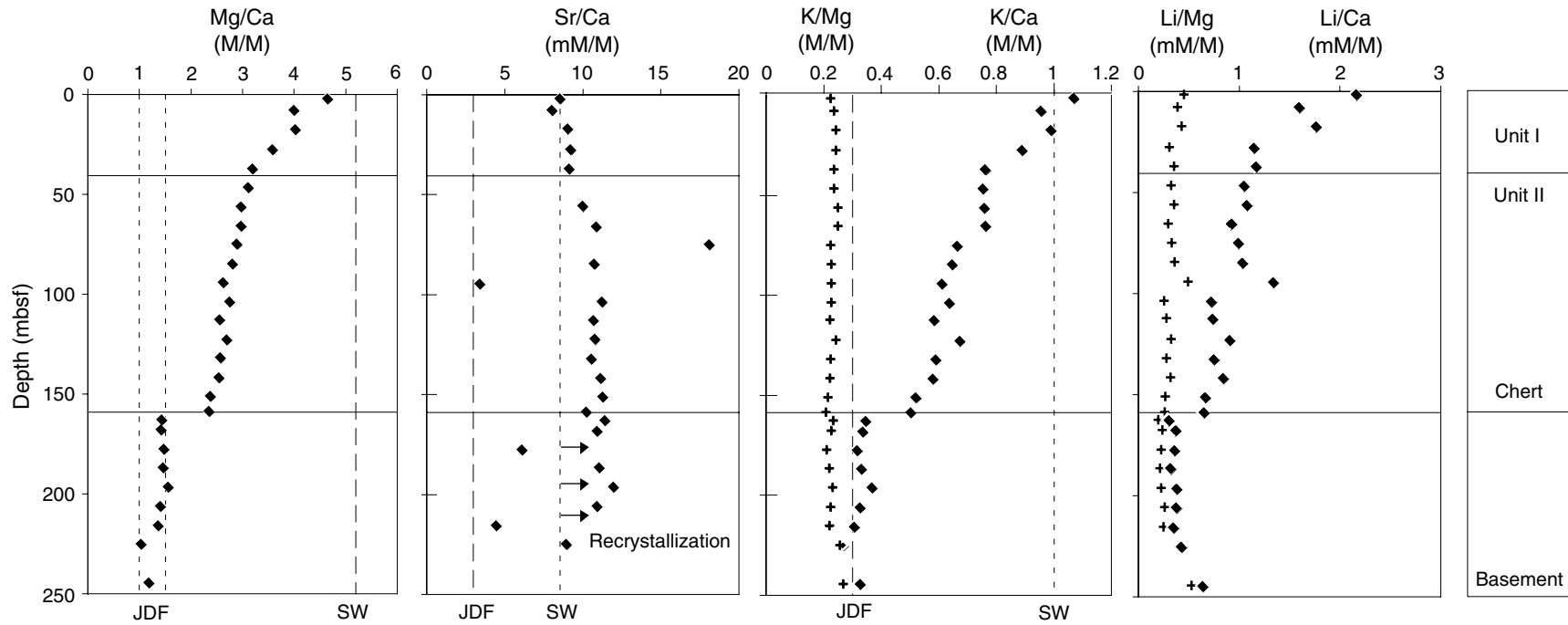


Figure F27. Whole-core gamma ray attenuation (GRA) bulk density, discrete sample bulk density, and grain density, porosity, and split-core *P*-wave velocity (PWS3; V_p) for the sediments of Site 1256. Open symbols = anomalous values. Also shown is the simplified lithostratigraphy: blue = nannofossil ooze; orange and yellow = clay, silt, or silty clay; shades of purple = diatom-rich intervals. Dashed lines = the boundary between lithologic Units I and II at 40.6 mbsf, the top of the diatom mat at 111 mbsf, and a physical property boundary at ~205 mbsf. The GRA density data have been smoothed by averaging over a 41-point (102.5 cm long) window.

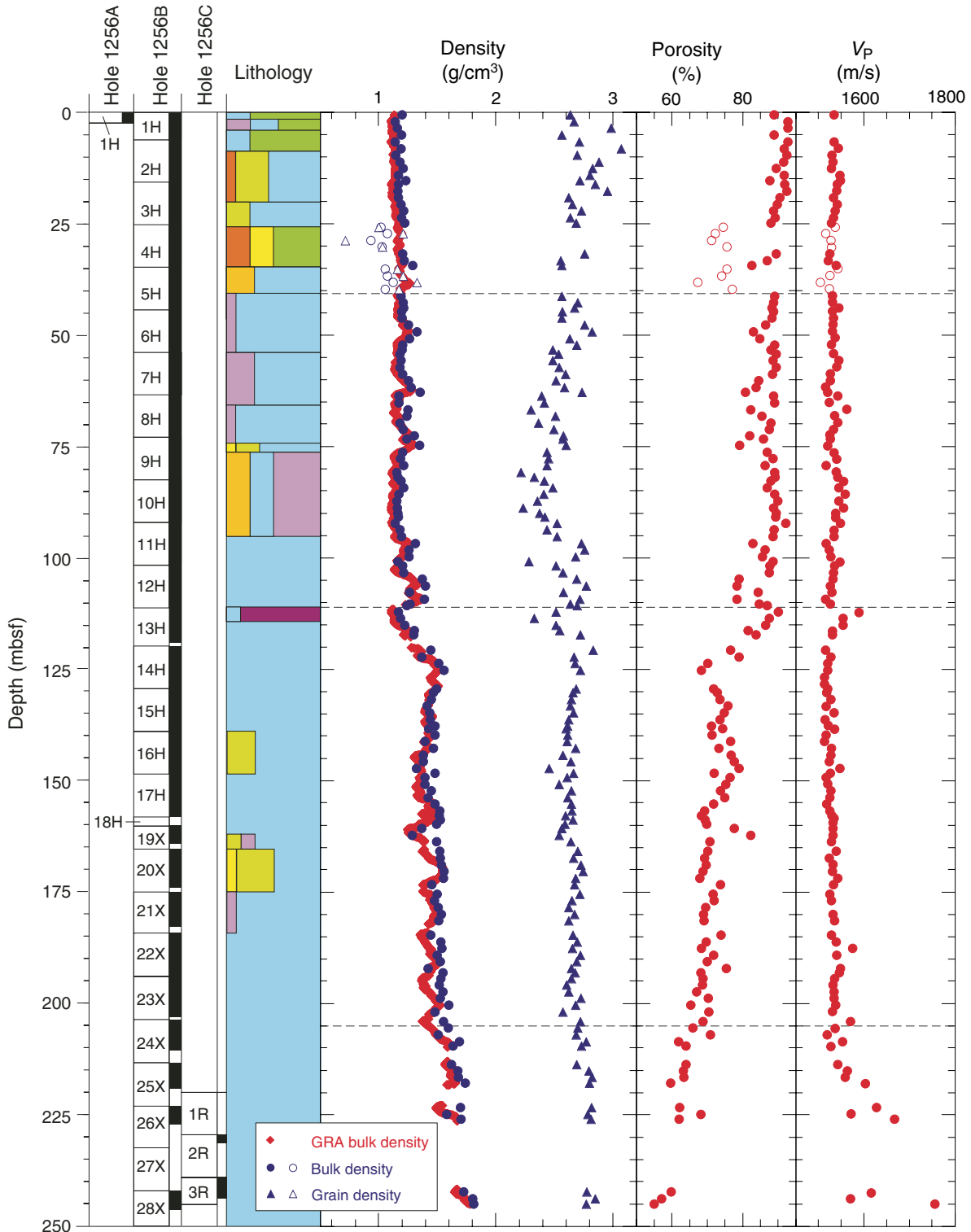


Figure F28. Downhole variations in temperature, thermal conductivity, and heat flow for Hole 1256B.

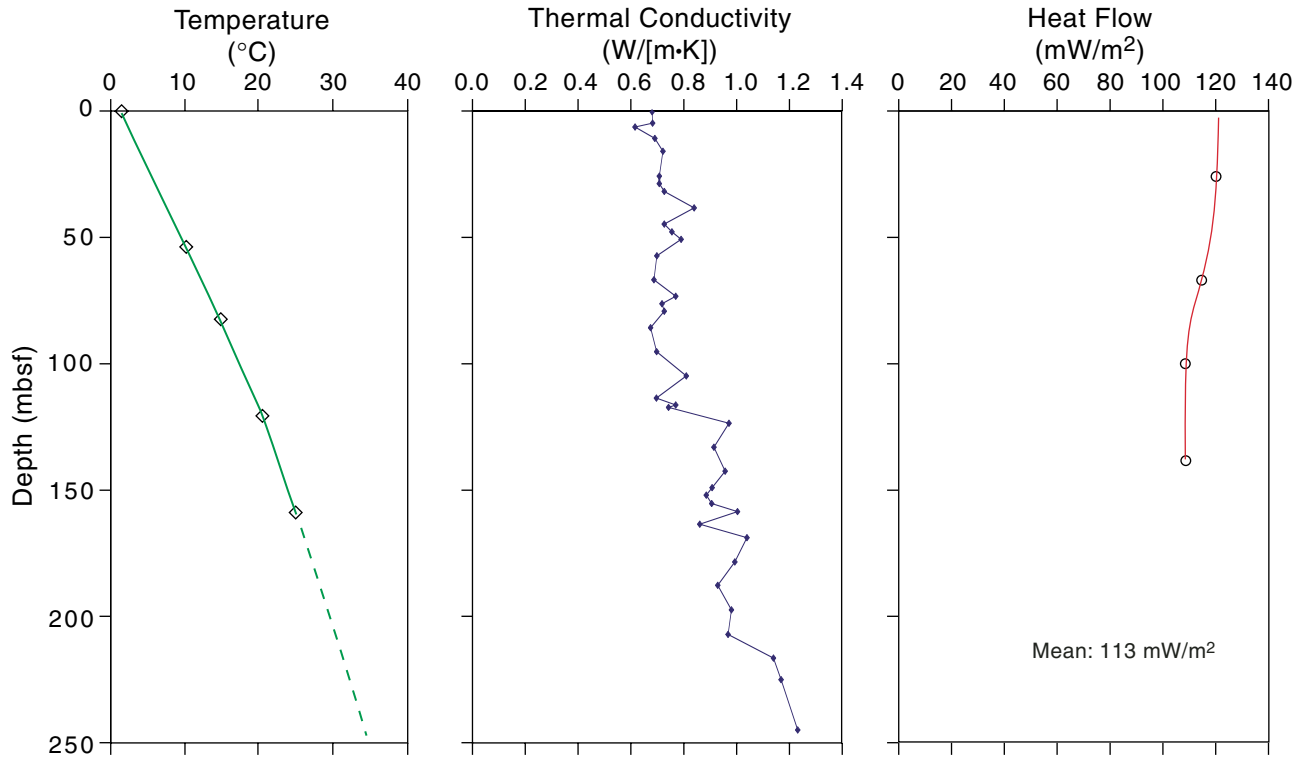


Figure F29. Summary of basement stratigraphy at Site 1256. Phenocryst percentages are based on thin section descriptions. cx = cryptocrystalline, μ x = microcrystalline, fg = fine grained. ol = olivine, pl = plagioclase, cpx = clinopyroxene. A. Hole 1256C. (Continued on next page.)

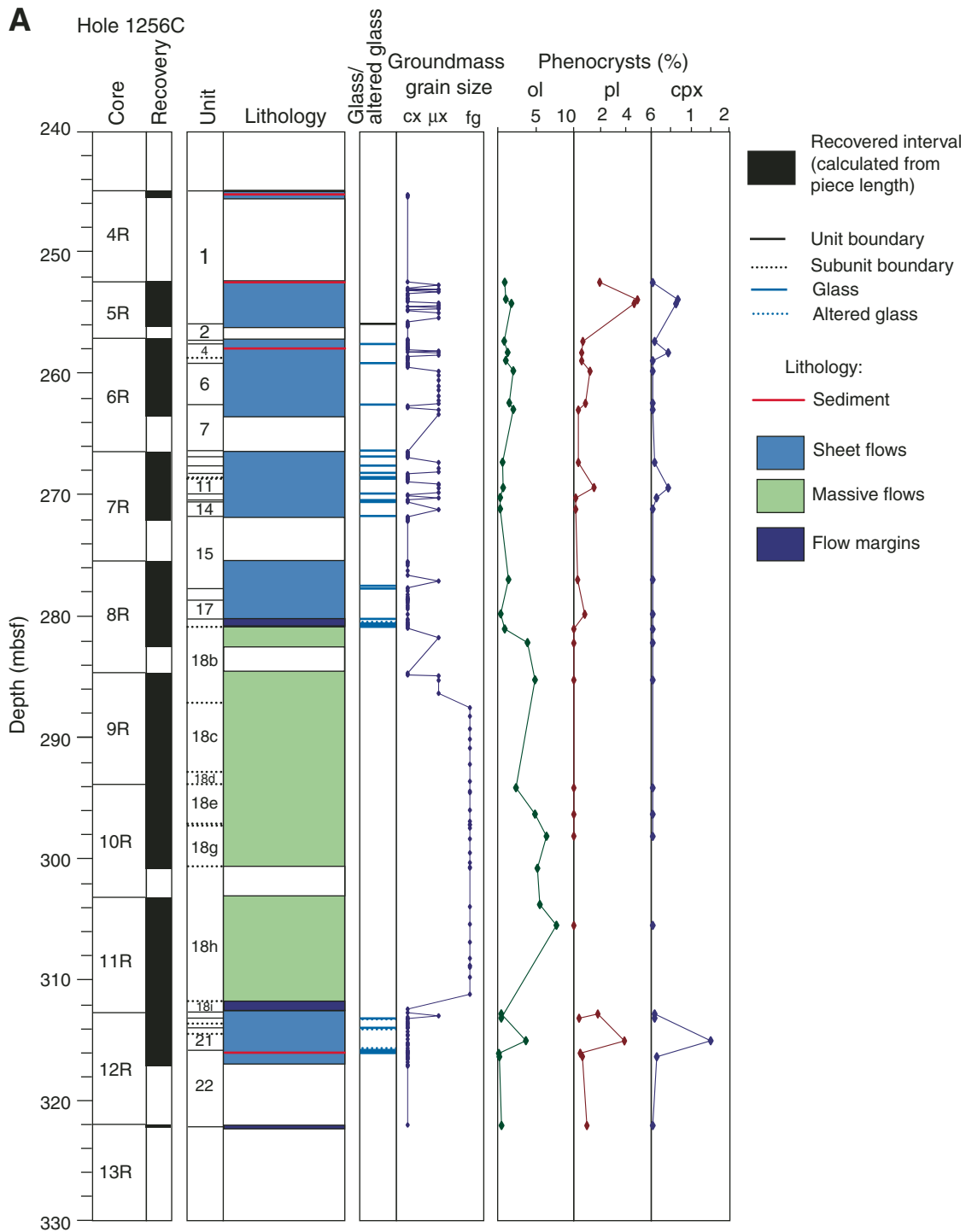


Figure F29 (continued). B. Hole 1256D.

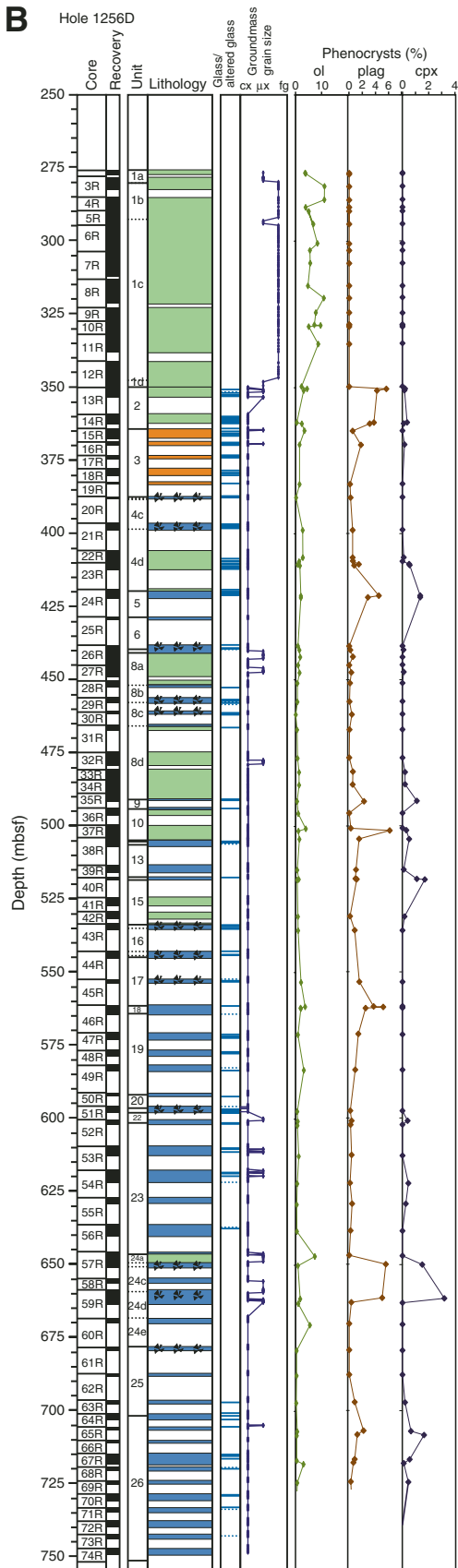


Figure F30. Close-up photograph of typical aphyric cryptocrystalline to microcrystalline texture of sheet flow interior (top) with decreasing grain size toward the chilled margin at the base of the piece in basement Unit 1256C-6 (interval 206-1256C-6R-5, 13–35 cm).



Figure F31. Close-up photograph of folded recrystallized material at base of the ponded flow in basement Subunit 1256C-18i (interval 206-1256C-11R-7, 21–42 cm).

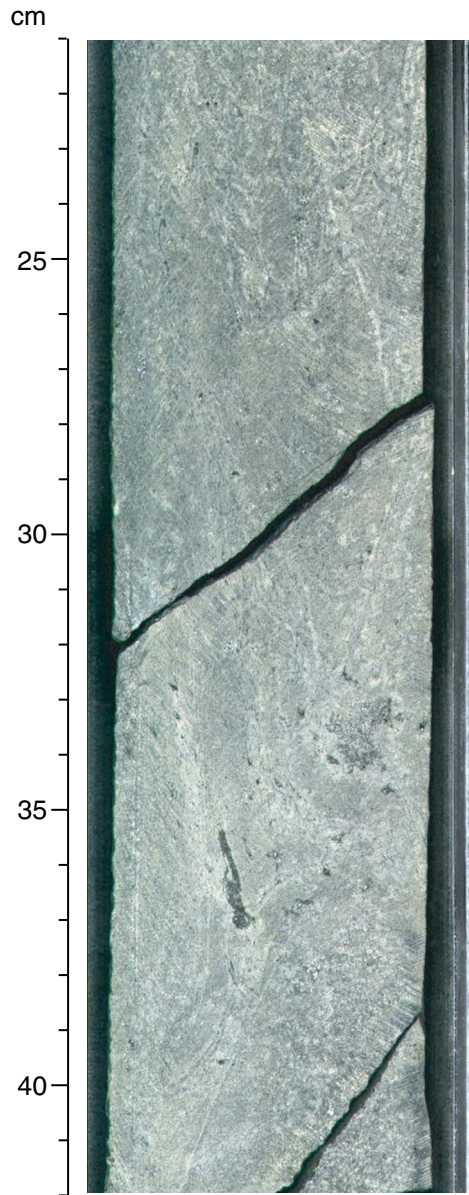


Figure F32. Close-up photograph of typical texture of thin sheet flows. Glassy margin of thin sheet flow in basement Unit 1256D-2 (interval 206-1256D-13R-3, 25–33 cm). Note the horizontal planar shape to glassy margin and parallel vesicle horizon just below the margin.



Figure F33. Close-up photograph of pieces of hyaloclastite consisting of rounded glassy blocks with chilled margins and angular clasts of glass in basement Subunit 1256D-21 (interval 206-1256D-51R-1, 106–150 cm).

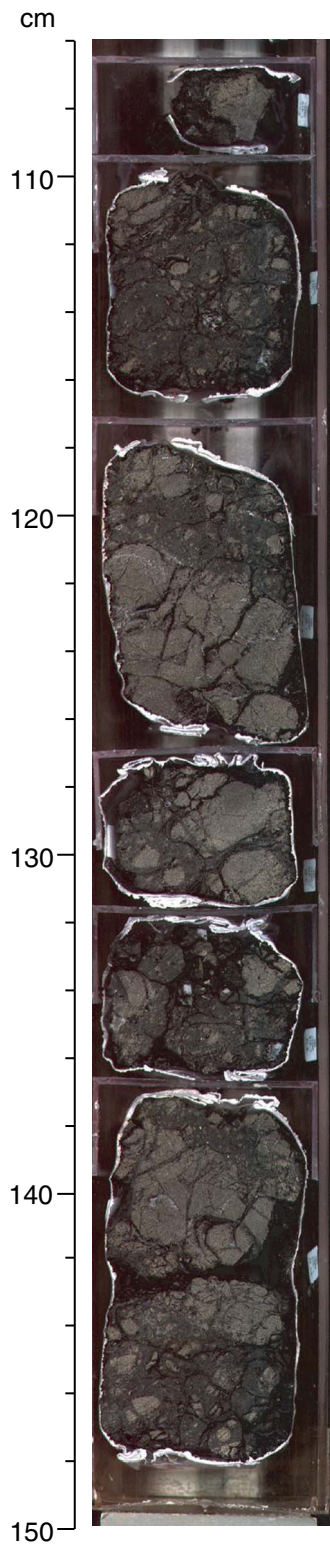


Figure F34. Close-up photograph of volcanoclastic rock composed of angular fragments of cryptocrystalline basalt embedded in a matrix of altered glass in basement Unit 1256D-4a (interval 206-1256D-20R-1, 31–50 cm).

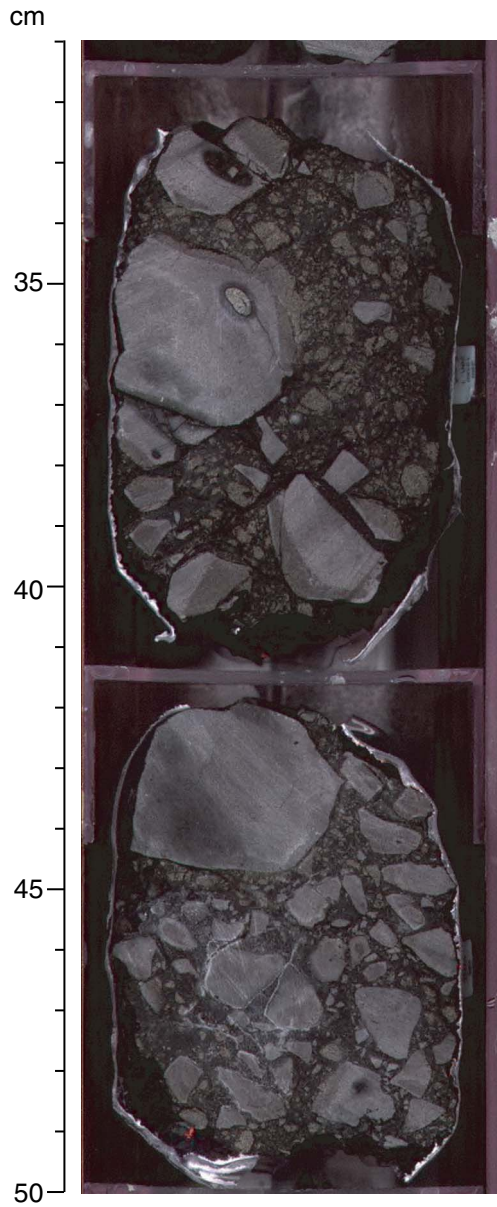


Figure F35. Modal abundance of phenocrysts in basalt from Holes 1256C, 1256D, and all of Site 1256. Lava flows and dikes from Hole 504B and the Mid-Atlantic Ridge (MAR) are plotted for comparison.

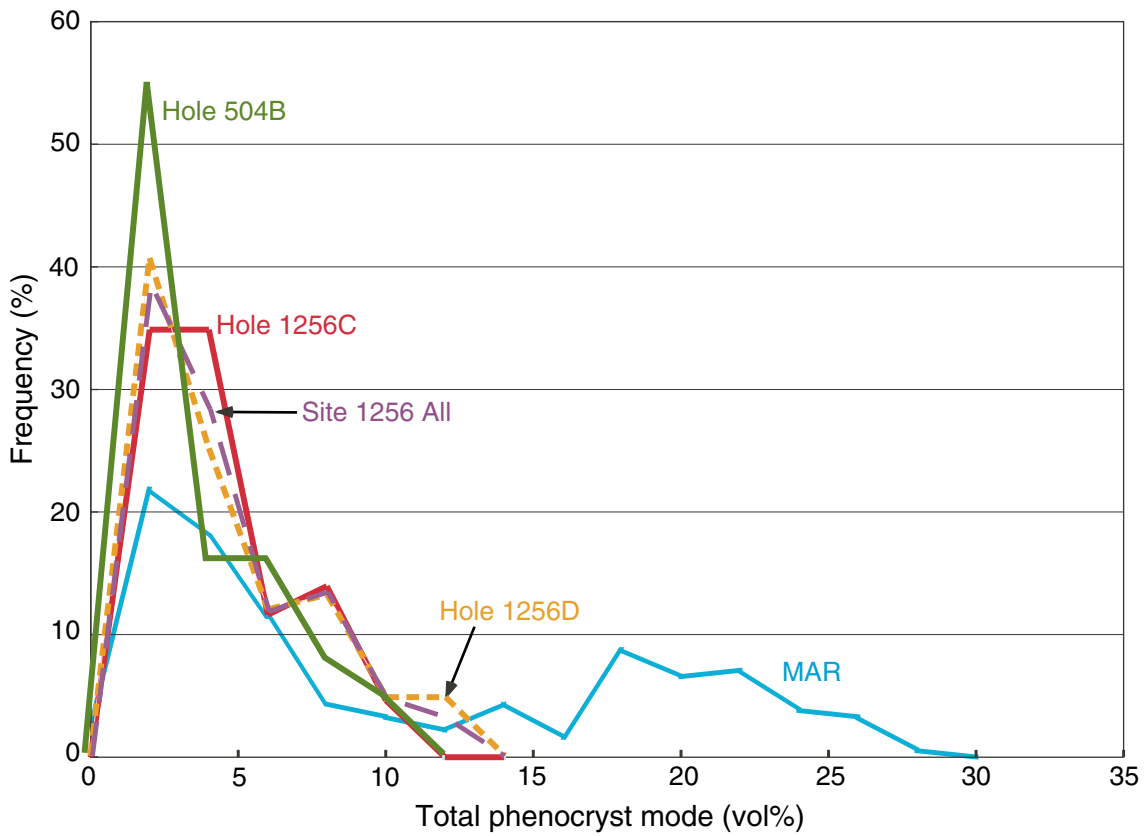


Figure F36. Proportion of phenocrystic clinopyroxene (Cpx)-plagioclase (Pl)-olivine (Ol) in basalts from Holes 1256C and 1256D in comparison with basalts from Hole 504B and the Mid-Atlantic Ridge (MAR).

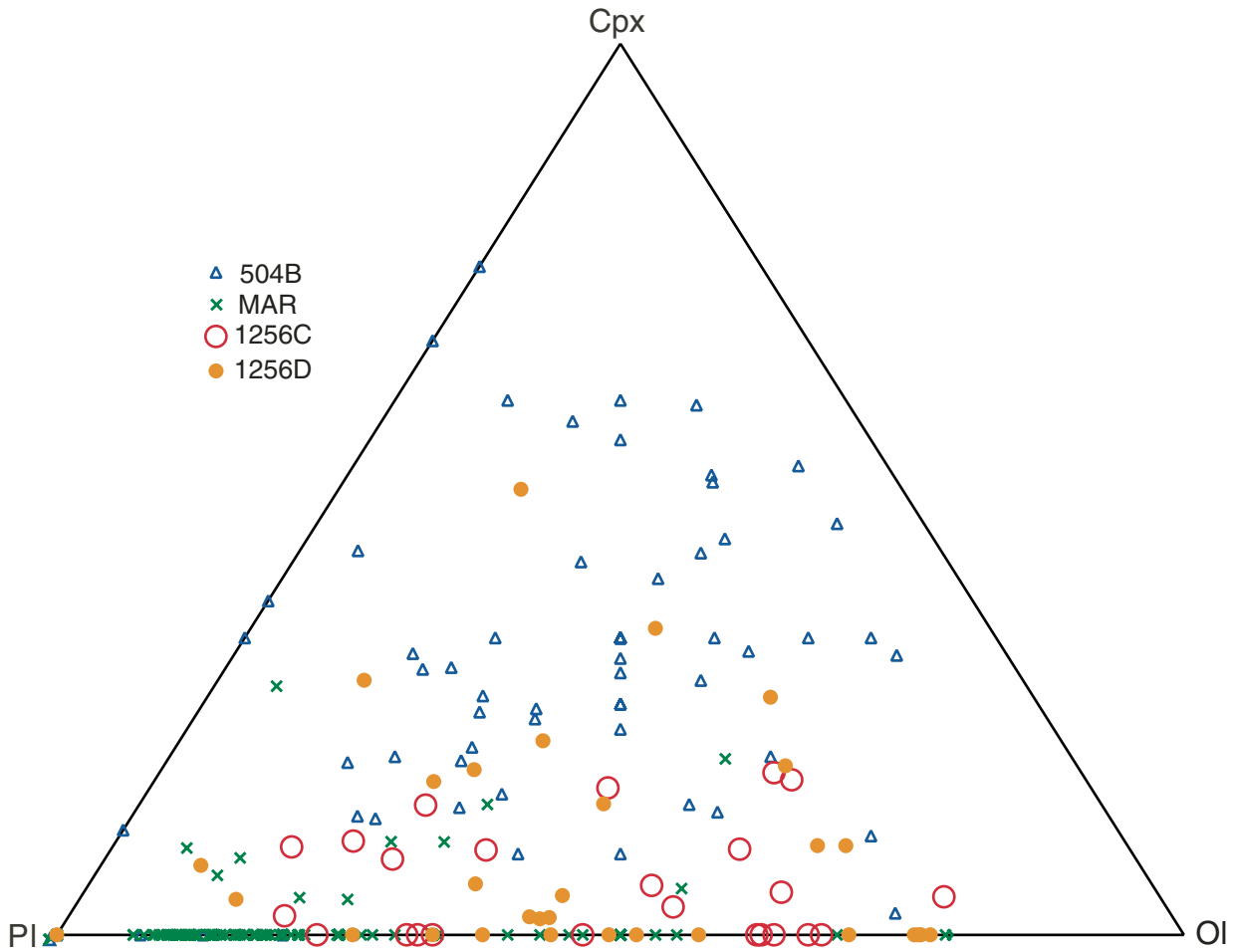
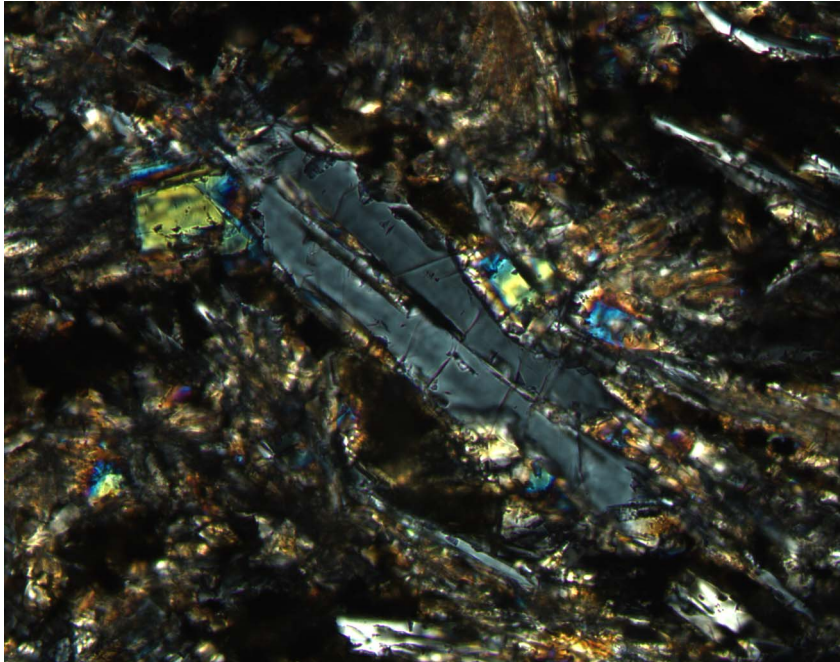


Figure F37. Photomicrographs showing plagioclase phenocryst clots (Sample 206-1256D-55R-2, 63–64 cm) (width of view = 0.7 mm). A. Normally zoned plagioclase partially enclosing augite microphenocrysts. B. Reversely zoned plagioclase clotted with augite and olivine. Note that augite microphenocrysts are not in direct contact with the riddled, resorbed core of plagioclase.

A



B

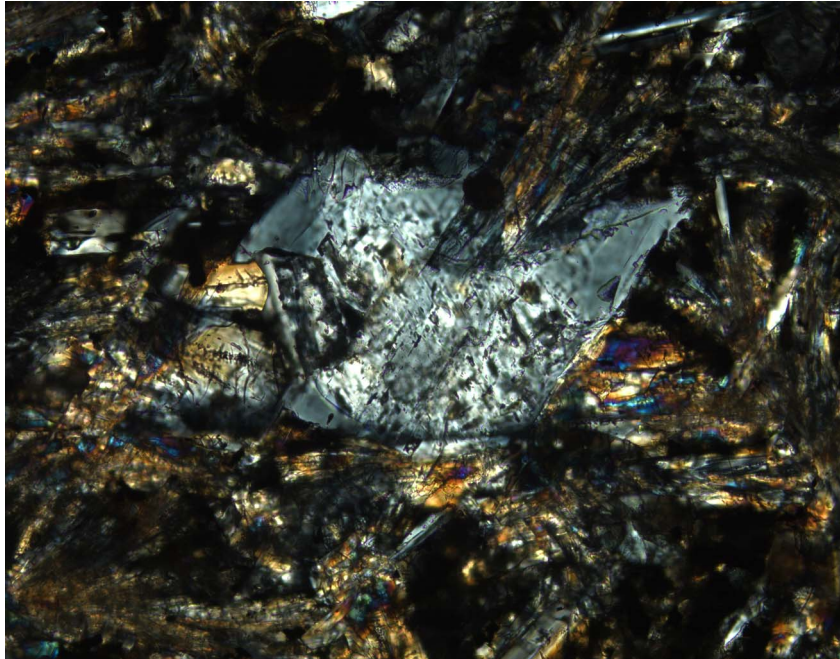


Figure F38. Plots of shipboard geochemical analyses vs. depth with igneous stratigraphy and units for comparison. Open symbols = Hole 1256C samples, h = hyaloclastite, a = altered basalt. (Continued on next four pages.)

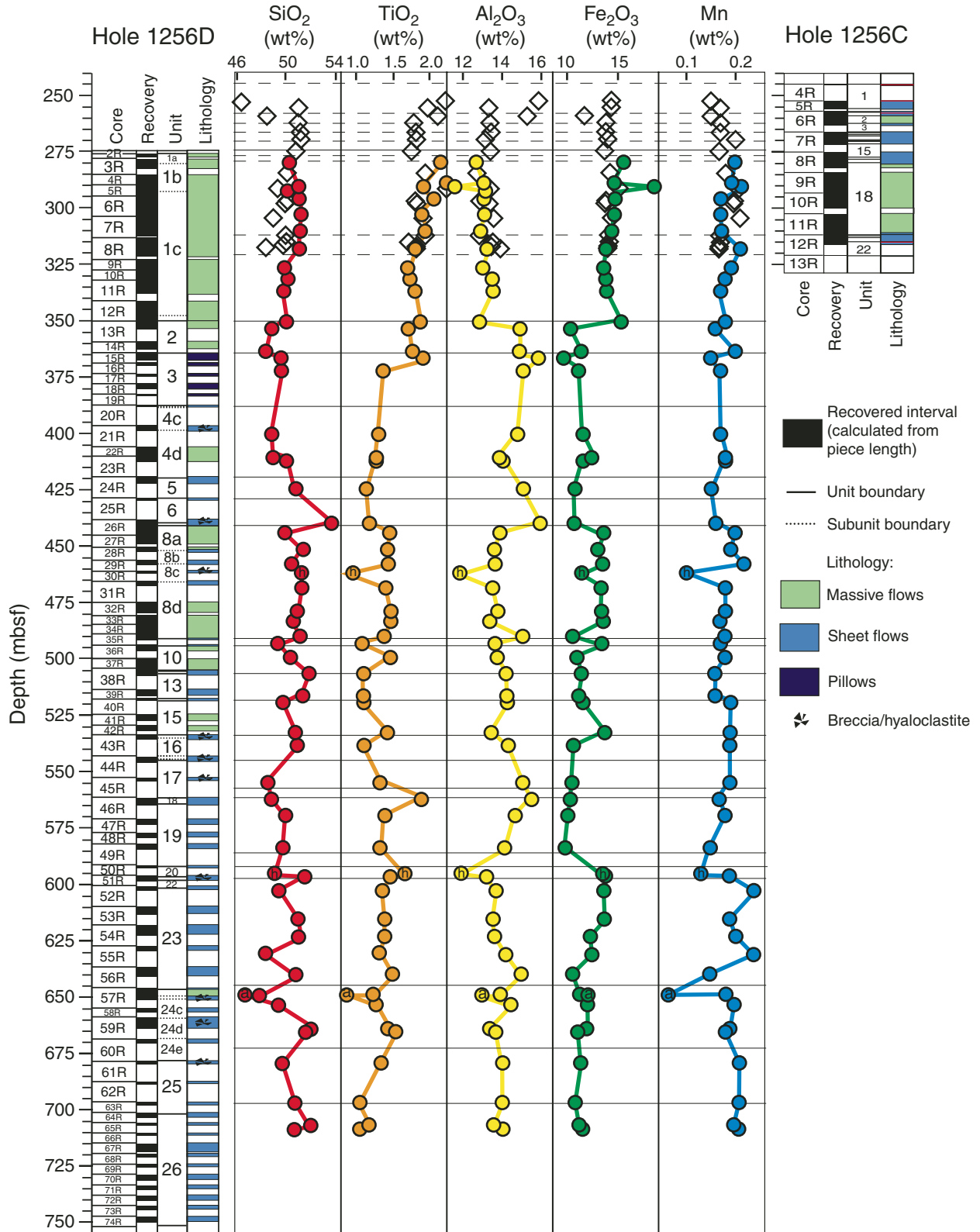


Figure F38 (continued).

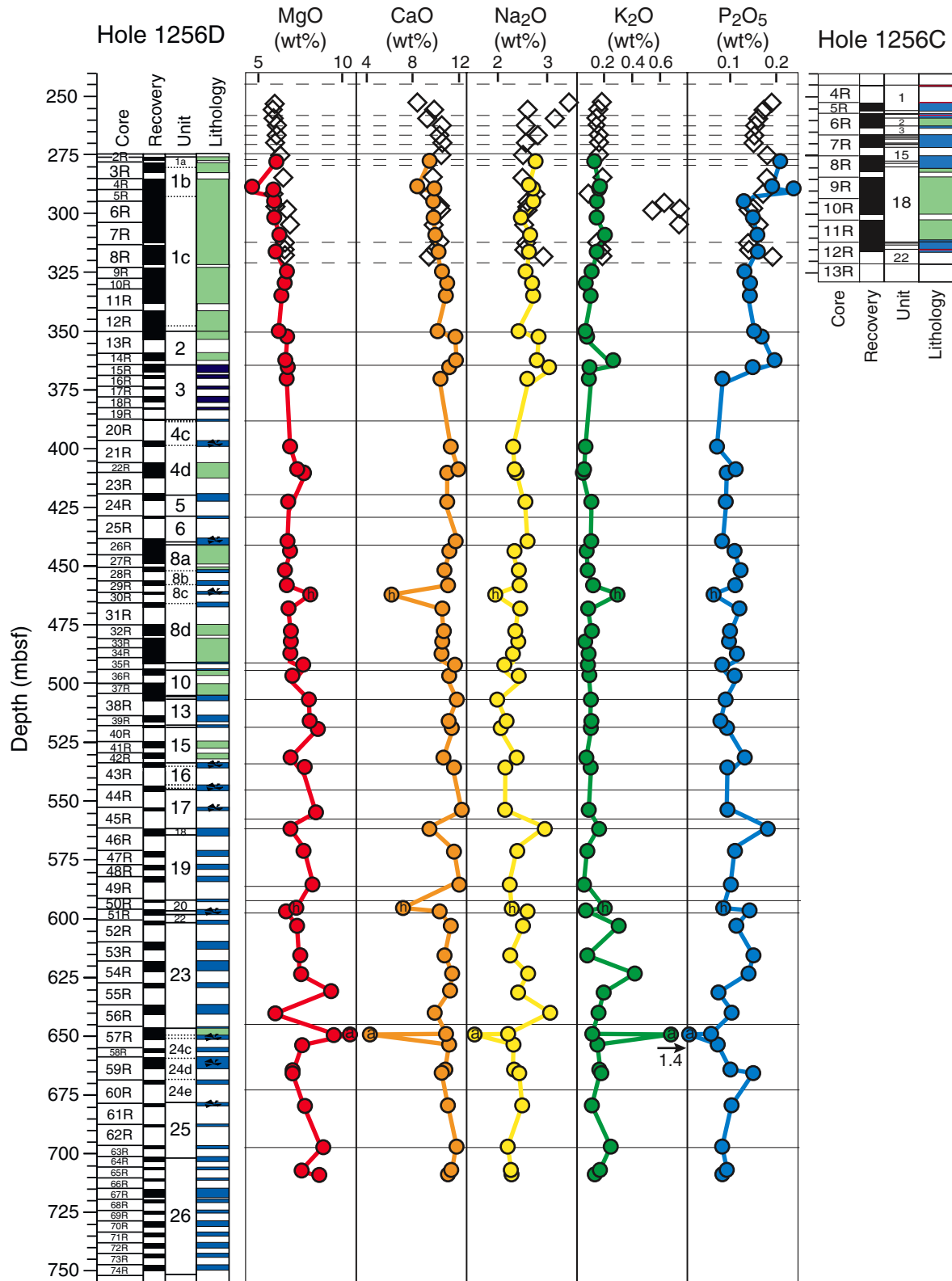


Figure F38 (continued).

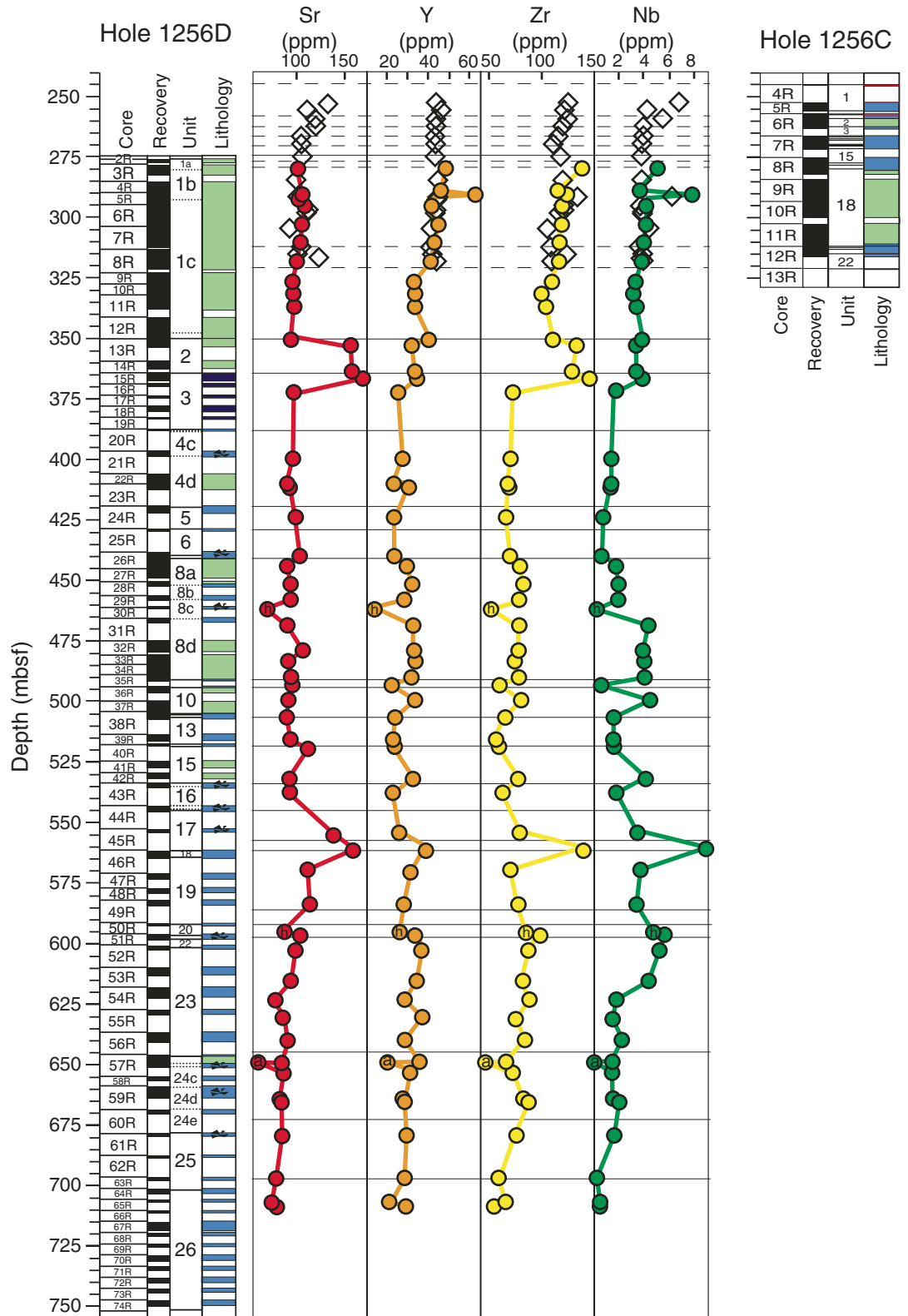


Figure F38 (continued).

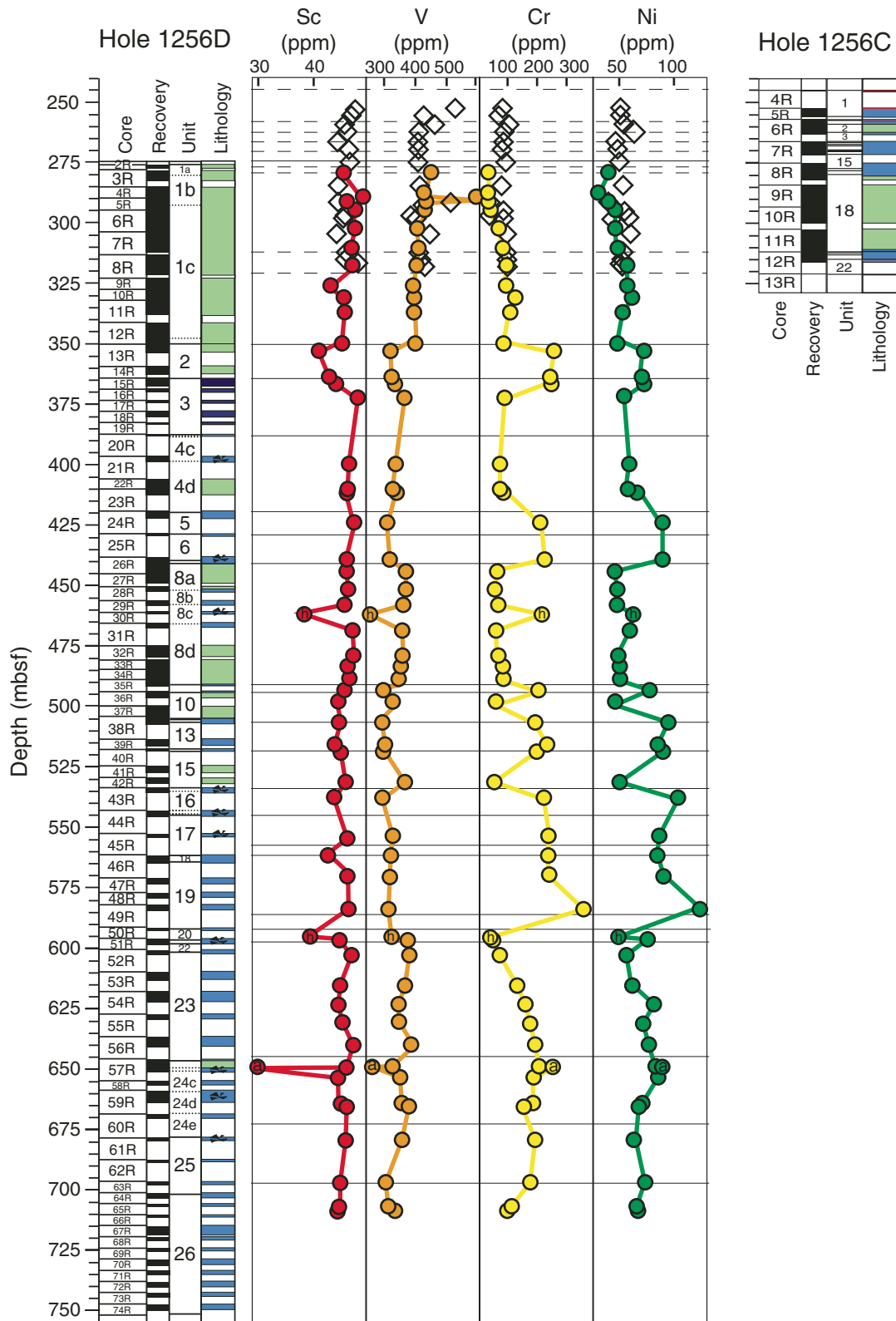


Figure F38 (continued).

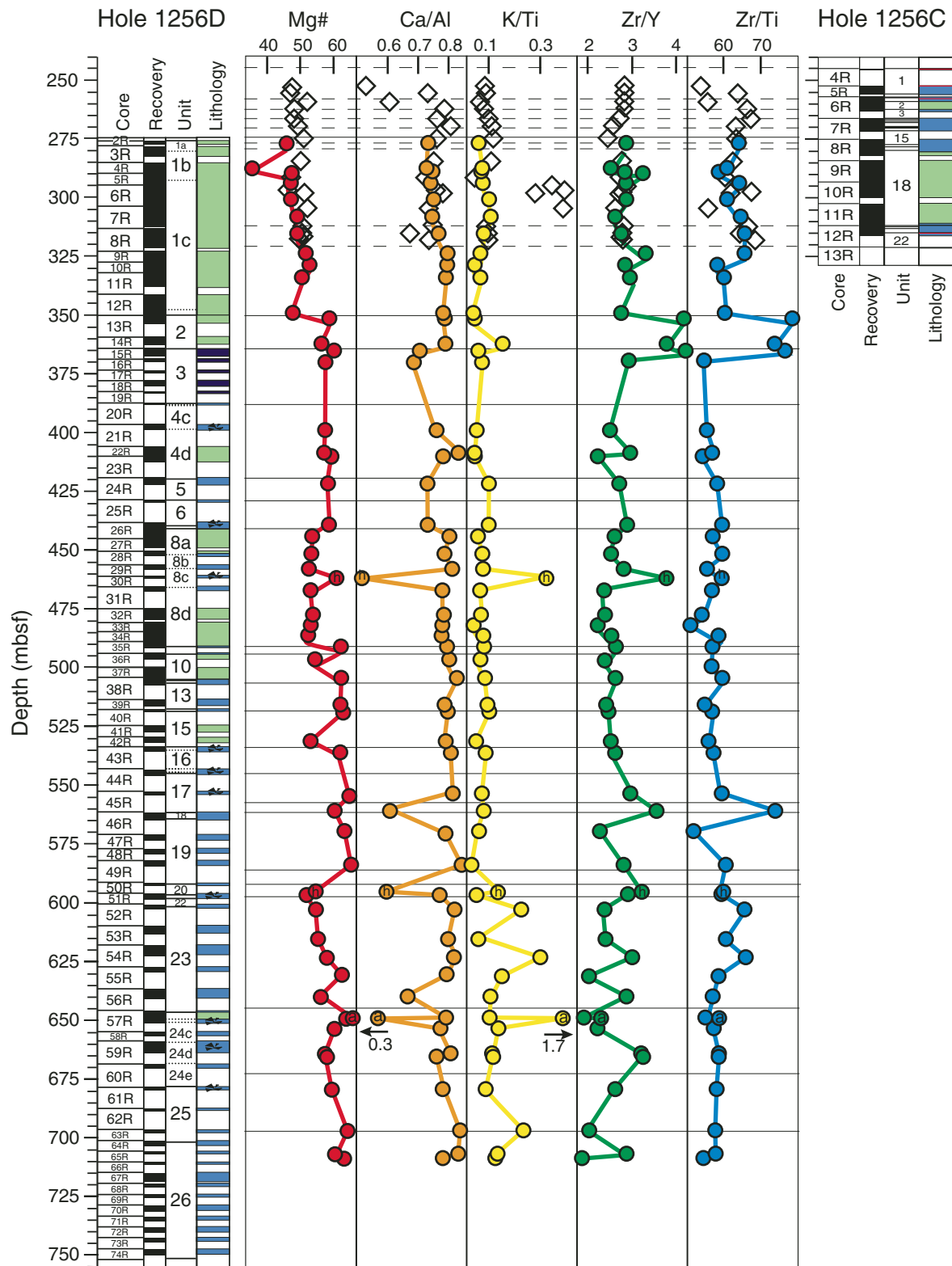


Figure F39. Nb-Zr-Y ternary diagram showing the fields for different basalt types. Samples taken from Site 1256 all lie in the N-MORB field. E-MORB = enriched mid-ocean-ridge basalt, N-MORB = normal mid-ocean-ridge basalt.

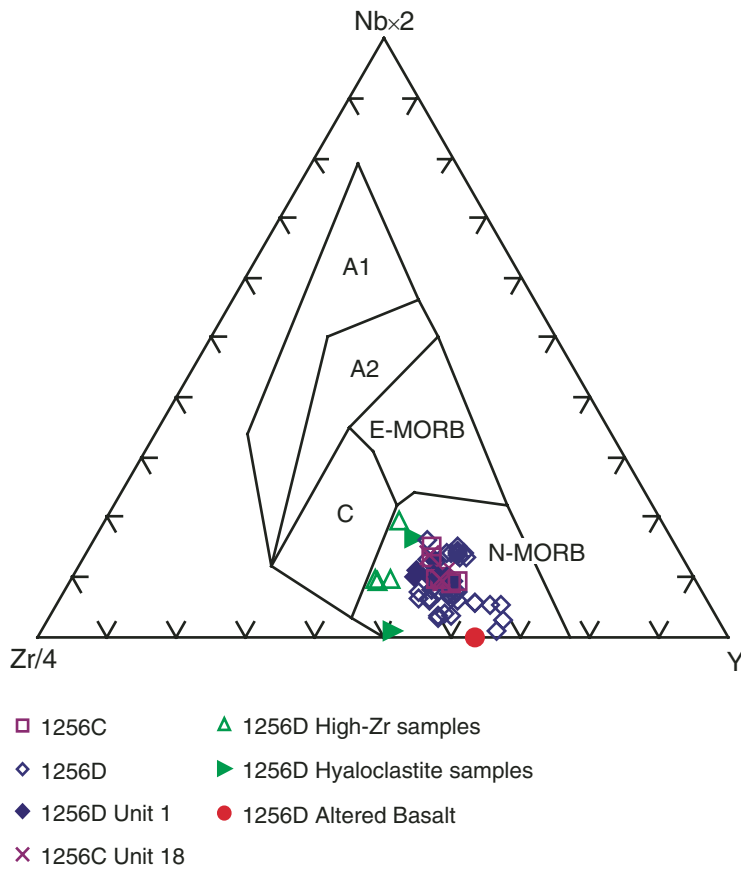


Figure F40. Zr vs. TiO₂ and Nb.

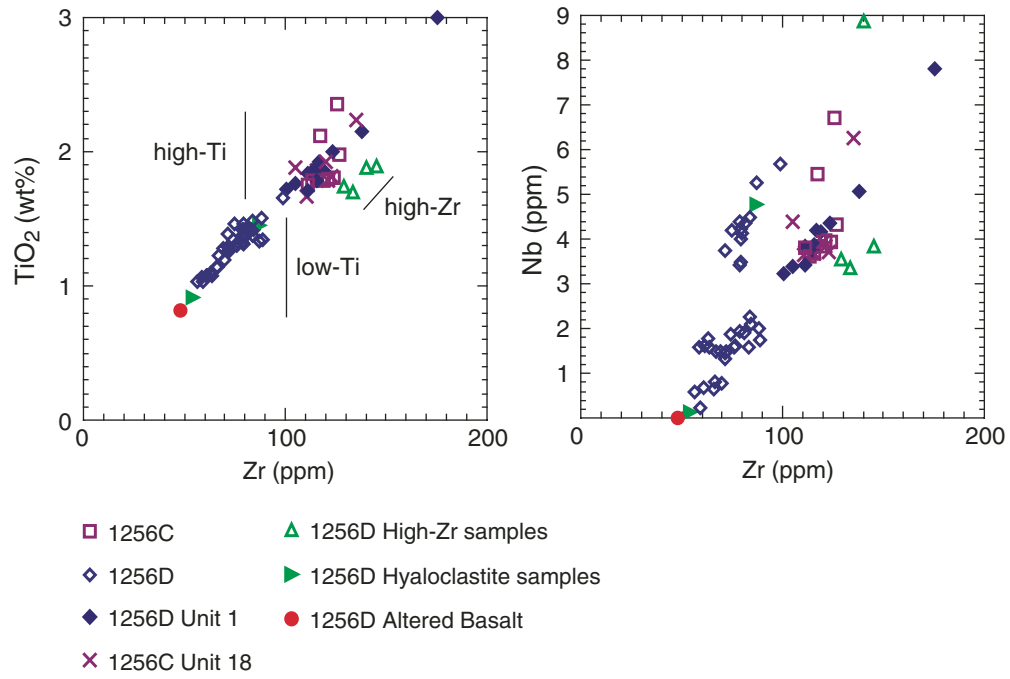


Figure F41. Plots of elemental abundance vs. MgO for all shipboard analyses. (Continued on next page.)

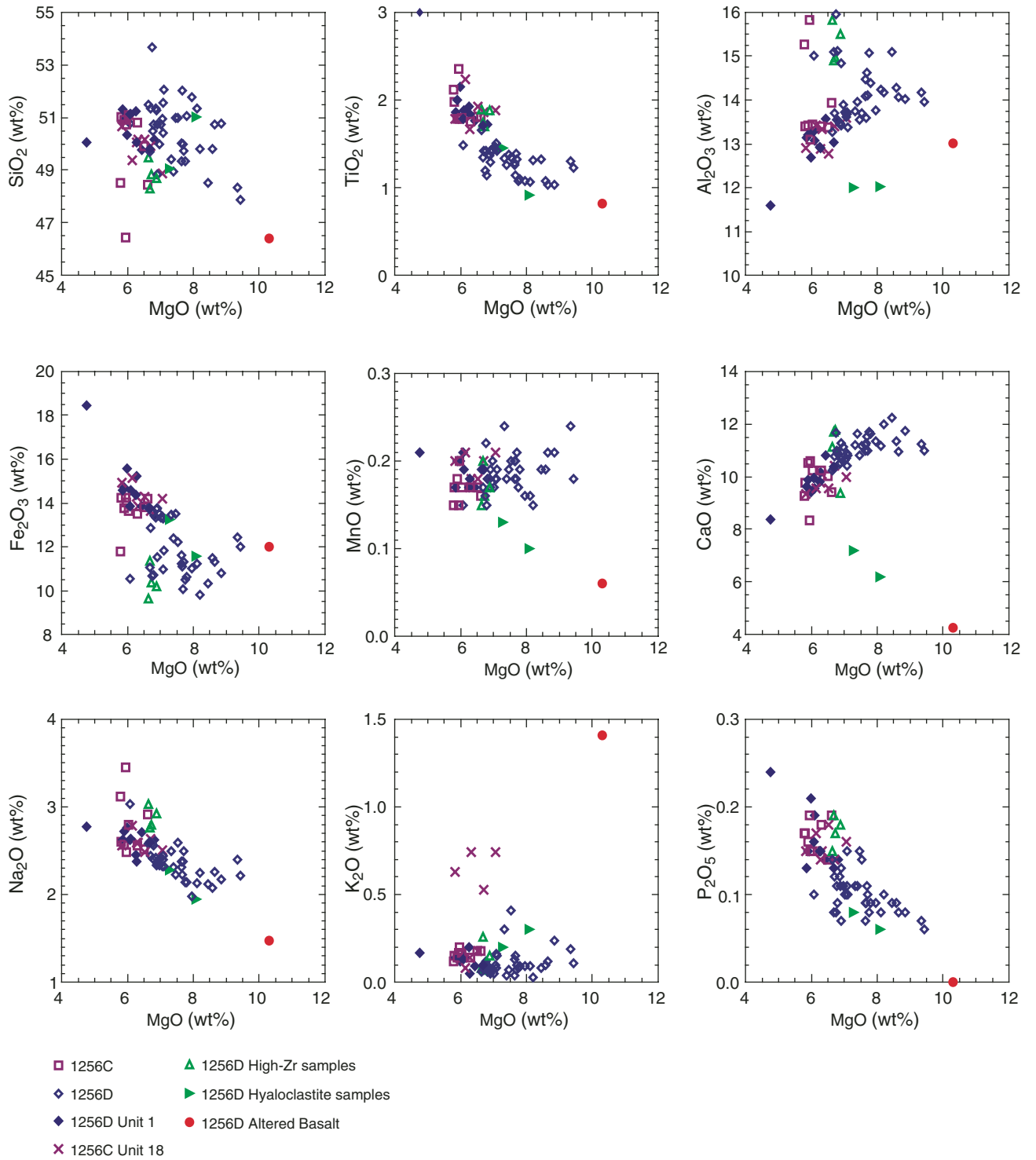
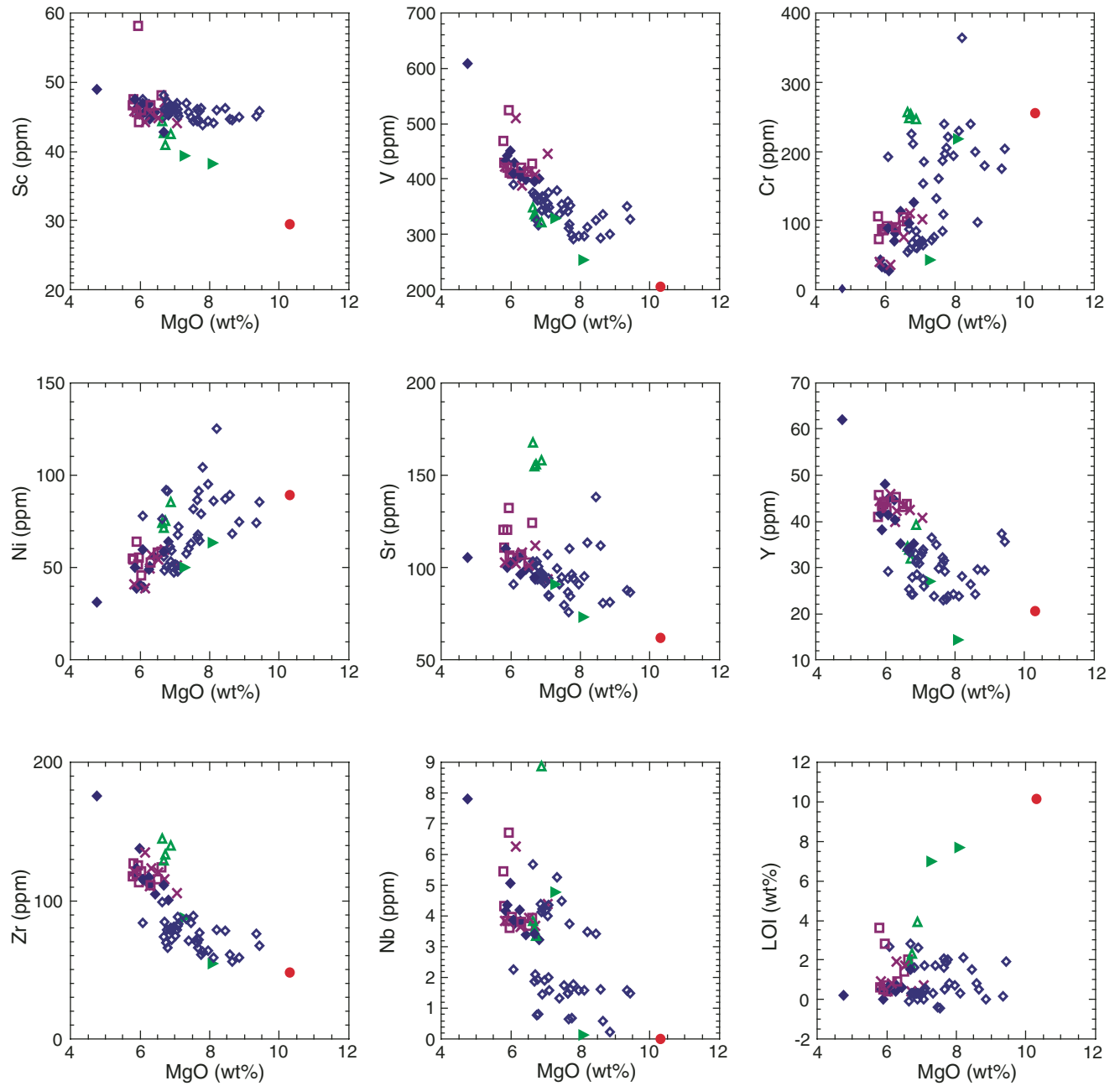


Figure F41 (continued).



- 1256C
- ◇ 1256D
- ◆ 1256D Unit 1
- × 1256C Unit 18
- ▲ 1256D High-Zr samples
- ▶ 1256D Hyaloclastite samples
- 1256D Altered Basalt

Figure F42. Distributions of alteration types with depth in Hole 1256D. Data are averaged for each core. Low-T = low temperature.

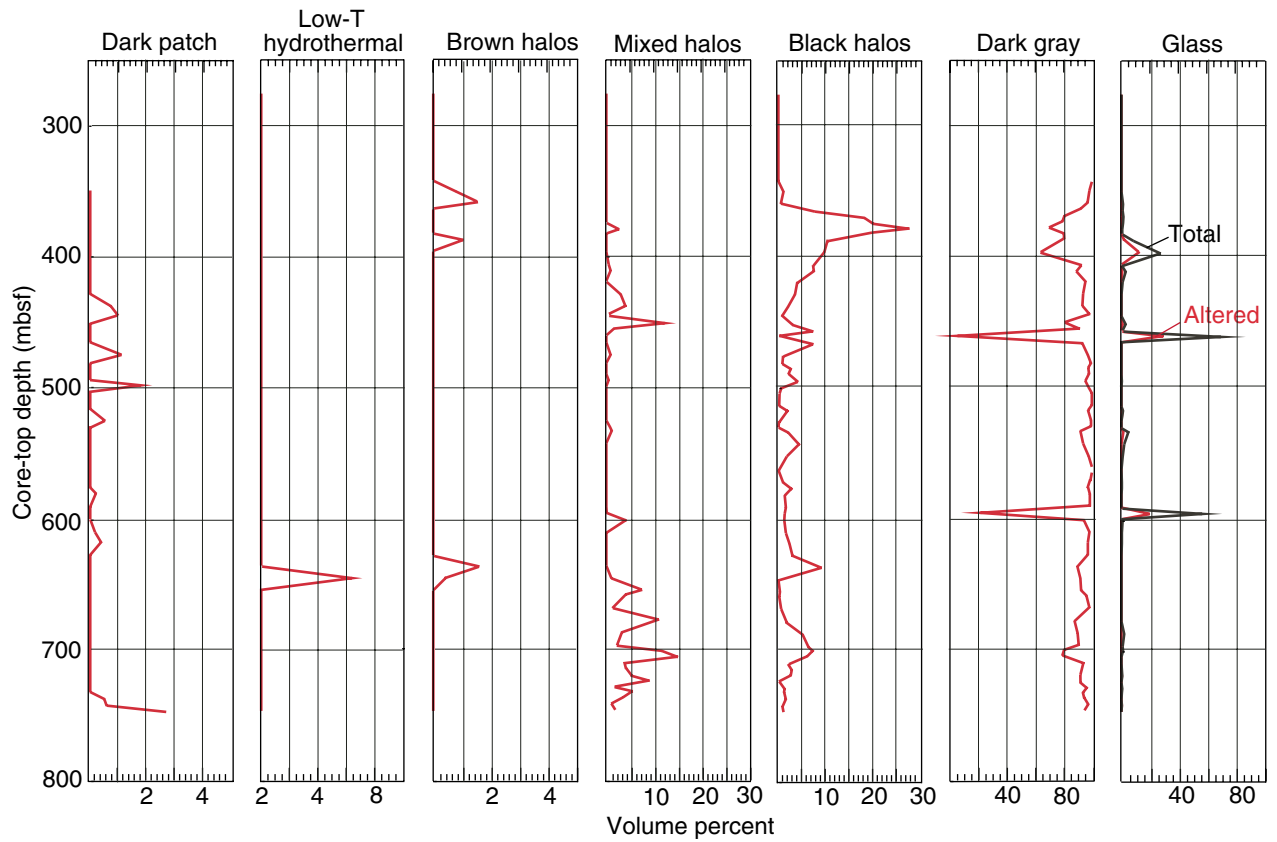


Figure F43. Distribution of secondary minerals with depth in Hole 1256D. Lines reflect presence or absence of a phase only. Note the late magmatic/hydrothermal minerals at 275–350 mbsf in massive Unit 1256D-1 and the appearance of secondary albite below 625 mbsf.

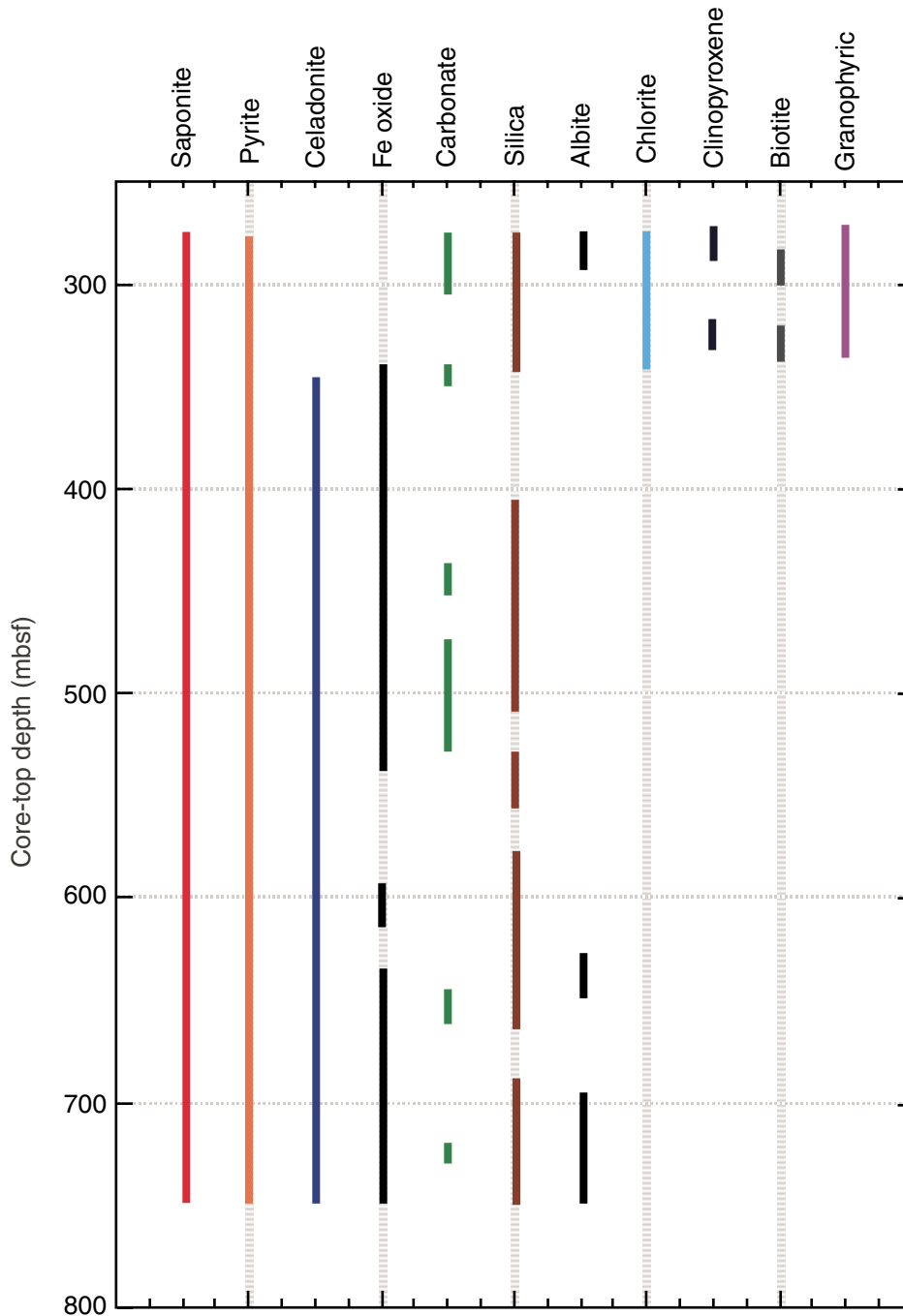


Figure F44. Total volume percent secondary minerals contained in veins, breccia, and interflow sediment with depth in Hole 1256D.

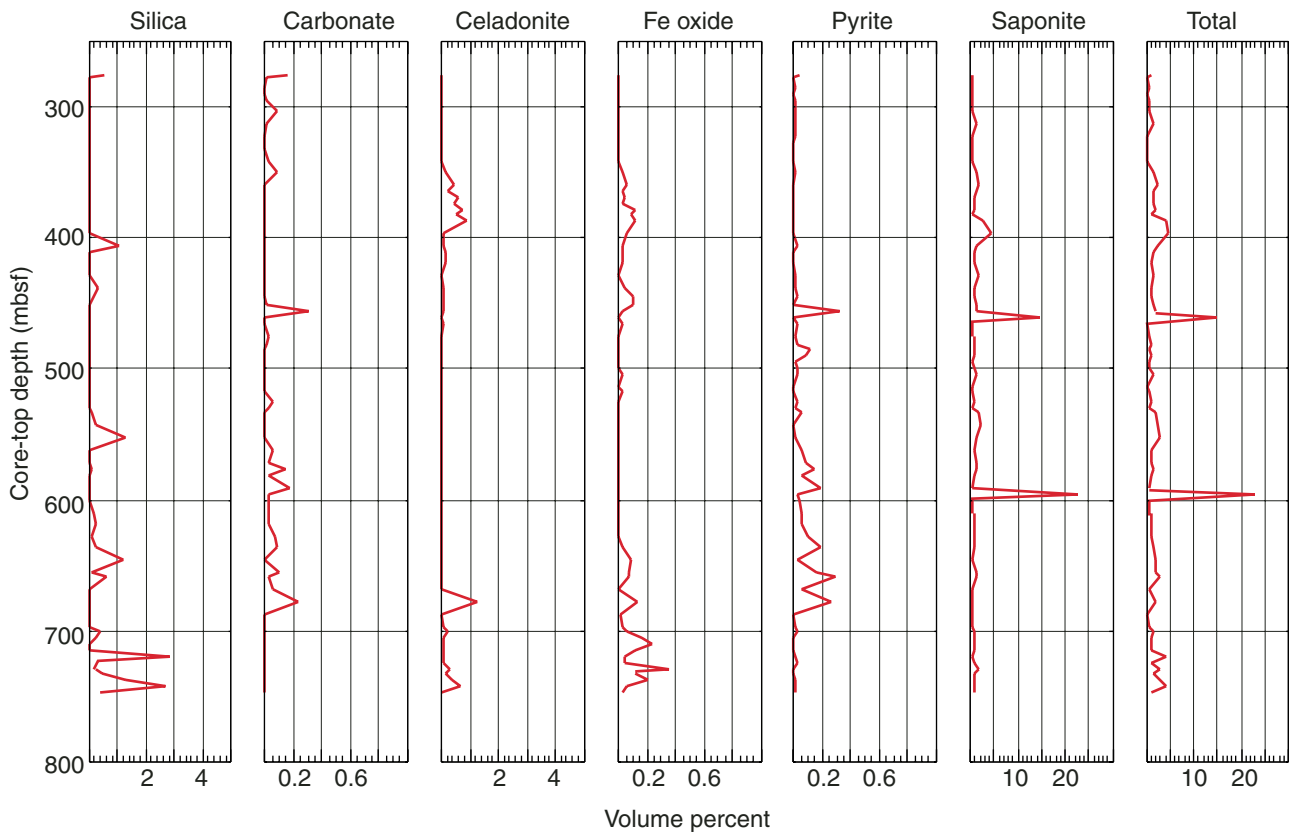


Figure F45. Abundance of secondary mineral veins with depth in Hole 1256D. Numbers of veins per core are normalized to the amount of recovered material per core (veins per meter).

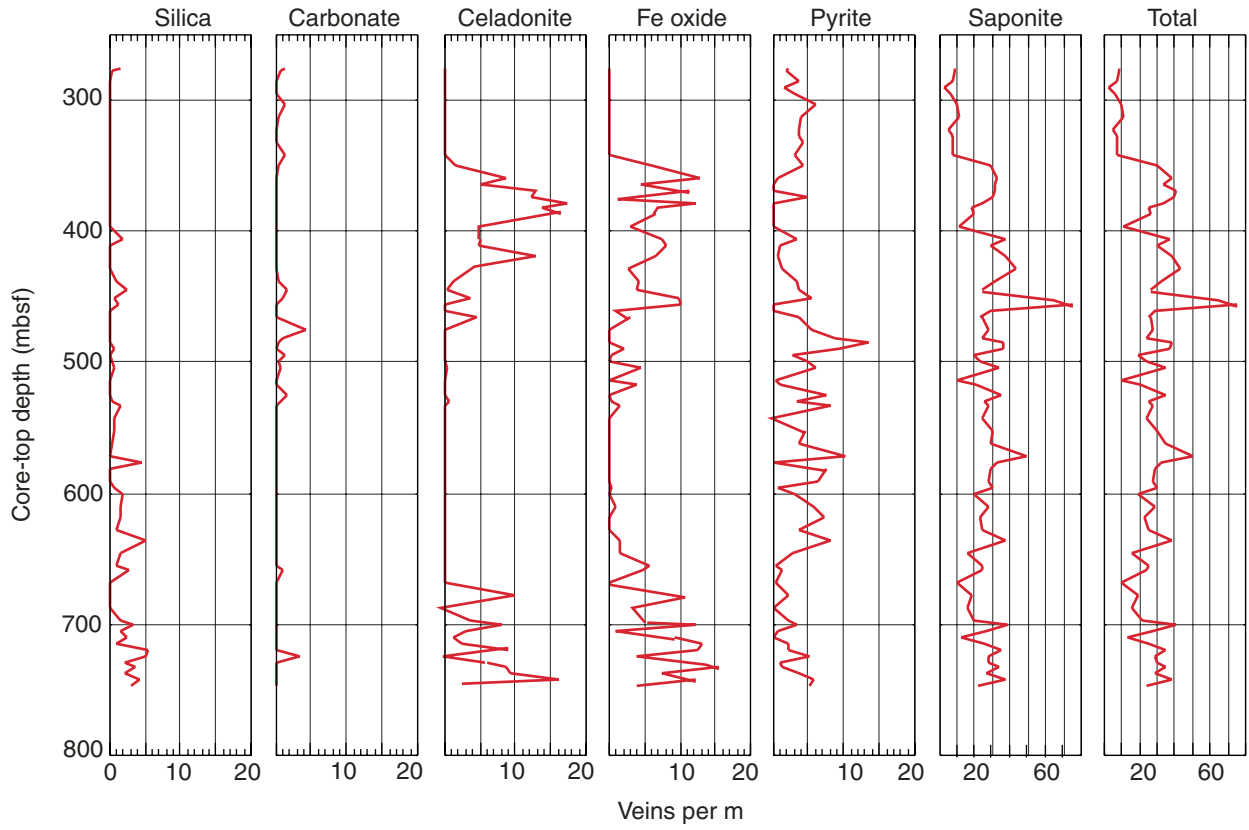


Figure F46. Volume percent secondary mineral veins with depth in Hole 1256D. Area percentages of veins on cut core surfaces are normalized to amount of recovered material per core, and area percentages are assumed equal to volume percentages.

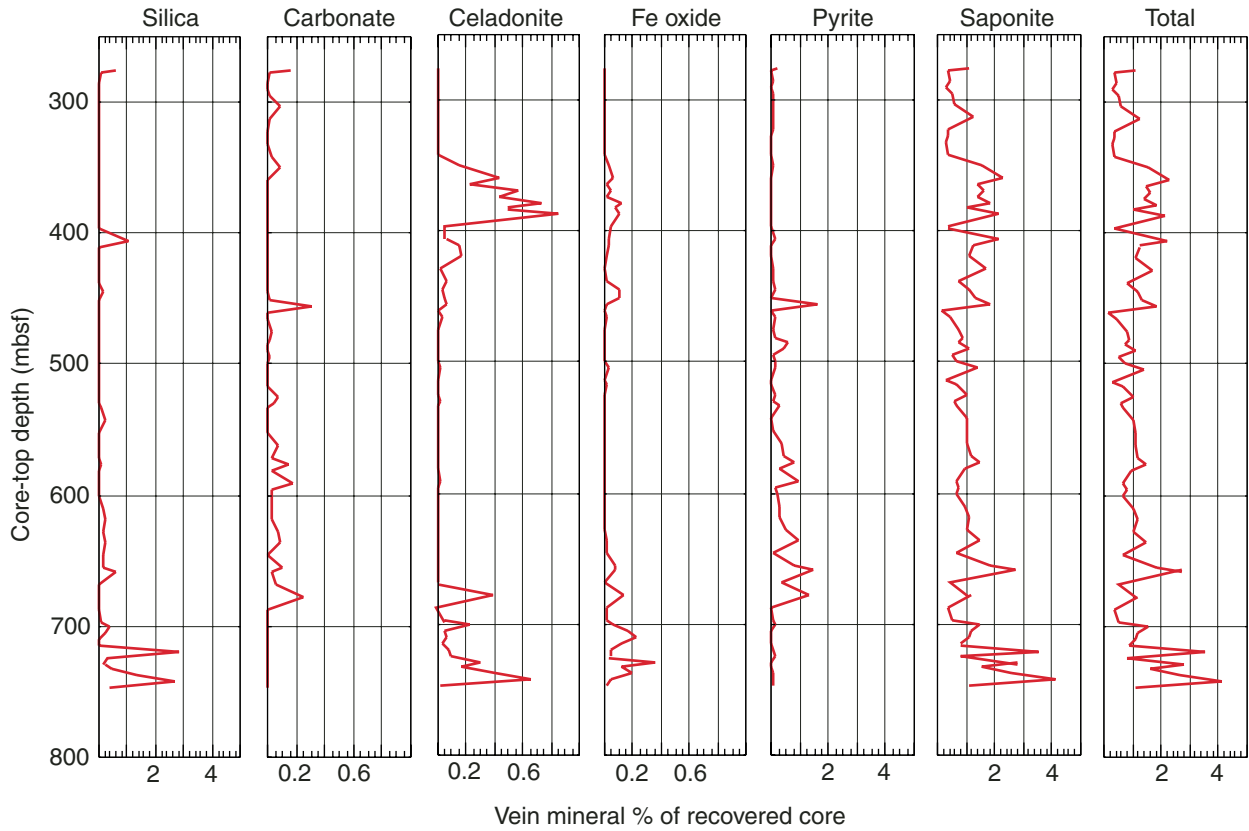


Figure F47. Distribution of alteration zones with depth in selected ODP basement sections (Alt, in press). Hole 1256D is shown for comparison.

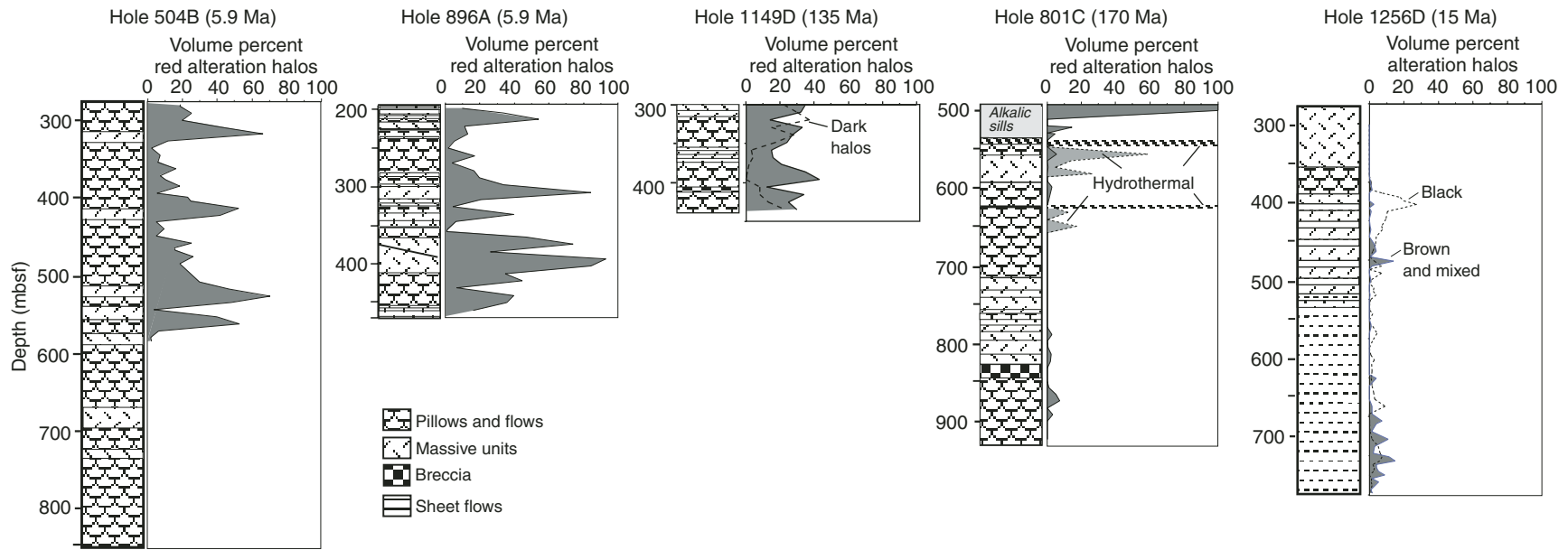


Figure F48. Occurrence of measured structures with depth, Hole 1256C. (Continued on next page.)

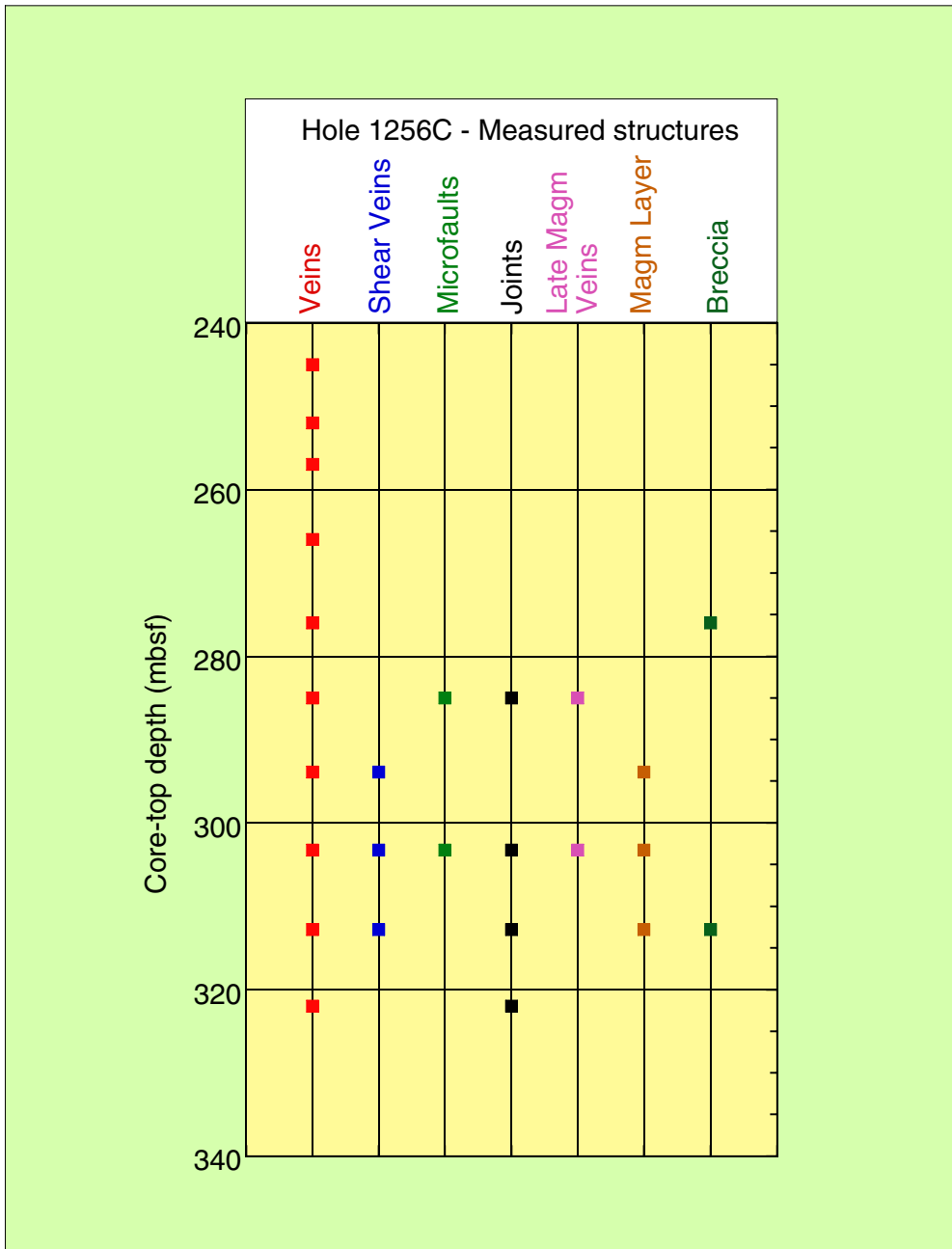


Figure F48 (continued). Hole 1256D.

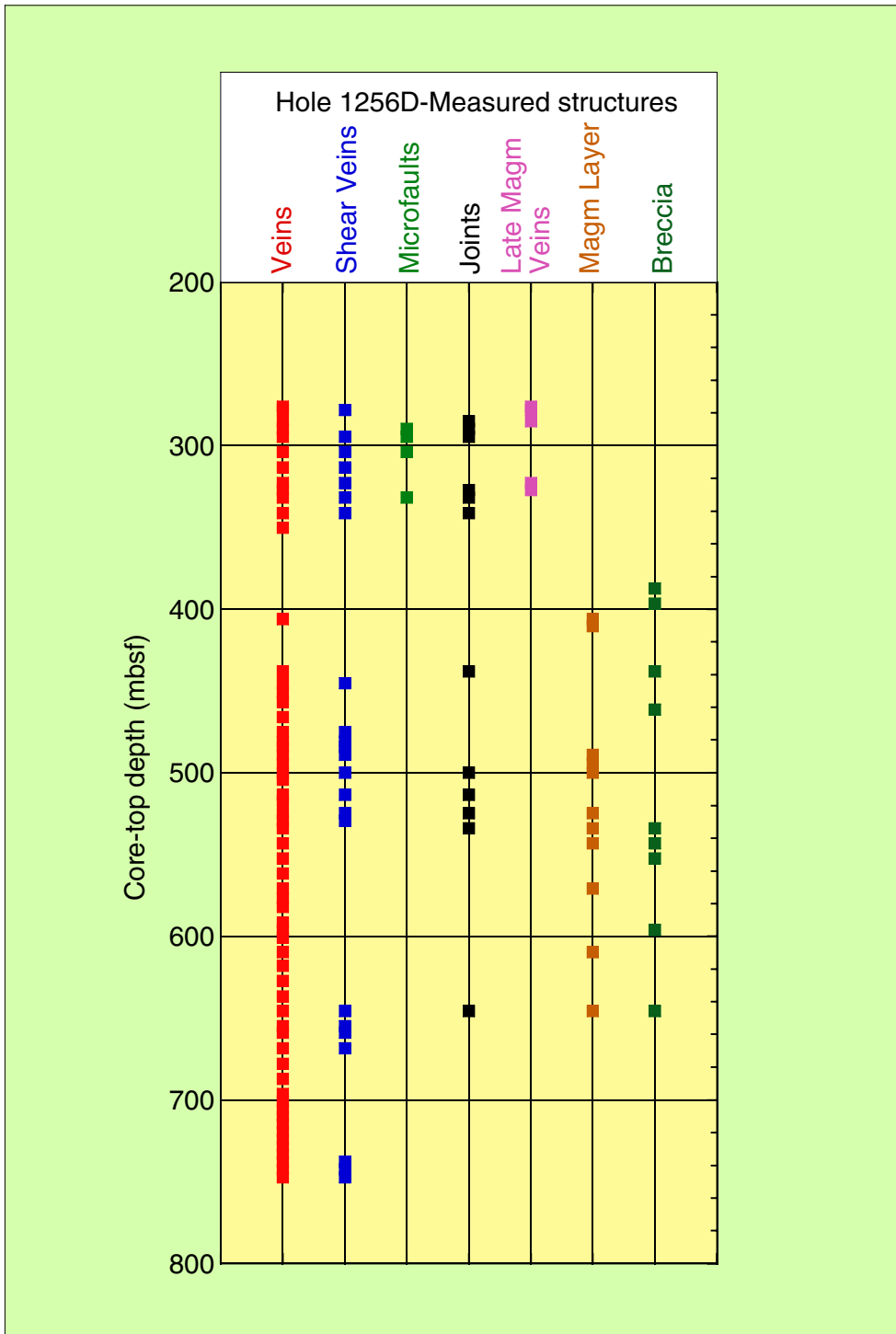


Figure F49. Rose diagrams of true dip values of all oriented structures for Holes 1256C and 1256D.

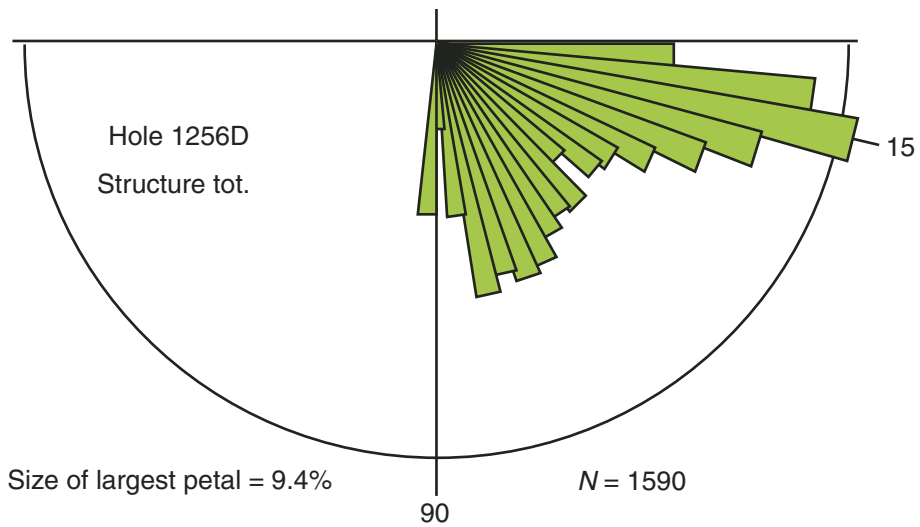
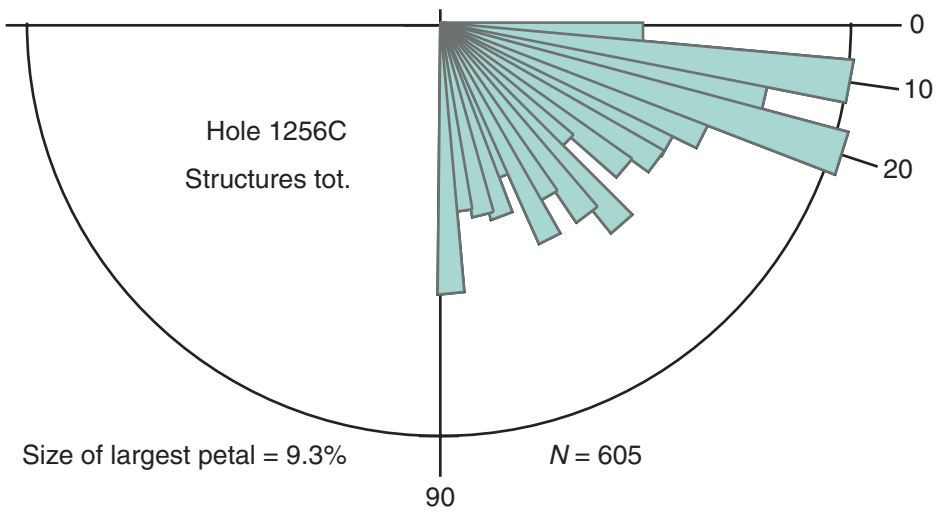
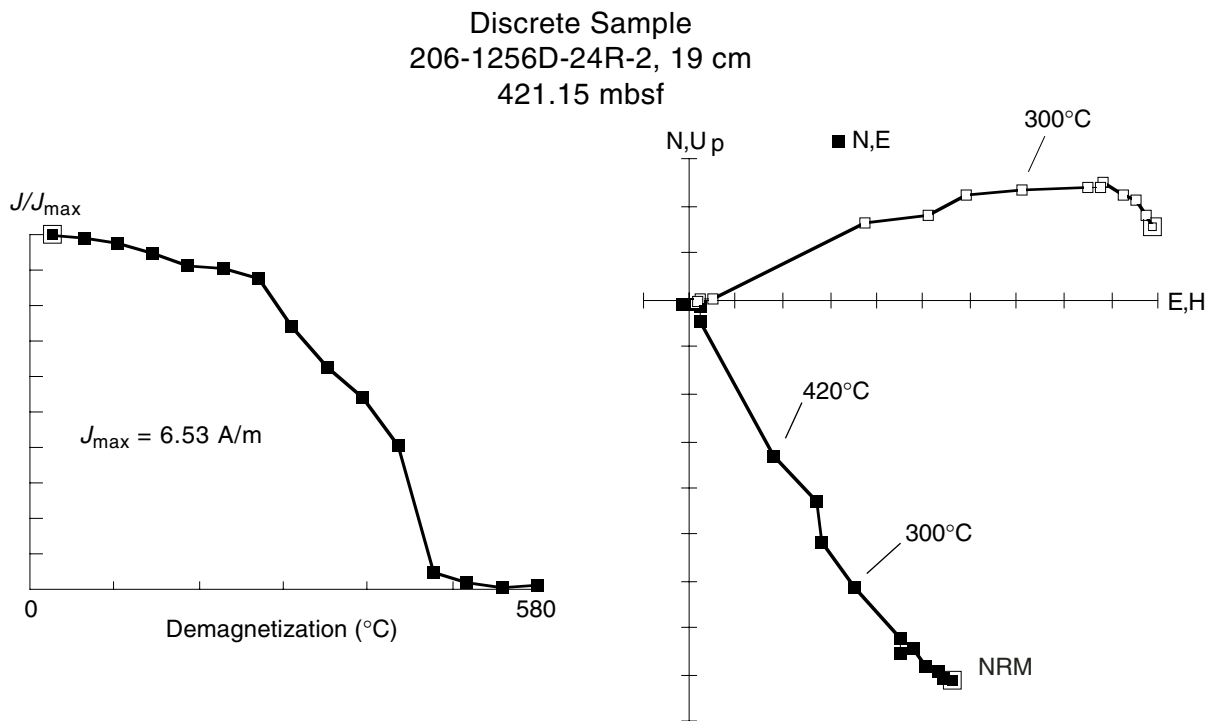


Figure F50. Thermal demagnetization plots for Sample 206-1256D-24R-2, 18–20 cm, a sample with relatively high blocking temperatures and little drilling overprint. Component plot at upper right shows north and east horizontal components as solid symbols and total horizontal and vertical components as open symbols.



Demag (°C)	Dec (°)	Inc (°)	Intensity (mT)
25.0	145.5	-9.2	6.53
60.0	146.1	-10.6	6.47
100.0	146.1	-12.7	6.38
140.0	146.9	-13.8	6.23
180.0	147.4	-16.1	5.99
220.0	149.2	-15.5	5.94
260.0	147.9	-16.0	5.75
300.0	150.1	-18.5	4.87
340.0	151.2	-21.1	4.11
380.0	147.6	-19.7	3.53
420.0	151.1	-24.3	2.68
460.0	152.1	-7.5	3.11e-1
500.0	124.6	-9.4	1.52e-1
540.0	217.7	23.0	6.58e-2
580.0	251.4	6.1	1.15e-1

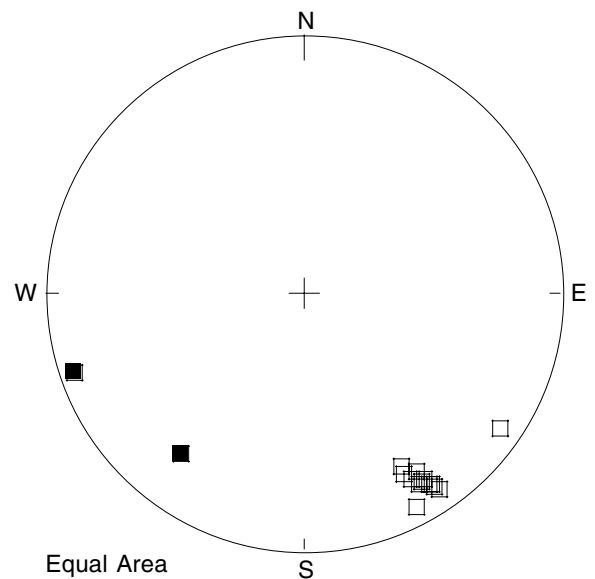


Figure F51. Alternating-field demagnetization plots for Sample 206-1256C-11R-3, 62–64 cm. This exceptionally stable sample appears to have the drilling overprint removed by 14 mT. Component plot at upper right shows north and east horizontal components as solid symbols and total horizontal and vertical components as open symbols.

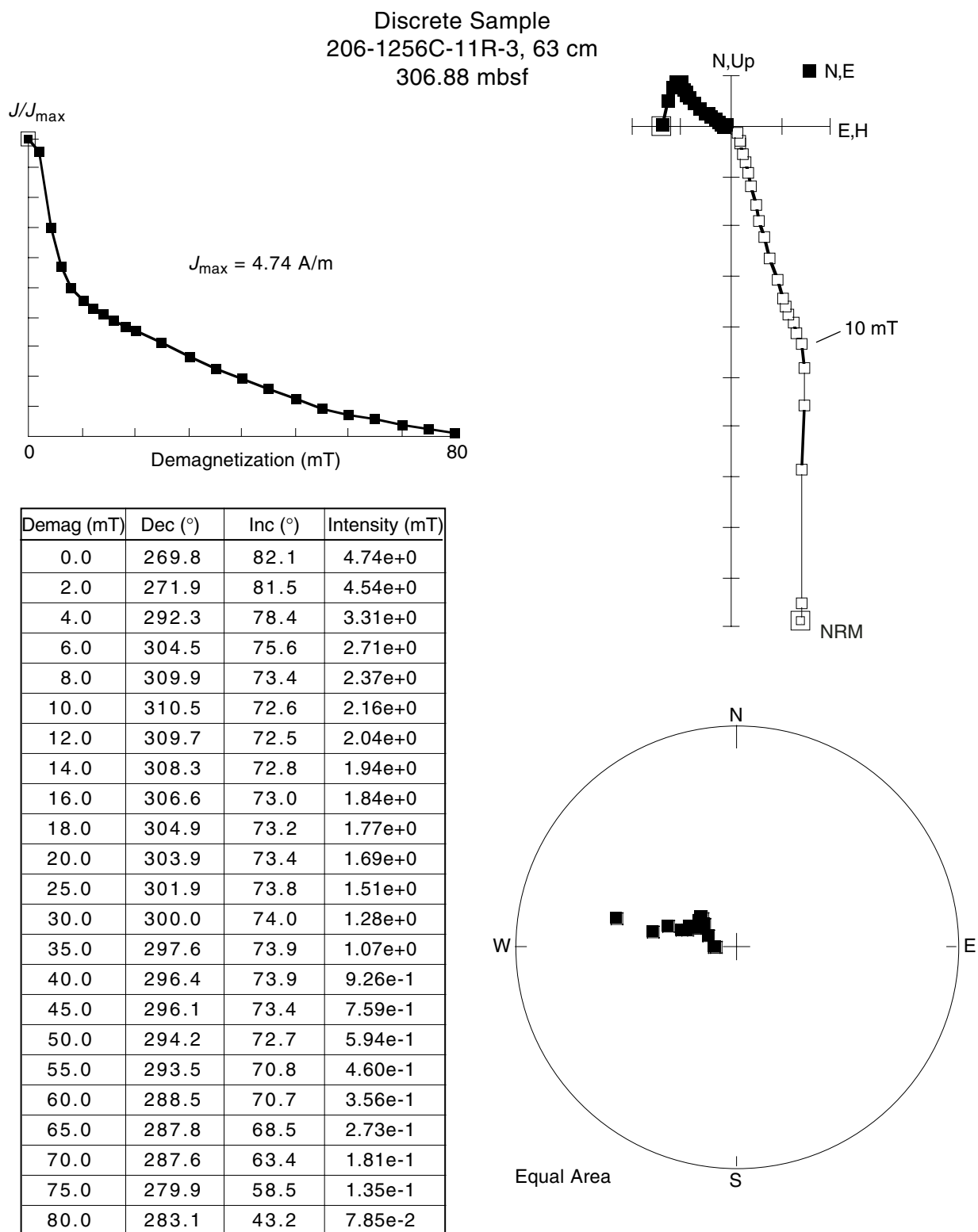


Figure F52. Summary of downhole logging results in Holes 1256C and 1256D. FMS and UBI images are not oriented. Laboratory physical property measurements of the porosity and bulk density are also plotted along with the graphic lithology log based on core descriptions in Hole 1256B.

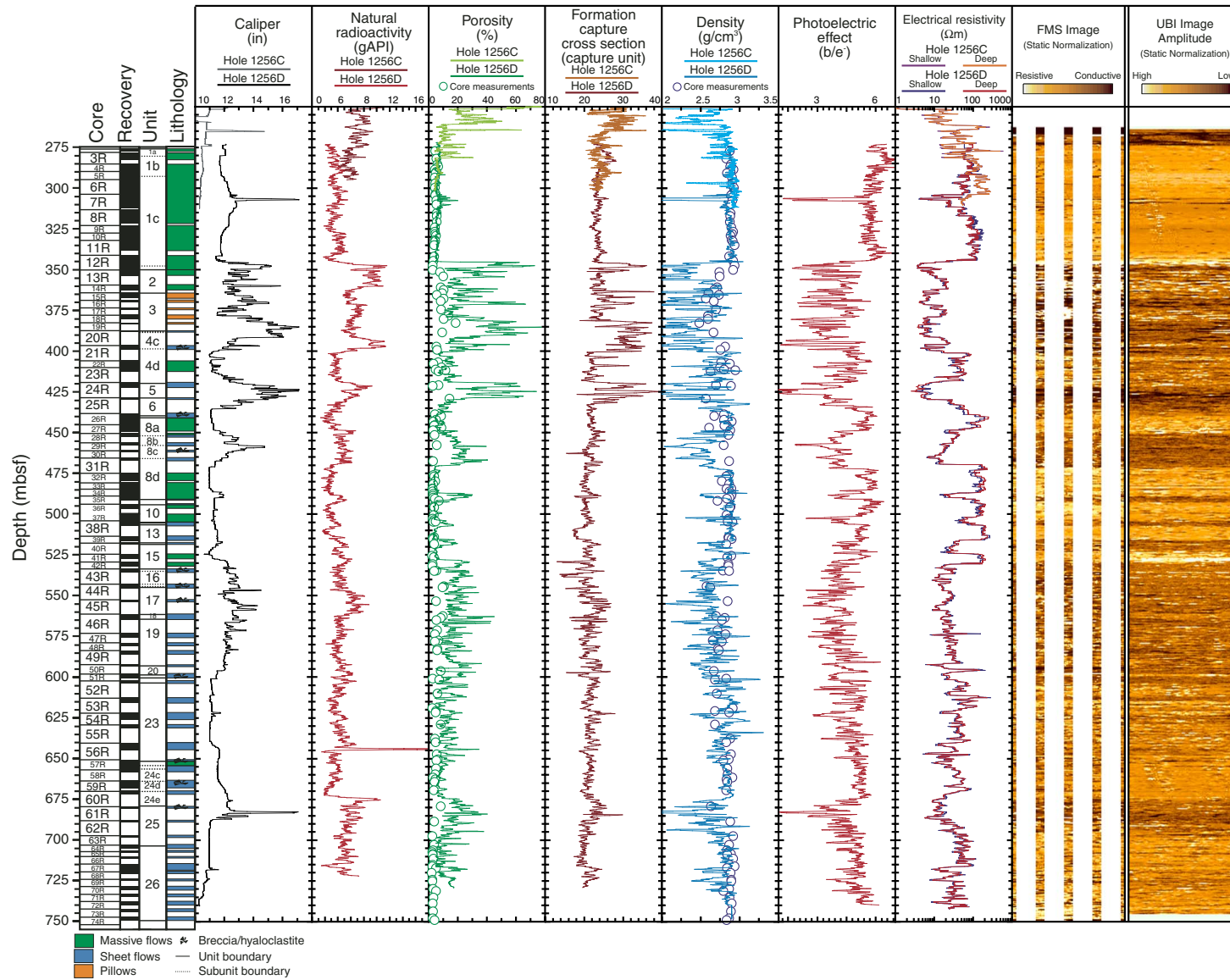


Figure F53. Comparison between unrolled core images from the massive ponded basalt (Subunit 1256D-1c) recovered in Section 206-1256D-6R-5 and Formation Microscanner (FMS)/Ultrasonic Borehole Imager (UBI) images from ~300 mbsf. Several features can be identified as potential matches on the whole-round core image and in the oriented image logs. The depth scale shown is the ODP curated depth, and core pieces have not been reoriented with respect to the FMS/UBI images because the DMT CoreLog Integra software that performs this routine was not functional during Leg 206.

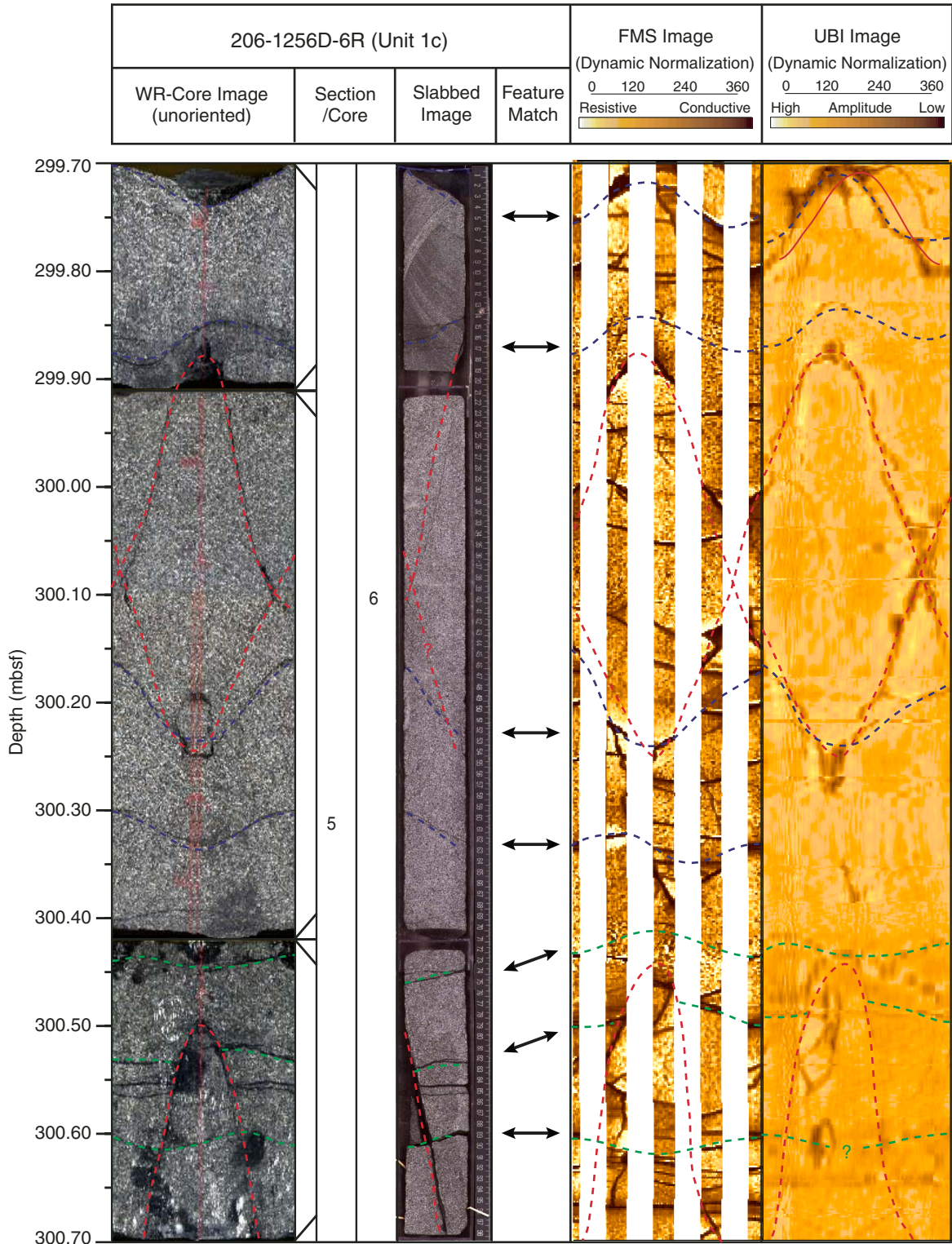


Table T1. Compilation of deep drill holes into in situ ocean basement, DSDP and ODP, 1968–2003. (See table notes. Continued on next page.)

Leg	Hole	Latitude	Longitude	Ocean	Water depth (m)	Age (Ma)	Sediment thickness (m)	Basement penetration (m)	Recovery (%)	Spreading rate	Comments	Lithology
24	238	11°09.21'S	70°31.56'E	Indian	2845	30	506	81	50	S/I	Projection of Chagos-Laccadive Plateau	Basaltic lavas
26	257	30°59.16'S	108°20.99'E	Indian	5278	120	262	65	50	S/I	Wharton Basin off Perth, Australia	Basaltic and breccia
34	319A	13°01.04'S	101°31.46'W	Pacific	4296	16	98	59	25	F	Bauer Deep, 13°S East Pacific Rise	Basaltic lavas
37	332A	36°52.72'N	33°38.46'W	Atlantic	1851	3.5	104	331	10	S	Mid-Atlantic Ridge 36–37°N	Basalt, basalt breccia, interlayered sediments
37	332B	36°52.72'N	33°38.46'W	Atlantic	1983	3.5	149	583	21	S	Mid-Atlantic Ridge 36–37°N	Basalt, basalt breccia
37	333A	36°50.45'N	33°40.05'W	Atlantic	1666	3.5	218	311	8	S	Mid-Atlantic Ridge 36–37°N	Basalt, basalt breccia
37	335	37°17.74'N	35°11.92'W	Atlantic	3188	15	454	108	38	S	Mid-Atlantic Ridge 36–37°N	Basaltic lavas
45	395A	22°45.35'N	46°04.90'W	Atlantic	4485	7.3	92	571	18	S	Mid-Atlantic Ridge 23°N	Basaltic lavas and breccia
45	396	22°58.88'N	43°30.95'W	Atlantic	4450	9	126	96	33	S	Mid-Atlantic Ridge 23°N	Basaltic lavas
46	396B	22°59.14'N	43°30.90'W	Atlantic	4459	13	151	255	23	S	Mid-Atlantic Ridge 23°N	Basalt and breccia
49	410A	45°30.53'N	29°28.56'W	Atlantic	2987	9	331	49	38	S	Mid-Atlantic Ridge 45°N	Basaltic lavas
49	412A	36°33.74'N	33°09.96'W	Atlantic	2626	1.6	163	131	18	S	Mid-Atlantic Ridge 33°N	Basalt flows and intercalating limestone
51–53	417A	25°06.63'N	68°02.48'W	Atlantic	5478	110	208	209	61	S	Western Atlantic	Basaltic lavas
51–53	417D	25°06.69'N	68°02.81'W	Atlantic	5479	110	343	366	70	S	Western Atlantic	Basaltic lavas
51–53	418A	25°02.10'N	68°03.44'W	Atlantic	5509	110	324	544	72	S	Western Atlantic	Basaltic lavas
54	428A	09°02.77'N	105°26.14'W	Pacific	3359	2.3	63	53	39	F	9°N East Pacific Rise	Basaltic lavas
63	469	32°37.00'N	120°32.90'W	Pacific	3803	17	391	63	34	I	Off California coast	Basaltic lavas
63	470A	28°54.46'N	117°31.11'W	Pacific	3555	15	167	49	33	I	Off California coast	Basaltic lavas
65	482B	22°47.38'N	107°59.60'W	Pacific	3015	0.5	137	93	54	I	Off Gulf of California	Massive basalt and interlayered sediment
65	482D	22°47.31'N	107°59.51'W	Pacific	3015	0.5	138	50	50	I	Off Gulf of California	Massive basalt and interlayered sediment
65	483	22°53.00'N	108°44.90'W	Pacific	3084	2	110	95	40	I	Off Gulf of California	Massive basalt and pillow basalt with interlayered sediments
65	483B	22°52.99'N	108°44.84'W	Pacific	3084	2	110	157	47	I	Off Gulf of California	Massive basalt and pillow basalt with interlayered sediments
65	485A	22°44.92'N	107°54.23'W	Pacific	2997	1.2	154	178	51	I	Off Gulf of California	Massive basalt and interlayered sediments
68	501	01°13.63'N	83°44.06'W	Pacific	3467	6.6	264	73	60	I	South flank of Costa Rica Rift	Basaltic lavas
82	559	35°07.45'N	40°55.00'W	Atlantic	3754	35	238	63	37	S	West flank of Mid-Atlantic Ridge 35°N	Basaltic lavas
82	562	33°08.49'N	41°40.76'W	Atlantic	3172	12	240	90	45	S	West flank of Mid-Atlantic Ridge 33°N	Pillow basalt and massive basalt
82	564	33°44.36'N	43°46.03'W	Atlantic	3820	35	284	81	43	S	West flank of Mid-Atlantic Ridge 34°N	Pillow basalt and minor massive basalt
91	595B	23°49.34'S	165°31.61'W	Pacific	5620	80	70	54	28	F	Central South Pacific	Vesicular aphyric basalt
92	597C	18°48.43'S	129°46.22'W	Pacific	4147	30	53	91	53	F	West flank South East Pacific Rise 18°S	Massive basalt flows
106/109	648B	22°55.320'N	44°56.825'W	Atlantic	3326	0	0	50	12	S	Mid-Atlantic Ridge 23°N	Pillow basalt
123	765D	15°58.560'S	117°34.51'E	Indian	5714	140	928	267	31	F	Argo Abyssal Plain	Normal-enriched MORB basaltic lavas
129/185	801C*	18°38.538'N	156°21.59'E	Pacific	5674	170	462	414	47	F	Western North Pacific	Pillow basalt, basalt flows, breccias
136	843B	19°20.54'N	159°5.68'W	Pacific	4418	95	243	71	37	F	West of Hawaii	Basaltic lavas
69/70/83/111/137/140/148	504B	1°13.611'N	83°43.818'W	Pacific	3463	6.9	274.5	1836.5	20	I	South flank of Costa Rica Rift	Basalt, stockwork, diabase
148	896A	1°13.006'N	83°43.392'W	Pacific	3448	6.9	179	290	27	I	South flank of Costa Rica Rift	Basaltic lavas
185	1149D	31°18.79'N	143°24.03'E	Pacific	5818	133	307	133	17	F	Western North Pacific	Pillow basalt, basalt flows, breccias
187	1162B	44°37.9'S	129°11.3'E	Indian	5464	18	333	59	17	I	Australian-Antarctic Discordance	Basaltic lavas and breccia
187	1163A	44°25.5'S	126°54.5'E	Indian	4354	17	161	47	33	I	Australian-Antarctic Discordance	Basaltic lavas
187	1164B	43°45.0'S	127°44.8'E	Indian	4798	18.5	150	66	16	I	Australian-Antarctic Discordance	Basaltic lavas
191	1179D	41°04.8'N	159°57.8'E	Pacific	5564	129	377	98	44	F	Western North Pacific	Basaltic lavas
200	1224F	27°53.36'N	141°58.77'W	Pacific	4967	46	28	147	26	F	Central Pacific	Basaltic lavas

Table T1 (continued).

Leg	Hole	Latitude	Longitude	Ocean	Water depth (m)	Age (Ma)	Sediment thickness (m)	Basement penetration (m)	Recovery (%)	Spreading rate	Comments	Lithology
203	1243B	5°18.07'N	110°04.58'W	Pacific	3868	11	110	87	25	F	Western flank of East Pacific Rise 5°N	Basaltic lavas
206	1256C	6°44.18'N	91°56.06'W	Pacific	3635	15	251	89	61	F	Cocos Plate eastern flank East Pacific Rise	Basaltic lavas
206	1256D	6°44.16'N	91°56.06'W	Pacific	3635	15	251	502	48	F	Cocos Plate eastern flank East Pacific Rise	Basaltic lavas

Notes: S = slow (<40 cm/m.y.), I = intermediate, F = fast (>80 cm/m.y.). The holes listed here sampled normal mid-ocean-ridge basalt (N-MORB) crust formed at bare rock mid-ocean ridges and were initiated in lavas. We have not included holes from arc settings or holes spudded into plutonic rocks at tectonic windows or transform faults. Table adapted from separate compilations of hard rock drill holes by W. Bach, J. Alt, and D. Teagle. * = 60.2 m of alkali basalt sills that were intruded at the sediment/basement boundary some 20 m.y. after the formation of the crust in Hole 801C have been subtracted from the basement penetration in that hole.

Table T2. Operation acronyms.

Acronym	Definition	Comment
APC	Advanced Piston Corer	A coring tool
APCT	Advanced Piston Corer Temperature tool	An APC coring shoe with thermistors for making temperature measurements
BCR	Bi-centered reamer	A bit used to open holes to a larger diameter than the bit diameter
BHA	Bottom-hole assembly	The bit, the thick-wall joints of pipe, and other parts that are at the bottom of the drill string
CADA	Cam-actuated Drill Ahead	A casing running tool made by Drill Quip
DDI	Downhole Designs, Incorporated	A company
DP	Dynamic positioning	A shipboard navigation system
EOP	End of pipe	The end of the pipe
FMS	Formation MicroScanner	A logging tool
gpm	Gallons per minute	A circulation rate for fluids out the end of the drill pipe
GPS	Global Positioning System	A satellite navigation system
GUATB-03C	Guatemalan Basin site selected for drilling	Now known as Site 1256
LGH	Lower guide horn	A guide located below the moonpool that keeps the pipe from getting bent sharply at the base of the ship
mbrf	Meters below rig floor	Depth measured from the rig floor
mbsf	Meters below seafloor	Depth measured from the seafloor
PDR	Precision depth recorder	An instrument for estimating water depth
PFT	Perfluorocarbon tracer	A dye used for microbiological contamination tests
RCB	Rotary core barrel	A coring tool
ROP	Rate of penetration	A coring or drilling penetration rate
spm	Strokes per minute	A circulation rate for fluids out the end of the drill pipe; 1 spm ~ 5 gpm
SSR	Subsurface release	A tool used for connecting to and releasing from casing
TDC	Tapered drill collar	A tapered heavy-walled tubular that is part of the BHA
UTC	Universal Time Coordinated	A time standard
VIT	Vibration-isolated television	The camera that is lowered along the drill string
WHC	Wireline heave compensation	Reduces motion of wireline tools by compensating for ship heave
WOB	Weight on bit	The weight at the bit
WOW	Waiting on weather	An operational delay caused by weather conditions
WOW	Waiting on whales	An operational delay in using the seismic guns because whales were in the vicinity
XCB	Extended core barrel	A coring tool

Table T3. Operations conducted during Leg 206. (See table notes. Continued on next page.)

Hole	Activity	Local time (hr)	Date (2002)	Operation on hole	Time on hole (hr)	Time on site (hr)	Time on site (days)	Comments
1256A	On location with GPS	1630	Nov 14					Spud at 0640 hr on 15 Nov
	Clear seafloor 1256A	0645	Nov 15		14.25	14.25	0.59	Objective attained
1256B	Clear seafloor 1256A	0645	Nov 15					Spud at 0815 hr on 15 Nov
	Bit at rotary table	0630	Nov 17		47.75	62.00	2.58	Basement reached
1256C	Bit at rotary table	0630	Nov 17					Spud at 1515 hr on 17 Nov
	EOP at rotary table	0345	Nov 23		141.25	203.25	8.47	Depth objective attained
1256D	EOP at rotary table	0345	Nov 23	Jet-in 20-in casing				Spud reentry cone and casing
		1035	Nov 24	End jetting	30.83	234.08	9.75	Reach 95 mbsf; release CADA
		2015	Nov 24	Bit at rotary table	9.67	243.75	10.16	Change to BCR BHA
		0620	Nov 25	Reentry 1	10.08	253.83	10.58	Enter cone with BCR BHA
		0815	Nov 25	Begin drilling	1.92	255.75	10.66	Start 21.5-in hole at 95 mbsf
		0445	Nov 27	End drilling	44.50	300.25	12.51	Stop at ~17 m into basement
		1300	Nov 27	Bit at rotary table	8.25	308.50	12.85	Failed bit bearing put junk in hole
		2140	Nov 27	Reentry 2	8.67	317.17	13.22	Reenter with 2x junk basket BHA
		0000	Nov 28	Start cleaning	2.33	319.50	13.31	Work junk baskets
		0330	Nov 28	End cleaning	3.50	323.00	13.46	Advance 1 m into basement
		0505	Nov 28	Clear seafloor	1.58	324.58	13.52	Recover drill string
		1140	Nov 28	Bit at rotary table	6.58	331.17	13.80	Change to BCR BHA
		1755	Nov 28	Reentry 3	6.25	337.42	14.06	Enter cone with BCR BHA
		2000	Nov 28	Begin drilling	2.08	339.50	14.15	Resume 21.5-in hole at ~17 m in basement
		0030	Nov 30	Begin wiper trip	28.50	368.00	15.33	TD = 276.1 mbsf (26.1 m in basement)
		0415	Nov 30	Displace hole	3.75	371.75	15.49	150 bbl sepiolite; 100 bbl barite
		0700	Nov 30	Clear seafloor	2.75	374.50	15.60	Recover drill string
		1330	Nov 30	Bit at rotary table	6.50	381.00	15.88	Rig-up for 16-in casing
		0417	Dec 1	Casing wet at 0417 hr	14.78	395.78	16.49	End making up casing
		1040	Dec 1	Detect crushed joint	6.38	402.17	16.76	Stop running casing
		0004	Dec 2	Recover casing	13.40	415.57	17.32	Replace four joints and casing collar
		1135	Dec 2	Casing wet at 1135 hr	11.52	427.08	17.80	End repair of casing string
		2008	Dec 2	Reentry 4	8.55	435.63	18.15	Weather getting bad; heave = ~2.5 m
		2315	Dec 2	Clear seafloor	3.12	438.75	18.28	POOH due to heave = ~4 m
		0650	Dec 3	Reentry 5	7.58	446.33	18.60	WOW for 5.75 hr
		1730	Dec 3	Land casing	10.67	457.00	19.04	Work stuck casing for 3.75 hr
		1745	Dec 3	Cement casing	0.25	457.25	19.05	30 bbl cement
		2115	Dec 3	Clear seafloor	3.50	460.75	19.20	Release CADA running tool
		0500	Dec 4	CADA tool on surface	7.75	468.50	19.52	Detorque CADA tool
		0630	Dec 4	Begin to run in hole	1.50	470.00	19.58	Make up bit 1: CC4 SN BX-020
		1500	Dec 4	Reentry 6	8.50	478.50	19.94	Quick reentry
		1815	Dec 4	Start to drill cement	3.25	481.75	20.07	Attempted core/dropped chisel
		0955	Dec 5	Clear seafloor	15.67	497.42	20.73	Tested bottom of hole and found junk
		1615	Dec 5	Bit at rotary table	6.33	503.75	20.99	Change to Bowen fishing magnet
		2358	Dec 5	Reentry 7	7.72	511.47	21.31	Quick reentry
		0230	Dec 6	Start fishing	2.53	514.00	21.42	Work junk baskets and magnet 1 hr
		0440	Dec 6	Clear seafloor	2.17	516.17	21.51	Quick reentry
		1130	Dec 6	Bit at rotary table	6.83	523.00	21.79	Clean magnet; Bit 2: CC-7 SN BP-723
		2130	Dec 6	Reentry 8	10.00	533.00	22.21	1-hr search for cone
		0045	Dec 7	Work junk basket	3.25	536.25	22.34	Work junk basket before coring
		0100	Dec 7	Begin coring bit 2	0.25	536.50	22.35	Clean hole!
		0900	Dec 10	End coring	80.00	616.50	25.69	Hr = 49.58; cored = 129.9 m (158.0 m in basement)
		1203	Dec 10	Work stuck pipe	3.05	619.55	25.81	Stuck when sinker bars pulled
		1435	Dec 10	Clear seafloor	2.53	622.08	25.92	
		2040	Dec 10	Bit at rotary table	6.08	628.17	26.17	Bit 3: CC-7 SN BP-737
		0410	Dec 11	Reentry 9	7.50	635.67	26.49	
		0845	Dec 11	Begin coring bit 3	4.58	640.25	26.68	
		2145	Dec 14	End coring	85.00	725.25	30.22	Hr = 62.9; cored = 88.0 m (244.0 m in basement)
		2340	Dec 14	Clear seafloor	1.92	727.17	30.30	
		0655	Dec 15	Bit at rotary table	7.25	734.42	30.60	Bit 4: CC-9 SN BF-857, no junk basket
		1435	Dec 15	Reentry 10	7.67	742.08	30.92	Quick reentry
		1800	Dec 15	Begin coring bit 4	3.42	745.50	31.06	
		2200	Dec 18	End coring	76.00	821.50	34.23	Hr = 57.8; cored = 77.0 m (321.0 m in basement)
		2355	Dec 18	Clear seafloor	1.92	823.42	34.31	
		0740	Dec 19	Bit at rotary table	7.75	831.17	34.63	
		1550	Dec 19	Reentry 11	8.17	839.33	34.97	Bit 5: CC-9 SN BF-738
		1915	Dec 19	Begin coring bit 5	3.42	842.75	35.11	3 m soft fill
		2000	Dec 22	End coring	72.75	915.50	38.15	Hr = 59.4; cored = 84.0 m (405.0 m basement)

Table T3 (continued).

Hole	Activity	Local time (hr)	Date (2002)	Operation on hole	Time on hole (hr)	Time on site (hr)	Time on site (days)	Comments
		0010	Dec 23	Clear seafloor	4.17	919.67	38.32	
		0625	Dec 23	Bit at rotary table	6.25	925.92	38.58	Bit 6: CC-9 SN BF-740
		1540	Dec 23	Reentry 12	9.25	935.17	38.97	1 hr dt piperacker
		1845	Dec 23	Begin coring Bit 6	3.08	938.25	39.09	
		1145	Dec 27	End coring	89.00	1027.25	42.80	Hr = 64.9; cored = 97.0 m (502.0 m basement)
		1515	Dec 27	Clear seafloor	3.50	1030.75	42.95	
		2300	Dec 27	Bit at rotary table	7.75	1038.50	43.27	
		0622	Dec 28	Reentry 13	7.37	1045.87	43.58	Enter cone with logging BHA
		0915	Dec 28	Rig-up for logging	2.88	1048.75	43.70	Recover VIT camera
		1000	Dec 28	Rig-up first log	0.75	1049.50	43.73	
		1930	Dec 30	End logging	57.50	1107.00	46.13	BGR magnetometer (BGRM) did not work; two runs
		2030	Dec 30	Rig-down from logging	1.00	1108.00	46.17	Triple combo, FMS, BGRM, UBI, WST
		2100	Dec 30	Clear seafloor	0.50	1108.50	46.19	
		0325	Dec 31	Bit at rotary table	6.42	1114.92	46.45	
		0330	Dec 31	Under way to Balboa	0.08	1115.00	46.46	Beacon recovered after 45 days

Notes: GPS = Global Positioning System. EOP = end of pipe. CADA = Cam-Actuated Drill-Ahead tool. BCR = bi-centered reamer. BHA = bottom-hole assembly. TD = total depth. POOH = pull out of hole. WOW = waiting on weather. VIT = vibration-isolated television. FMS = Formation MicroScanner, UBI = ultrasonic borehole imager, WST = well seismic tool.

Table T4. Coring summary, Site 1256.

Hole	Latitude	Longitude	Water depth (mbsl)	Number of cores	Interval cored (m)	Core recovered (m)	Recovery (%)	Drilled (m)	Penetration (m)
1256A	6°44.189'N	91°56.057'W	3634.5	1	2.3	2.4	103	0	2.3
1256B	6°44.190'N	91°56.060'W	3634.7	29	251.7	224.1	89.1	0	251.7
1256C	6°44.179'N	91°56.059'W	3634.7	14	120.2	61.1	50.8	220.1	340.3
1256D	6°44.163'N	91°56.061'W	3634.7	73	475.9	227.3	47.8	276.1	752.0
Totals:				117	850.1	514.9	60.6	496.2	1346.3

Table T5. Site 1256 operations summary. (See table notes. Continued on next page.)

Core	Top (mbsf)	Cored (m)	Curated (m)	Recovered (m)	Recovery (%)	Date (2002)	Local time (hr)	Comment
206-1256A-1H	0.0	2.3	2.37	2.37	103.00	Nov 15	0700	
206-1256B-1H	0.0	6.1	6.14	6.14	100.70	Nov 15	0835	
2H	6.1	9.5	9.86	9.86	103.80	Nov 15	0935	Tensor on @ 0930 hr
3H	15.6	9.5	9.88	9.88	104.00	Nov 15	1030	Tensor on @ 0930 hr
4H	25.1	9.5	10.18	10.18	107.20	Nov 15	1155	
5H	34.6	9.5	9.92	9.92	104.40	Nov 15	1235	
6H	44.1	9.5	10.01	10.01	105.40	Nov 15	1405	
7H	53.6	9.5	9.84	9.84	103.60	Nov 15	1500	
8H	63.1	9.5	9.96	9.96	104.80	Nov 15	1555	
9H	72.6	9.5	9.82	9.82	103.40	Nov 15	1700	Tensor on @ 1700 hr
10H	82.1	9.5	9.53	9.53	100.30	Nov 15	1755	
11H	91.6	9.5	9.93	9.93	104.50	Nov 15	1855	
12H	101.1	9.5	9.94	9.94	104.60	Nov 15	1950	
13H	110.6	9.5	7.44	7.44	78.30	Nov 15	2055	Imploded top and bottom
14H	120.1	9.5	9.97	9.97	104.90	Nov 15	2150	
15H	129.6	9.5	9.73	9.73	102.40	Nov 15	2250	
16H	139.1	9.5	9.73	9.73	102.40	Nov 15	2350	
17H	148.6	9.5	10.00	10.00	105.30	Nov 16	0105	Tensor out/in @ 2345 hr
18H	158.1	2.0	2.03	2.03	101.50	Nov 16	0205	
19X	160.1	5.1	4.02	4.02	78.80	Nov 16	0340	
20X	165.2	9.6	8.63	8.63	89.90	Nov 16	0445	
21X	174.8	9.2	7.71	7.71	83.80	Nov 16	0545	
22X	184.0	9.7	9.50	9.50	97.90	Nov 16	0640	
23X	193.7	9.7	9.09	9.09	93.70	Nov 16	0735	
24X	203.4	9.6	6.81	6.81	70.90	Nov 16	0830	
25X	213.0	9.7	5.80	5.80	59.80	Nov 16	0950	
26X	222.7	9.3	4.03	4.03	43.30	Nov 16	1050	
27X	232.0	9.6	0.29	0.29	3.00	Nov 16	1155	
28X	241.6	9.1	4.25	4.25	46.70	Nov 16	1335	
29X	250.7	1.0	0.13	0.10	10.00	Nov 16	1500	
206-1256C-1R	220.1	9.4	0.15	0.15	1.60	Nov 17	2230	
2R	229.5	9.5	1.85	1.85	19.50	Nov 17	2340	
3R	239.0	6.0	4.67	4.67	77.80	Nov 18	0035	
4R	245.0	7.4	0.57	0.53	7.20	Nov 18	0220	Tag basalt @ 3897.2 m (251.8 mbsf), S/B out
5R	252.4	4.7	3.89	3.27	69.60	Nov 18	0805	Note: excessive torque @ 3901.5 m (256.1 mbsf)
6R	257.1	9.3	6.80	6.21	66.80	Nov 18	1630	
7R	266.4	9.1	6.20	5.55	61.00	Nov 18	2340	Whirl-Pak, tracer
8R	275.5	9.2	7.44	7.04	76.50	Nov 19	1145	
9R	284.7	9.2	10.07	10.07	109.50	Nov 19	1750	
10R	293.9	9.4	7.08	7.03	74.80	Nov 20	0220	
11R	303.3	9.5	10.24	10.22	107.60	Nov 20	1215	Whirl-Pak/tracer other
12R	312.8	9.2	4.78	4.32	47.00	Nov 20	2125	AHC on
13R	322.0	9.1	0.16	0.16	1.80	Nov 21	0425	
14R	331.1	9.2	0.00	0.00	0.00	Nov 21	1115	TD Hole 1256C: no recovery
206-1256D-2R	276.1	2.0	1.41	1.44	72.00	Dec 7	0325	
3R	278.1	7.0	4.61	4.48	64.00	Dec 7	0845	
4R	285.1	4.8	5.31	5.29	110.20	Dec 7	1150	
5R	289.9	4.8	4.61	4.58	95.40	Dec 7	1530	
6R	294.7	9.2	9.27	9.39	102.10	Dec 7	2340	
7R	303.9	9.4	8.57	8.34	88.70	Dec 8	0315	
8R	313.3	9.5	8.40	8.15	85.80	Dec 8	0710	
9R	322.8	4.6	6.03	5.98	130.00	Dec 8	1035	
10R	327.4	4.5	4.86	4.80	106.70	Dec 8	1345	
11R	331.9	9.3	6.34	6.37	68.50	Dec 8	1759	
12R	341.2	9.1	10.28	10.38	114.10	Dec 9	0130	
13R	350.3	9.2	3.83	3.23	35.10	Dec 9	0530	
14R	359.5	4.7	3.18	2.77	58.90	Dec 9	0825	
15R	364.2	4.7	3.81	3.09	65.70	Dec 9	1345	
16R	368.9	4.6	1.25	1.01	22.00	Dec 9	1600	AHC on
17R	373.5	4.5	1.26	1.01	22.40	Dec 9	1830	
18R	378.0	4.7	2.68	2.20	46.80	Dec 9	2140	
19R	382.7	4.7	0.50	0.50	10.60	Dec 9	2359	
20R	387.4	9.4	1.28	1.23	13.10	Dec 10	0420	
21R	396.8	9.2	2.57	2.10	22.80	Dec 10	840	TD bit 2 @ 49.6 hr

Table T5 (continued).

Core	Top (mbsf)	Cored (m)	Curated (m)	Recovered (m)	Recovery (%)	Date (2002)	Local time (hr)	Comment
22R	406.0	4.3	5.48	4.88	113.50	Dec 11	1340	
23R	410.3	9.2	2.32	1.98	21.50	Dec 11	1840	
24R	419.5	9.3	3.32	2.50	26.90	Dec 12	10	
25R	428.8	9.5	0.86	0.61	6.40	Dec 12	600	
26R	438.3	7.1	8.56	7.48	105.40	Dec 12	1530	
27R	445.4	5.5	3.96	3.75	68.20	Dec 12	2105	Shot @ 2032 hr
28R	450.9	5.7	2.10	1.65	28.90	Dec 13	200	
29R	456.6	4.8	1.94	1.50	31.20	Dec 13	455	
30R	461.4	4.6	0.77	0.79	17.20	Dec 13	655	
31R	466.0	9.2	1.55	1.30	14.10	Dec 13	1330	
32R	475.2	5.8	4.83	4.38	75.50	Dec 13	2155	
33R	481.0	3.4	3.62	3.27	96.20	Dec 14	810	
34R	484.4	4.6	5.02	4.45	96.70	Dec 14	1615	
35R	489.0	5.0	2.91	2.58	51.60	Dec 14	2145	
36R	494.0	6.1	2.44	2.20	36.10	Dec 16	135	
37R	500.1	4.2	5.68	5.15	122.60	Dec 16	920	
38R	504.3	9.2	3.38	3.44	37.40	Dec 16	1925	
39R	513.5	4.0	2.93	2.85	71.20	Dec 16	2355	Nonmagnetic core barrel
40R	517.5	7.3	1.15	0.96	13.20	Dec 17	645	
41R	524.8	4.6	2.97	2.57	55.90	Dec 17	1210	Monel core barrel
42R	529.4	4.5	2.77	2.59	57.60	Dec 17	1815	
43R	533.9	9.2	2.21	1.78	19.30	Dec 17	2320	Nonmagnetic core barrel
44R	543.1	9.4	2.77	2.47	26.30	Dec 18	545	
45R	552.5	9.0	1.73	1.36	15.10	Dec 18	1330	Monel core barrel, two attempts to land core barrel
46R	561.5	9.5	3.68	3.35	35.30	Dec 18	2145	
47R	571.0	6.0	2.95	2.53	42.20	Dec 19	2359	Monel core barrel
48R	577.0	5.1	2.35	2.22	43.50	Dec 20	425	
49R	582.1	9.4	2.43	2.27	24.10	Dec 20	1130	Monel core barrel
50R	591.5	4.6	1.49	1.32	28.70	Dec 20	1435	
51R	596.1	4.6	2.91	2.47	53.70	Dec 20	1730	Monel core barrel
52R	600.7	9.1	2.20	2.18	24.00	Dec 21	110	
53R	609.8	8.3	3.70	3.70	44.60	Dec 21	1125	Monel core barrel
54R	618.1	9.3	4.30	4.05	43.50	Dec 21	2320	
55R	627.4	9.2	2.40	2.70	29.30	Dec 22	710	Nonmagnetic core barrel
56R	636.6	9.2	4.69	4.32	47.00	Dec 22	1430	
57R	645.8	9.2	5.92	5.45	59.20	Dec 22	2145	Nonmagnetic core barrel
58R	655.0	4.0	1.89	1.83	45.80	Dec 23	2245	
59R	659.0	9.6	5.29	4.72	49.20	Dec 24	605	Nonmagnetic core barrel
60R	668.6	9.4	2.04	2.03	21.60	Dec 24	1145	
61R	678.0	9.2	1.50	1.46	15.90	Dec 24	1545	Nonmagnetic core barrel
62R	687.2	9.3	1.33	1.10	11.80	Dec 24	2320	
63R	696.5	4.6	1.58	1.60	34.80	Dec 25	400	Monel core barrel
64R	701.1	4.6	2.76	2.88	62.60	Dec 25	905	
65R	705.7	4.7	3.86	3.90	83.00	Dec 25	1430	
66R	710.4	4.4	0.93	0.88	20.00	Dec 25	2025	
67R	714.8	4.7	4.22	4.13	87.90	Dec 26	240	Monel core barrel
68R	719.5	4.6	1.63	1.68	36.50	Dec 26	615	
69R	724.1	4.6	1.25	1.10	23.90	Dec 26	945	Monel core barrel
70R	728.7	4.6	2.46	2.30	50.00	Dec 26	1440	
71R	733.3	4.6	1.77	1.68	36.50	Dec 26	1900	Nonmagnetic core barrel
72R	737.9	4.5	2.45	2.39	53.10	Dec 27	10	
73R	742.4	4.8	1.90	1.83	38.10	Dec 27	505	Monel core barrel
74R	747.2	4.8	2.46	2.40	50.00	Dec 27	1155	

Notes: AHC = automatic heave compensation. TD = total depth.

Table T6. Unit summary for the sedimentary overburden, Site 1256.

Unit	Subunit	Age	Core, section, interval (cm)	Depth (mbsf)
I	IA	Pleistocene	206-1256A-1H	0-2.37
			206-1256B-1H through 3H-2, 38	0-17.48
	IB	Pliocene to late Miocene	206-1256B-3H-2, 38, through 5H-4	17.48-40.6
II		late Miocene to middle Miocene	206-1256B-5H-5 through 28X-CC	40.6-250.7
			206-1256C-1R through 3R-CC	220.1-245.0

Table T7. Calcareous nannofossil datums, ages, and depths, Site 1256.

Datum	Zone (base)	Core, section, interval (cm)		Depth (mbsf)			Age (Ma)
		Top	Bottom	Top	Bottom	Mean	
		206-1256B-	206-1256B-				
FO <i>Emiliana huxleyi</i>	NN21	1H-2, 67	1H-4, 60	2.17	5.10	3.64	0.26
LO <i>Pseudoemiliana lacunosa</i>	NN20	1H-CC	2H-2, 113	5.77	8.70	7.24	0.46
LO <i>Discoaster brouweri</i>	NN19	2H-CC	3H-4, 40-42	15.75	20.50	18.13	1.95
LO <i>Discoaster pentaradiatus</i>	NN18	3H-5, 83	3H-CC	22.43	25.22	23.83	2.52
LO <i>Discoaster surculus</i>	NN17	3H-CC	4H-2, 40-42	25.22	27.00	26.11	2.53
LO <i>Sphenolithus abies/neoabies</i>		4H-2, 40-42	4H-4, 40-42	27.00	30.00	28.50	3.66
LO <i>Reticulofenestra pseudoumbilicus</i>	NN16	4H-4, 40-42	4H-6, 40-42	30.00	33.00	31.50	3.82
FO <i>Ceratolithus rugosus</i>	NN13	5H-2, 40-42	5H-3, 40-42	36.50	38.00	37.25	5.1
LO <i>Discoaster quinqueramus</i>	NN12	5H-5, 40-42	5H-6, 93-100	41.00	43.03	42.02	5.6
FO <i>Discoaster berggrenii</i>	NN11	9H-2, 80	9H-CC	74.90	82.24	78.57	8.6
LO <i>Discoaster hamatus</i>	NN10	9H-CC	10H-4, 100	82.24	87.60	84.92	9.4
FO <i>Discoaster hamatus</i>	NN9	11H-CC	12H-4, 60	101.28	106.20	103.74	10.38
FO <i>Catinaster coalitus</i>	NN8	12H-4, 60	12H-5, 52	106.20	107.62	106.91	10.9
FO <i>Discoaster kugleri</i>	NN7	16H-CC	17H-3, 112	148.59	152.72	150.66	11.8
LO <i>Cyclicargolithus floridanus</i>		23X-3, 97	23X-CC	197.67	202.53	200.10	13.2
LO <i>Sphenolithus heteromorphus</i>	NN6	24X-CC	25X-2, 90	209.88	215.40	212.64	13.6

Notes: FO = first occurrence, LO = last occurrence. This table is also available in [ASCII](#).

Table T8. Magnetostratigraphy, Site 1256.

Depth (mbsf)	Age (Ma)	Chron/Subchron
9.30	0.780	C1n (o); Brunhes
11.47	0.990	C1r.1n (t); Jaramillo
12.61	1.070	C1r.1n (o); Jaramillo
13.87	1.201	C1r.2r-1n (t); Cobb Mountain
14.12	1.211	C1r.2r-1n (o); Cobb Mountain
17.48	1.770	C2n (t); Olduvai
18.84	1.950	C2n (o); Olduvai
20.17	2.140	C2r.1n (t); Reunion
20.60	2.150	C2r.1n (o); Reunion
23.15	2.581	C2An.1n (t); Gauss
25.36	3.040	C2An.1n (o); Gauss (above Kaena)
25.98	3.110	C2An.2n (t); Gauss
26.08	3.220	C2An.2n (o); Gauss (above Mammoth)
26.57	3.330	C2An.3n (t); Gauss
28.52	3.580	C2An.3n (o); Gauss
32.96	4.180	C3n.1n (t); Cochiti
33.85	4.290	C3n.1n (o); Cochiti
34.80	4.480	C3n.2n (t); Nunivak
35.50	4.620	C3n.2n (o); Nunivak
36.62	4.800	C3n.3n (t); Sidufjall
37.08	4.890	C3n.3n (o); Sidufjall
37.80	4.980	C3n.4n (t); Thvera
39.70	5.230	C3n.4n (o); Thvera
49.50	5.894	C3An.1n (t)
50.75	6.137	C3An.1n (o)
51.60	6.269	C3An.2n (t)
56.41	6.567	C3An.2n (o)
71.56	7.562	C4n.1n (o)
72.87	7.650	C4n.2n (t)
76.70	8.072	C4n.2n (o)
77.05	8.225	C4r.1n (t)
77.65	8.257	C4r.1n (o)
83.33	8.699	C4An (t)
84.93	9.025	C4An (o)
86.53	9.230	C4Ar.1n (t)
86.95	9.308	C4Ar.1n (o)
88.28	9.580	C4Ar.2n (t)
89.81	9.642	C4Ar.2n (o)
90.55	9.740	C5n.1n (t)
91.62	9.882	C5n.1n (o)
92.53	9.920	C5n.2n (t)

Notes: (t) = termination, (o) = onset. This table is also available in [ASCII](#).

Table T9. Igneous unit and contact log, Hole 1256C.

Unit/Subunit	Upper contact			Type	Minimum thickness (m)	Rock type
	Core, section	Piece	Depth (mbsf)			
206-1256C-						
S1	4R-1		245.525	NR	0.16	Chert
1	4R-1	5	245.235	NR	3.80	Sheet flows
S2	5R-1	1	252.415	NR	0.03	Chert
2	5R-3	5	255.93	NR	0.35	Sheet flows
3	6R-1	4	257.26	NR	0.29	Sheet flows
4	6R-1	7	257.55	C	0.28	Sheet flows
S3	6R-1	12	257.83	NR	0.17	Sediment
5	6R-1	15	347.1	NR	1.17	Sheet flows
6	6R-2	11	259.17	C	3.44	Sheet flows
7	6R-5	2	262.61	NR	1.01	Sheet flows
8	7R-1	2	266.4	NR	0.50	Sheet flows
9	7R-1	11	266.9	C	0.76	Sheet flows
10	7R-2	1	267.66	C	0.63	Sheet flows
11a	7R-2	4	268.29	C	0.28	Sheet flows
11b	7R-2	7	268.57	C	0.10	Sheet flows
11c	7R-2	11	268.67	C	1.35	Sheet flows
11 (total)					1.73	Sheet flows
12	7R-3	6	270.02	NR	0.39	Sheet flows
13	7R-4	3	270.41	C	0.20	Sheet flows
14	7R-5	1	270.61	C	1.21	Sheet flows
15	7R-5	2	271.82	NR	2.63	Sheet flows
16	8R-2	3	277.75	C	0.97	Sheet flows
17	8R-3	9	278.72	NR	1.55	Sheet flows
18a	8R-4	3	280.27	C	0.72	Flow margin
18b	8R-5	4	280.99	GS	4.03	Massive flow
18c	9R-3	1	287.17	GS	5.80	Massive flow
18d	9R-7	1	292.97	GS	1.67	Massive flow
18e	10R-1	1	293.9	GS	3.31	Massive flow
18f	10R-3	2	297.21	GS	0.08	Massive flow
18g	10R-3	4	297.29	GS	3.46	Massive flow
18h	11R-1	1	304.04	GS	7.46	Massive flow
18i	11R-6	1f	311.83	GS	2.75	Flow margin
18 (total)					29.28	Massive flow
19	12R-1	1	312.8	NR	0.48	Sheet flows
20a	12R-1	4	313.28	C	0.13	Sheet flows
20b	12R-1	5	313.41	GS	0.25	Sheet flows
20c	12R-1	7	313.66	GS	0.38	Sheet flows
20 (total)					0.76	Sheet flows
21a	12R-1	11	314.04	C	0.58	Sheet flows
21b	12R-2	2	314.62	C	1.33	Sheet flows
21 (total)					1.91	Sheet flows
22	12R-3	3	315.95	C	1.45	Flow margin

Notes: NR = not recovered, C = chilled margin, GS = gradational change in grain size. Depths calculated relative to the top of each core and based on piece lengths. This table is also available in [ASCII](#).

Table T10. Igneous unit and contact log, Hole 1256D.

Unit/Subunit	Upper contact			Type	Minimum thickness (m)	Rock type
	Core, section	Piece	Depth (mbsf)			
	206-1256D-					
1a	2R-1	1	276.10	NR	3.56	Massive flow
1b	3R-3	1	280.25	GS	10.18	Massive flow
1c	5R-3	1	292.73	GS	51.09	Massive flow
1d	12R-6	1	347.77	GS	3.57	Massive flow
1 (total)					68.40	Massive flow
2	13R-1	1	350.30	NR	6.67	Massive flow
3	15R-1	2	364.24	NR	8.53	Pillows
4a	20R-1	5	387.62	NR	0.30	Sheet flows with breccia
4b	20R-1	9	387.92	NR	1.25	Sheet flows
4c	20R-1	15	388.23	NR	1.04	Hyaloclastite
4d	21R-2	8	398.52	NR	7.96	Massive flow
4 (total)					10.55	Sheet flows
5	24R-1	7	419.74	NR	2.69	Sheet flows
6	25R-1	1	428.80	NR	2.02	Sheet flows
7	26R-2	2	439.61	NR	0.92	Sheet flows
8a	26R-3	1	440.53	NR	10.54	Massive flow
8b	28R-2	1	452.26	C	2.07	Sheet flows
8c	29R-2	5	458.02	NR	0.82	Sheet flows and hyaloclastite
8d	31R-1	1	466.00	NR	16.01	Massive flow
8 (total)					29.44	
9	35R-2	10	491.06	NR	0.79	Sheet flows
10	36R-1	6	494.24	C	7.25	Massive flow
11	37R-4	9	505.05	NR	1.35	Sheet flows
12	38R-1	19	505.24	C	1.22	Sheet flows
13	38R-2	18	506.46	NR	3.66	Sheet flows
14	40R-1	4	517.65	NR	0.79	Sheet flows
15	40R-1	16	518.44	NR	5.38	Massive flow
16a	43R-1	1	533.90	C	1.35	Sheet flows
16b	43R-2	2	535.25	C	0.68	Sheet flows
16c	44R-1	4	543.18	NR	1.03	Sheet flows
16d	44R-1	11	544.21	C	0.89	Sheet flows and hyaloclastite
16 (total)					3.95	
17	44R-2	6	545.10	NR	2.19	Sheet flows
18	46R-1	2	561.54	NR	2.90	Sheet flows
19	46R-3	9	564.44	NR	8.39	Sheet flows
20	50R-1	10	592.27	NR	1.33	Sheet flows
21	51R-1	13	596.81	NR	1.71	Hyaloclastite
22	51R-2	22	598.52	NR	1.24	Sheet flows
23	52R-1	6	601.88	C	15.82	Sheet flows
24a	57R-1	12	646.64	NR	3.33	Massive flow
24b	57R-4	2b	649.70	NR	1.41	Sheet flows
24c	57R-5	8	651.11	NR	3.71	Sheet flows
24d	59R-2	3	659.57	GS	4.31	Sheet flows
24e	60R-1	1	668.60	GS	1.94	Sheet flows
25	61R-1	1	678.50	NR	4.62	Sheet flows
26	64R-1	11	702.08	C	24.66	Sheet flows

Notes: NR = not recovered, GS = gradational change in grain size, C = chilled margin.
 Depths calculated relative to the top of each core and based on piece lengths. This table is also available in [ASCII](#).

Table T11. Locations of glass and altered glass, Holes 1256C and 1256D. (See table notes. Continued on next page.)

Core, section	Piece	Unit/ Subunit	Depth (mbsf)		Core, section	Piece	Unit/ Subunit	Depth (mbsf)	
			Glass	Altered glass				Glass	Altered glass
206-1256C-					15R-2	9	3	365.99	
5R-3	4	2	255.90		15R-2	13	3	366.27	
6R-1	7	4	257.55		15R-3	1	3	366.86	
6R-2	11	6	259.17		16R-1	5	3	369.07	
6R-5	1	6	262.61		16R-1	6	3	369.11	
7R-1	1	8	266.40		16R-1	7	3	369.15	
7R-1	11	9	266.90		16R-1	14	3	369.46	
7R-1	12	9	267.66		16R-1	22	3	369.96	
7R-2	1	10	267.66		17R-1	1	3	373.52	
7R-2	4	11a	268.29		17R-1	12	3	374.00	
7R-2	6	11a	268.53		17R-1	13	3	374.04	
7R-2	8	11b	268.64		17R-1	18	3	374.32	
7R-2	9	11c	268.67		18R-1	11	3	378.68	
7R-3	5	11c	270.00		18R-1	12	3	378.75	
7R-4	2	12	270.40		18R-2	3	3	379.45	
7R-4	3	13	270.41		18R-2	7	3	379.60	379.60
7R-5	1	14	270.61		18R-2	8	3	379.66	379.66
7R-5	1	14	271.82		18R-2	18	3	380.34	
8R-2	2	15	277.59		19R-1	8	3		383.12
8R-2	2	15		277.59	20R-1	1	3	387.44	
8R-2	3	16	277.75		20R-1	5	4a	387.65	
8R-4	4	18a	280.31		20R-1	6	4a	387.72	387.72
8R-4	6	18a	280.56	280.56	20R-1	7	4a	387.80	387.80
8R-4	7	18a	280.59	280.59	20R-1	8	4a	387.88	
8R-4	8	18a	280.71	280.71	20R-1	10	4b	387.97	
8R-5	1	18a	280.74	280.74	20R-1	11	4b		388.03
8R-5	2	18a	280.80	280.80	21R-1	6	4b	397.09	
8R-5	3	18a	280.90	280.90	21R-1	15	4c	397.50	
12R-1	4	20a		313.28	21R-1	16	4c	397.55	
12R-1	11	21a		314.04	21R-1	17	4c	397.62	
12R-2	3	21b		314.69	21R-1	18	4c	397.70	
12R-3	2	21b		315.90	21R-1	19	4c	397.77	
12R-3	4	22		316.01	21R-1	20	4c	397.85	
12R-3	6	22		316.08	21R-1	21	4c	397.94	
12R-3	7	22		316.18	21R-1	22	4c	398.01	
206-1256D-					21R-2	1	4c	398.10	
13R-1	13	2	351.11		21R-2	2	4c	398.14	
13R-2	7	2		352.08	21R-2	3	4c	398.17	
13R-2	8	2	352.14		21R-2	4	4c	398.21	
13R-2	16	2	352.79		21R-2	5	4c	398.26	
13R-2	17	2	352.84		21R-2	6	4c	398.33	
13R-3	4	2	353.23		21R-2	7	4c	398.45	
14R-1	8	2	360.21		22R-3	4	4d	408.87	
14R-1	9	2	360.25		22R-3	5	4d	408.91	
14R-1	13	2	360.54		22R-3	13	4d	409.63	
14R-1	15	2	360.61		22R-3	14	4d	409.71	
14R-1	18	2	360.71		22R-4	1	4d	409.79	
14R-1	19	2	360.89		22R-4	2	4d	409.85	
14R-1	20	2	361.06		22R-4	9	4d	410.55	
14R-1	21	2	361.09		22R-4	10	4d	410.62	
14R-1	22	2	361.13		23R-1	4	4d	410.54	
14R-2	1	2	361.16		23R-1	10	4d	411.33	
14R-2	2	2	361.19		23R-2	3	4d	411.74	
14R-2	5	2	361.41		23R-2	4	4d	411.78	
14R-2	6	2	361.46		23R-2	11	4d	412.03	
14R-2	7	2		361.54	23R-2	14	4d	412.22	
14R-2	9	2	361.72		23R-2	16	4d		412.33
14R-2	10	2	361.80		24R-1	1	4d	419.52	
14R-2	11	2	361.83		24R-1	15	5	420.28	
14R-2	13	2	361.90		24R-1	17	5	420.38	
14R-2	14	2	361.97		24R-1	19	5	420.45	
14R-2	15	2	362.04		24R-1	21	5	420.51	
14R-2	16	2	362.08		24R-2	2	5	420.95	
14R-2	17	2	362.19		24R-2	3	5	421.01	
14R-3	1	2	362.58		24R-2	8	5	421.36	
15R-1	2	3	364.29		24R-2	10	5	421.42	
15R-1	3	3	364.37		26R-1	1	6	438.36	
15R-1	4	3	364.42		26R-1	18	6	439.44	
15R-1	16	3	365.29		26R-1	19	6		439.48

Table T11 (continued).

Core, section	Piece	Unit/ Subunit	Depth (mbsf)		Core, section	Piece	Unit/ Subunit	Depth (mbsf)	
			Glass	Altered glass				Glass	Altered glass
26R-1	20	6	439.53		48R-1	11	19	578.12	
26R-2	1	6	439.59		49R-1	12	19		582.97
26R-2	2	7		439.64	49R-2	3	19	583.89	
26R-2	3	7	439.70		50R-1	17	20	592.77	
26R-2	4	7		439.78	51R-1	1	20		596.13
28R-2	4	8b	452.42		51R-1	13	21	596.82	
28R-2	5	8b	452.47		51R-1	14	21	596.86	
28R-2	6	8b	452.49		51R-1	15	21	596.93	
28R-2	7	8b	452.52		51R-1	16	21	596.98	
29R-1	1	8b	456.62		51R-1	17	21	597.03	
29R-1	3	8b		456.69	51R-1	18	21	597.08	
29R-1	7	8b	456.91	456.91	51R-1	19	21	597.16	
29R-1	19	8b	457.36		51R-1	20	21	597.22	
29R-2	3	8b	457.95		51R-1	21	21	597.26	
29R-2	5	8c		458.05	51R-1	22	21	597.33	
30R-1	1	8c	461.43		51R-2	1	21	597.40	
30R-1	2	8c	461.49		51R-2	2	21	597.44	
30R-1	3	8c	461.56		51R-2	3	21	597.46	
30R-1	4	8c	461.61		51R-2	4	21	597.49	
30R-1	5	8c	461.67		51R-2	5	21	597.55	
30R-1	6	8c	461.74		51R-2	6	21	597.62	
30R-1	7	8c	461.85		51R-2	7	21	597.69	
30R-1	8	8c	461.94		51R-2	8	21	597.76	
30R-1	9	8c	461.98		51R-2	9	21	597.84	
30R-1	10	8c	462.01		51R-2	10	21	597.93	
30R-1	11	8c	462.05		51R-2	11	21	598.01	
31R-1	8	8d	466.28		51R-2	12	21	598.08	
31R-1	11	8d	466.46		51R-2	13	21	598.15	
35R-2	7	8d	490.96		51R-2	14	21	598.21	
35R-2	8	8d	491.01		51R-2	15	21	598.25	
35R-2	9	8d	491.04	491.04	51R-2	16	21	598.28	
35R-2	12	9	491.24		51R-2	17	21	598.31	
36R-1	3	9	494.11		51R-2	18	21	598.36	
38R-1	21	12	505.34		51R-2	19	21	598.41	
38R-1	22	12	505.41		51R-2	20	21	598.46	
38R-1	23	12	505.48		51R-2	21	21	598.51	
38R-2	3	12	505.78		52R-1	6	23	601.91	
38R-2	11	12		506.16	52R-1	9	23	602.04	
40R-1	5	14	517.73		52R-1	10	23	602.08	
40R-1	6	14	517.79		52R-1	11	23	602.11	
43R-1	2	16a	533.98		53R-1	12	23	610.56	
43R-1	3	16a	534.03		53R-2	8	23	611.80	
43R-1	4	16a	534.07		54R-1	4	23	618.96	
43R-1	5	16a	534.09		54R-2	7	23	620.09	
43R-1	6	16a	534.13		54R-3	14	23		622.08
43R-1	7	16a	534.18		54R-3	15	23		622.12
43R-1	8	16a	534.22		56R-1	18	23		637.87
43R-1	20	16a	535.06		56R-2	1	23	637.91	
43R-2	2	16b	535.27		63R-1	20	25	697.39	
43R-2	4	16b	535.36		64R-1	1	25	701.11	
43R-2	8	16b	535.63		64R-1	11	26	702.10	
44R-1	1	16b	543.12		64R-2	10	26	703.29	
44R-1	2	16b	543.16		65R-1	3	26	705.79	
44R-1	11	16d	544.24		67R-1	3	26	715.30	
44R-1	13	16d	544.33		67R-1	10	26	715.74	
44R-1	14	16d	544.38		67R-1	12	26	715.82	
44R-1	15	16d	544.42		67R-2	6	26	716.68	
44R-1	16	16d	544.47		68R-1	4	26		719.80
45R-1	3	17		552.64	68R-1	9	26	720.13	
45R-1	11	17	553.00		68R-1	10	26	720.21	
45R-1	19	17	553.49		70R-1	7	26	729.19	
46R-1	4	18	561.75		70R-1	8	26	729.27	
46R-1	5	18	561.79		71R-1	1	26	733.32	
46R-1	6	18	561.83		71R-1	10	26		733.95
46R-1	7	18	561.88		73R-1	11	26		743.20
46R-3	9	19		564.48	73R-1	12	26		743.26
47R-1	3	19	571.50						
47R-1	12	19	572.07						
47R-2	3	19	572.57						
48R-1	5	19	577.48						
48R-1	6	19	577.54						

Notes: Depths are calculated relative to the top of each core and based on piece length. This table is also available in [ASCII](#).